

SSC-444

**IN-SERVICE NON-DESTRUCTIVE
ESTIMATION OF THE REMAINING
FATIGUE LIFE OF WELDED JOINTS**



This document has been approved
For public release and sale; its
Distribution is unlimited

SHIP STRUCTURE COMMITTEE
2005

Ship Structure Committee

RADM Thomas H. Gilmour
U. S. Coast Guard Assistant Commandant,
Marine Safety and Environmental Protection
Chairman, Ship Structure Committee

Mr. W. Thomas Packard
Director,
Survivability and Structural Integrity Group
Naval Sea Systems Command

Senior Vice President
American Bureau of Shipping

Mr. Joseph Byrne
Director, Office of Ship Construction
Maritime Administration

Mr. Gerard A. McDonald
Director General, Marine Safety,
Safety & Security
Transport Canada

Mr. Kevin Baetsen
Director of Engineering
Military Sealift Command

Dr. Neil Pegg
Group Leader - Structural Mechanics
Defence Research & Development Canada - Atlantic

Mr. Jaideep Sirkar
(SNAME T&R Chair)
Society of Naval Architects & Marine Engineers

CONTRACTING OFFICER TECHNICAL REP.

Mr. Chao Lin / MARAD
TBD / NAVSEA
Mr. Robert Sedat / USCG

EXECUTIVE DIRECTOR

Lieutenant William A. Nabach
U. S. Coast Guard

SHIP STRUCTURE SUB-COMMITTEE

AMERICAN BUREAU OF SHIPPING

Mr. Glenn Ashe
Mr. Yung Shin
Mr. Phil Rynn
Mr. William Hanzalek

DEFENCE RESEARCH & DEVELOPMENT ATLANTIC

Dr David Stredulinsky
Mr. John Porter

MARITIME ADMINISTRATION

Mr. Chao Lin
Mr. Carlos Setterstrom
Mr. Richard Sonnenschein

MILITARY SEALIFT COMMAND

Mr. Joseph Bohr
Mr. Paul Handler
Mr. Michael W. Touma

NAVAL SEA SYSTEMS COMMAND

Mr. Jeffery E. Beach
Mr. Allen H. Engle
Mr. Charles L. Null

TRANSPORT CANADA

Mr. Val Smith

UNITED STATES COAST GUARD

Mr. Rubin Sheinberg
Mr. Robert Sedat
Mr. H. Paul Cojeen
Captain Ray Petow

Member Agencies:

*American Bureau of Shipping
Defence Research Development Canada
Maritime Administration
Military Sealift Command
Naval Sea Systems Command
Society of Naval Architects & Marine Engineers
Transport Canada
United States Coast Guard*



**Ship
Structure
Committee**

Address Correspondence to:

Executive Director
Ship Structure Committee
U.S. Coast Guard (G-MSE/SSC)
2100 Second Street, SW
Washington, D.C. 20593-0001
Web site: <http://www.shipstructure.org>

**SSC – 444
SR – 1433**

OCTOBER 2005

**IN-SERVICE NON-DESTRUCTIVE ESTIMATION OF THE REMAINING FATIGUE LIFE OF
WELDED JOINTS**

Ship structures are subjected to fatigue loading during daily operations. Under cyclic loading, fatigue cracks can form at defects or discontinuities in a structure, especially in welded joints due to the inherent defects in the weld. Historically, ships were not designed for fatigue loading. Fatigue cracking can be a significant problem for ships, especially at welded joints. If a method for determining the extent of fatigue damage and an estimation of remaining fatigue life could be found, both time and resources could be saved in the maintenance of ship structures.

Research was performed to determine the feasibility of using ultrasonic non-destructive testing methods to predict the fatigue life of a welded detail. If the fatigue life of a detail could be reliably determined, the repair of fatigue cracking could be performed in a more efficient manner.

The correlation between the crack depths found using ultrasonic testing to the remaining fatigue life of the welded joints was studied. Also investigated was the relationship between crack lengths found by visual observation and the remaining fatigue life of the welded joints. The limited results found through this project do not support any substantial conclusions regarding the use of ultrasonic testing methods for the prediction of remaining fatigue life.

A handwritten signature in black ink, appearing to read 'T. H. Gilmore', written in a cursive style.

T. H. GILMOUR

Rear Admiral, U.S. Coast Guard
Chairman, Ship Structure Committee

Technical Report Documentation Page

1. Report No. SSC-444		2. Government Accession No. PB2005-		3. Recipient's Catalog No.	
4. Title and Subtitle In-Service Non-Destructive Estimation of the Remaining Fatigue Life of Welded Joints				5. Report Date October 2005	
				6. Performing Organization Code	
7. Author(s) Shield, C.K., Swanson K.M., Dexter R.J.				8. Performing Organization Report No. SR-1433	
9. Performing Organization Name and Address University of Minnesota./ Dept. of Civil Engineering 122 CivE, 500 Pillsbury Dr. S.E. Minneapolis, MN 55455-0116				10. Work Unit No. (TRAIS)	
				11. Contract or Grant No. DTCG32-03-F-100045	
12. Sponsoring Agency Name and Address Ship Structure Committee U.S. Coast Guard (G-MSE/SSC) 2100 Second Street, SW Washington, DC 20593				13. Type of Report and Period Covered Final Report	
				14. Sponsoring Agency Code G-M	
15. Supplementary Notes Sponsored by the Ship Structure Committee. Jointly funded by its member agencies.					
16. Abstract Testing was performed to determine the feasibility of using non-destructive testing to predict the fatigue life of welded joints. Tests were conducted on large-scale specimens which realistically modeled details found in ship hulls. Ultrasonic non-destructive testing, both the time of flight diffraction method and the linear phased array method, was performed to detect fatigue cracking in the specimens. The correlation between the crack depths found using ultrasonic testing to the remaining fatigue life of the welded joints was studied. Also investigated was the relationship between crack lengths found by visual observation and the remaining fatigue life of the welded joints. The limited results found through this project do not support any substantial conclusions regarding the use of ultrasonic testing methods used for the prediction of remaining fatigue life.					
17. Key Words Ultrasonic Testing, Phased Array, Fatigue, Fatigue Life, Weld, Non-Destructive Evaluation, time of flight diffraction			18. Distribution Statement Distribution is available to the public through: National Technical Information Service U.S. Department of Commerce Springfield, VA 22151 Ph. (703) 487-4650		
19. Security Classif. (of this report) Unclassified		20. Security Classif. (of this page) Unclassified		21. No. of Pages	22. Price

CONVERSION FACTORS
(Approximate conversion of common U.S. Customary units
used for ship structures to metric or SI units)

To convert from	To	Function	Value
LENGTH			
Inches	Meters	divide by	39.3701
Inches	Millimeters	multiply by	25.4000
Feet	Meters	divide by	3.2808
VOLUME			
cubic feet	cubic meters	divide by	35.3149
cubic inches	cubic meters	divide by	61,024
SECTION MODULUS			
inches ² feet	centimeters ² meters	multiply by	1.9665
inches ² feet	centimeters ³	multiply by	196.6448
inches ³	centimeters ³	multiply by	16.3871
MOMENT OF INERTIA			
inches ² feet ²	centimeters ² meters ²	divide by	1.6684
inches ² feet ²	centimeters ⁴	multiply by	5993.73
inches ⁴	centimeters ⁴	multiply by	41.623
FORCE OR MASS			
Long tons	Tonnes	multiply by	1.0160
Long tons	Kilograms	multiply by	1016.047
Pounds	Tonnes	divide by	2204.62
Pounds	Kilograms	divide by	2.2046
Pounds	Newtons	multiply by	4.4482
PRESSURE OR STRESS			
Pounds/inch ²	Newtons/meter ² (Pascals)	multiply by	6894.757
Kilo pounds/inch ²	mega Newtons/meter ² (mega Pascals)	multiply by	6.8947
Pounds/inch ²	kg/cm ²	divide by	14.2232
kg/cm ²	mega Pascals	multiply by	0.098065
BENDING OR TORQUE			
Foot tons	meter tons	divide by	3.2291
Foot pounds	Kilogram meters	divide by	7.23285
Foot pounds	Newton meters	multiply by	1.35582
ENERGY			
Foot pounds	Joules	multiply by	1.355826
STRESS INTENSITY			
Kilo pounds/inch ² inch ^{1/2} (ksi√in)	mega Newton MNm ^{3/2}	multiply by	1.0998
J-INTEGRAL			
Kilo pound/inch	Joules/mm ²	multiply by	0.1753
Kilo pound/inch	Kilo Joules/m ²	multiply by	175.3
TEMPERATURE			
Degrees Fahrenheit	Degrees Celsius	subtract & divide by	32 1.8

ACKNOWLEDGMENT

The study was performed in the Structures Laboratory of the Department of Civil Engineering at the University of Minnesota. The project was administered by the Ship Structure Committee through a contract to John J. McMullen Associates, Inc. (JJMA). The authors are grateful for the support and guidance of Raymond Kramer and Peter Fontneau of JJMA. A special thanks to Jay Richardson of Structural Integrity Associates, Inc, who performed the ultrasonic testing. The authors wish to especially thank Paul Bergson, the manager of the Structures Laboratory, for his assistance and patience in the completion of the difficult experimental work. The authors are also indebted to the undergraduate laboratory assistants for their aid in the completion of the laboratory experiments. Lastly, the first and second authors would like to acknowledge the contributions of the third author to this project and to the field of fatigue of steel structures made prior to his untimely death on November 16, 2004. The entire steel community will feel the loss of Robert Dexter.

TABLE OF CONTENTS

1	INTRODUCTION.....	1
1.1	Problem Statement.....	1
1.2	Research Objective.....	1
1.3	Organization of Report.....	2
2	BACKGROUND.....	3
2.1	Estimation of Remaining Fatigue Life Based on Non-Destructive Testing Measurements.....	3
2.2	Ultrasonic Testing.....	5
2.2.1	Acoustic Wave Propagation.....	5
2.2.2	Wave Phenomena: Reflection, Refraction and Diffraction.....	7
2.2.2.1	Snell’s Law for Reflection and Refraction.....	8
2.2.2.2	Acoustic Impedance.....	9
2.2.2.3	Diffraction.....	10
2.2.2.4	Wave Phenomena Detected in Ultrasonic Testing Methods.....	10
2.2.3	Acoustic Wave Attenuation.....	11
2.2.4	Near Field Versus Far Field.....	12
2.2.5	Ultrasonic Testing Equipment.....	13
2.2.5.1	Piezoelectric Materials.....	13
2.2.5.2	Frequency of Testing.....	14
2.2.5.3	Additional Testing Equipment.....	14
2.2.6	Pulse Echo Method.....	15
2.2.7	Phased Array Method.....	16
2.2.7.1	Linear Phased Array Transducer Design.....	21
2.2.7.2	Linear Phased Array Output.....	22
2.2.7.3	Phased Array Detection Trials.....	22
2.2.8	Time of Flight Diffraction Method.....	25
2.2.8.1	Time of Flight Diffraction Output.....	28
2.2.8.2	Detection of Fatigue Cracks Using the Time of Flight Diffraction Method.....	34
2.2.8.3	Time of Flight Diffraction Testing Trials.....	36

2.2.8.4	Time of Flight Diffraction Operator Error.....	40
2.3	Eddy Current Testing.....	42
2.3.1	Eddy Currents.....	42
2.3.2	Mutual Inductance.....	42
2.3.3	Eddy Current Behavior (Defect Detection).....	44
2.3.4	Current Density and Depth of Eddy Current Penetration.....	45
2.3.5	Eddy Current Equipment.....	47
2.3.5.1	Probe/Coil.....	47
2.3.5.2	Frequency.....	48
2.3.5.3	Impedance Measurements/ Bridge Circuit.....	49
2.3.6	Lift-off and Probe Wobble.....	49
2.3.7	Output.....	49
2.3.8	Simple Calibration of Instruments.....	50
2.3.9	Testing of Ferromagnetic Materials.....	50
2.3.10	Advantages/Limitations.....	51
3	EXPERIMENTAL PROCEDURE.....	53
3.1	Test Specimens.....	53
3.2	Test Set Up.....	56
3.3	Static Calibration.....	56
3.4	Fatigue Test Procedure.....	62
3.5	Weld Repair Procedure.....	63
3.6	Non-Destructive Testing Procedure.....	66
3.6.1	Linear Phased Array Procedure.....	67
3.6.2	Time of Flight Diffraction Procedure.....	69
3.6.3	Dye Penetrant Testing.....	72
3.7	Fatigue Testing History.....	72
3.7.1	Specimen A.....	72
3.7.2	Specimen B.....	73
3.7.3	Specimen C.....	77
4	TESTING RESULTS.....	79
4.1	Fatigue Testing Results.....	79

4.2	Non-Destructive Testing Results	83
4.3	Correlation of TOFD Results to Remaining Fatigue Life	86
4.4	Correlation of Visual Observations to Remaining Fatigue Life	87
4.5	Correlation Between TOFD Measurements and Visual Observations	89
4.6	Feasibility of Using Time of Flight Diffraction and Linear Phased Array Testing to Predict Remaining Fatigue Life	90
5	CONCLUSIONS	91
6	RECOMMENDATIONS	93
7	REFERENCES	95

APPENDIX: NON-DESTRUCTIVE TESTING DATA

LIST OF TABLES

Table 3.1: Comparison of predicted versus measured stress in Specimen B at points of maximum loading, with maximum moment of 53.0 kN-m	59
Table 3.2: Comparison of predicted versus measured stress in Specimen C at points of maximum loading, with maximum moment of 26.5 kN-m	60
Table 3.3: Number of cycles undergone by each specimen at each round of NDT	66
Table 3.4: Fatigue history of Specimen A	73
Table 3.5: Fatigue history of Specimen B	74
Table 3.6: Fatigue history of Specimen C	78
Table 4.1 NDT results for Specimen A	80
Table 4.2 NDT results for Specimen B.....	81
Table 4.3 NDT results for Specimen C.....	82
Table A.1 NDT results for Specimen A.....	A-2
Table A.2 NDT results for Specimen B.....	A-3
Table A.3 NDT results for Specimen C.....	A-4

LIST OF FIGURES

Figure 2.1: Particle movements during shear and compression wave propagation in an elastic medium	6
Figure 2.2: Reflection and refraction of a sound wave at material interface	8
Figure 2.3: Wave phenomena resulting from incident wave encountering crack.....	11
Figure 2.4: Pulse echo probe with (a) favorable orientation relative to defect (b) unfavorable orientation to defect	16
Figure 2.5: Linear phased array probe with 16 elements.....	17
Figure 2.6: Constructive interference of sound waves forming focused beam in linear phased array testing.....	18
Figure 2.7: Delay laws for linear phased array testing	20
Figure 2.8: Linear phased array S-scan.....	23
Figure 2.9: Ultrasonic waves detected during TOFD testing	27
Figure 2.10: A-scan representation of TOFD	29
Figure 2.11: Indication with given time delay lies on ellipse with location of transducers as foci	30
Figure 2.12: Minimum time delay for cracks reached for transducer pair T-2 and R-2, as defect is centered between probes.....	30
Figure 2.13: TOFD scan directions.....	31
Figure 2.14: Typical TOFD B-scan with defect indications.....	33
Figure 2.15: TOFD B-scan with indication at upper cursor	34
Figure 2.16: Mutual inductance in circuit.....	43
Figure 2.17: Mutual inductance for eddy current testing.....	44
Figure 2.18: Pattern of eddy currents flowing in test material	46
Figure 3.1: Typical specimen.....	54
Figure 3.2: Photograph of typical specimen	55
Figure 3.3: Numbering of tee attachments.....	55
Figure 3.4: Load frame	57
Figure 3.5: Load frame with specimen in place.....	58
Figure 3.6: Clamped roller connection	58
Figure 3.7: Strain gauge layout.....	59

Figure 3.8: Stress distribution through beam cross section for Specimen B, at maximum moment of 53 kN-m.....	60
Figure 3.9: Stress distribution through beam cross-section for Specimen C, at maximum moment of 26.5 kN-m.....	61
Figure 3.10: Stress along length of beam for Specimen B, at maximum moment of 53 kN-m.....	61
Figure 3.11: Stress along length of beam for Specimen C, at maximum moment of 26.5 kN-m.....	62
Figure 3.12: Typical crack at failure of attachment.....	64
Figure 3.13: Typical repair weld.....	65
Figure 3.14: Area covered by each LPA scan.....	67
Figure 3.15: Linear phased array testing equipment.....	68
Figure 3.16: TOFD testing equipment.....	70
Figure 3.17: Probe placement for the TOFD scanning of flange and stem of tee attachment.....	71
Figure 3.18: Area covered by each UT scan.....	71
Figure 3.19: Crack in flange of Specimen B at flange of Tee 3.....	75
Figure 3.20: Weld repair of large crack in Specimen B at flange of Tee 3.....	76
Figure 4.1: Number of cycles vs. surface length for attachments on Specimen C.....	83
Figure 4.2: Depth of crack found using TOFD vs. LPA.....	85
Figure 4.3: Cycles to failure vs. TOFD estimated crack depth for non hammer-peened attachment details.....	87
Figure 4.4: Cycles to failure vs. TOFD estimated crack depth for hammer-peened attachment details.....	88
Figure 4.5: Cycles to failure vs. surface crack length.....	88
Figure 4.6: Surface crack length vs. crack depth determined using TOFD.....	89

EXECUTIVE SUMMARY

Global and local ship structures are subjected to cyclic loading during normal operation with increased cycles resulting from wave impact and machinery oscillations. Thus, fatigue cracking can be a significant problem for ships, especially at welded joints. The repair of these cracks can be expensive and time consuming. Both time and resources could be saved in the maintenance of ship structures if a method for determining the extent of fatigue damage and an estimation of remaining fatigue life could be found. Then, it would be possible to more effectively manage the repair of fatigue cracking. Research was performed to determine the feasibility of using ultrasonic non-destructive testing methods to predict the fatigue life of a welded detail. If the fatigue life of a detail could be reliably determined, the repair of fatigue cracking could be performed in a more efficient manner.

Fatigue testing was performed on three specimens. Each specimen was a W10 x 30 grade 50 beam, approximately 3.5 meters long with eight WT6 x 9.5 tee attachments fillet welded to the beam flanges. The specimens were subjected to cyclic loading to grow fatigue cracks at the welded details. Ultrasonic non-destructive testing, both time of flight diffraction and linear phased array, was performed at three times during fatigue testing to determine the extent of fatigue cracking. The specimens were monitored closely during testing for signs of surface cracking. Once cracking was detected, the surface crack length versus the number of cycles was recorded at regular intervals.

The relationship between the crack depths determined using ultrasonic testing versus the cycles to failure was investigated. Analysis of the limited amount of data collected indicated that there was little correlation between these two quantities. There was a reasonable correlation between the surface crack length and the remaining cycles to failure. There was no correlation between the surface crack length and the crack depth found using ultrasonic testing as would be expected. This indicates that the depth measurements taken by time of flight diffraction and linear phased array ultrasonic testing methods are not suitable for the extrapolation of fatigue life in welded steel joints.

1 INTRODUCTION

1.1 Problem Statement

Ship structures are subjected to fatigue loading during daily operations. This fatigue loading is due to the full spectrum of hull girder wave loading in all sea states, vibration from wave impacts and the oscillatory effects of rotating machinery. Under this cyclic loading, fatigue cracks can form at defects or discontinuities in a structure, especially in welded joints due to the inherent defects in the weld. Historically, ships were not designed explicitly for fatigue loading; instead a peak allowable stress was defined. By limiting the peak stress, designers hoped to avoid problems with fatigue [1]. Because of this approach, many large ship structures experience extensive fatigue damage [2,3]. Due to the highly redundant nature of ship structures, these fatigue cracks will typically not compromise structural integrity [1,4]. However, when left unchecked, fatigue cracks can grow to catastrophic proportions resulting in both local and global structural failure.

In general, the detection and repair of occasional fatigue cracks has become a part of routine maintenance. It is costly, and impractical, to take a ship out of service for repair every time a fatigue crack appears. It may be more efficient to create a method to predict fatigue crack growth and determine the threat that each crack may pose. Cracks that are found not to be propagating, and thus posing no risk to the structural integrity of the ship, may not need to be repaired immediately. The repair of fatigue cracks may then be planned for and managed more effectively with many cracks being repaired at one time. This approach has the potential to be more cost effective, saving time and resources and allowing for continued operation of the ship with a better understanding of the risk associated with specific cracks located in various areas of the ship.

1.2 Research Objective

This project was conducted to determine the feasibility of using non-destructive testing measurements to predict the remaining fatigue life of a welded joint, to better determine when repair of a fatigue crack is needed. Previous studies have been conducted to investigate the correlation between non-destructive testing measurements to remaining

life for various applications including those applicable to the aircraft and automobile industries [5,6,7]. However, no known studies have been conducted on typical welded joints found in ship structures, which have inherent defects that may or may not evolve into fatigue cracks.

For this project, fatigue tests were conducted on large-scale specimens which realistically modeled details found in ship hulls. Ultrasonic testing methods were used, both time of flight diffraction and linear phased array, to characterize any fatigue cracking in the specimens. The feasibility of using these non-destructive testing methods to predict the remaining fatigue life of the welded joints was investigated.

1.3 Organization of Report

Chapter 2 describes background information for the current project. This background includes a description of ultrasonic testing methods, specifically the time of flight diffraction and linear phased array methods. The physics of these methods is discussed, including wave propagation in elastic media. A summary of work done by previous researchers on the capabilities of these two ultrasonic testing methods in the detection and characterization of defects, and the use of non-destructive testing methods for the prediction of remaining fatigue life is included. Eddy current testing, an electromagnetic testing method, is also described. Chapter 3 describes the experiments conducted for this project including fatigue testing and non-destructive testing procedures. The results of the fatigue testing and non-destructive testing are found in Chapter 4. Also contained in Chapter 4 is an analysis of the data including the correlation of non-destructive testing data to the remaining life of the test specimens. Chapters 5 and 6 contain the project Conclusions and Recommendations, respectively.

2 BACKGROUND

Background information is provided on the research done in an attempt to correlate fatigue life in steel and aluminum directly to various non-destructive testing (NDT) methods. Then, the propagation of ultrasonic waves in elastic media, the basis for ultrasonic testing (UT) is described. Ultrasonic testing methods are discussed, specifically the time of flight diffraction (TOFD) method and the linear phased array (LPA) method. Included in the discussion is the way these two ultrasonic testing methods detect defects along with their capabilities in the detection and characterization of defects. Also discussed is eddy current testing, an electromagnetic non-destructive testing method.

2.1 Estimation of Remaining Fatigue Life Based on Non-Destructive Testing Measurements

The fatigue life of a steel member is considered to be the number of cycles needed to reach a crack dimension, either length or depth, of a certain magnitude. The magnitude of the crack dimension at failure is highly dependent on the member size, type and the use of the structure. For this project, fatigue life was considered to be the number of cycles undergone before the formation of a through thickness crack 50 mm in length. The fatigue life of a member can be transformed into operational time based on the frequency of loading.

To the authors' knowledge, little research has been done in attempt to correlate remaining fatigue life of steel members directly to the output from a non-destructive testing method.

Shell [5] investigated the use of three NDT methods, pulse echo ultrasonic testing, white light interference microscopy (WLIM), and microradiography to predict the fatigue life of corroded aluminum specimens. The 48 specimens were made from 2 mm thick aluminum plate and were exposed to various conditions to create a range of corrosion damage. NDT testing was performed prior to fatigue cycling. From the NDT testing, 19 quantities (metrics) were investigated, including roughness, corrosion depth, material volume loss and signal loss. Then, the specimens were cycled to failure. Up to 15 of the 19 metrics studied were found to reasonably predict fatigue life of the specimens. Those

metrics with the strongest correlations to fatigue life include peak roughness found using WLIM, maximum UT signal lost, and the loss of cross-sectional area. The depth of corrosion estimated by UT, however, had little correlation with fatigue life, even though as Shell notes “this is a typical measurement used in structural analyses of corroded components.” An empirical model was then created. For most metrics, it was found that there was a linear relationship between the logarithm of the metric and the fatigue life of the corroded specimens.

Asif and Modh [6] used the electric potential method, an electromagnetic form of non-destructive testing, to correlate fatigue crack area to number of strain cycles in low cycle fatigue. Specimens were made from notched steel cylinders subjected to four-point bending and a rotation to encourage fatigue crack growth. Measurements were taken at various times during testing for five strain levels. It was found that the potential drop across the specimen increased as the area of crack increased, somewhat independent of strain level. Results for the number of strain cycles at a given crack area were plotted for the five strain levels. It was found that the relationship between strain cycles and crack area was nearly linear for each strain level. Thus, by determining the percentage change in the voltage across a specimen, the remaining fatigue life was predicted.

Kim [7] attempted to estimate the remaining fatigue life of an automobile chassis fabricated from thin cold-rolled steel plate. A magnetic non-destructive testing method was used which gives the relationship between magnetic flux and stress in the specimen. It was found that the magnetic flux decreased exponentially as the number of fatigue cycles increased. A statistical model was created to predict the remaining fatigue life of the specimen based on the magnetic flux found during NDT, normalized by a baseline magnetic flux taken before fatigue testing began.

The current project hoped to further these research attempts and gain results applicable to the ship industry for the estimation of fatigue life based on measurements taken with ultrasonic testing methods.

2.2 Ultrasonic Testing

Ultrasonic testing for the detection of defects in metals was first done in 1929 by S. Y. Sokolov in Russia [8]. Since its conception, ultrasonic testing has become a widely used form of non-destructive testing with many advancements and variations. Ultrasonic testing can be used to detect cracks, voids, and changes in geometric and material parameters such as thickness, stress and modulus [9]. All ultrasonic testing methods are similar in that they use ultrasonic waves for the detection of defects or material properties. No matter what method is used to introduce ultrasound into a test specimen, the sound energy in the specimen will be of the same form. The testing methods differ in which detectable signals are of interest and used for the detection and characterization of defects. For this project, the ultrasonic TOFD method and the ultrasonic LPA method were used for defect detection.

2.2.1 Acoustic Wave Propagation

Ultrasonic testing methods use ultrasonic sound waves, those waves having a higher frequency than is audible to the human ear, to detect defects. Sound waves are stress waves which propagate as oscillations of discrete particles of matter. These sound waves can be generated in a material by applying small, high frequency displacements to the surface [9]. In order for ultrasonic testing to be truly non-destructive, the sound waves used must be of low amplitude, which will adhere to the principles of linear elastic theory. These low amplitude waves will subject the test specimen to stresses well below the yield stress of the material and will not alter the specimen [10].

Several types of sound waves will propagate in a solid material, two of these are shown in Figure 2.1. Compression waves cause particles to oscillate in the same direction as the wave is propagating and have the highest velocity of all sound waves, thus they are often called primary waves. Shear waves cause particle motion in the direction transverse to the direction of wave propagation. The velocity of shear waves in isotropic media is approximately half the velocity of compression waves. There also exist various surface waves, including Rayleigh waves and Lamb waves. Surface waves produce more complex particle motions than either compression or shear waves. The velocity of

surface waves is approximately 90% that of shear waves, and thus the surface waves are often ignored in ultrasonic testing [9].

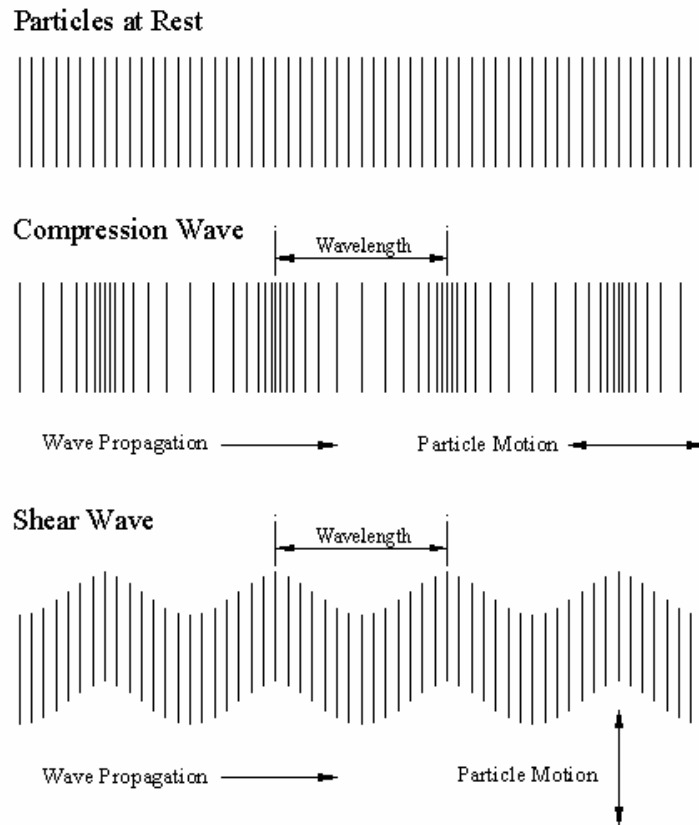


Figure 2.1: Particle movements during shear and compression wave propagation in an elastic medium

The velocity of sound waves is distinct in each material and can be found using Equations (2-1) for compression waves and (2-2) for shear waves.

$$V_c = \sqrt{\frac{E}{\rho} \cdot \frac{1-\nu}{(1+\nu)(1-2\nu)}} \quad (2-1)$$

$$V_s = \sqrt{\frac{E}{\rho} \cdot \frac{1}{2(1+\nu)}} \quad (2-2)$$

where V_c is the compression wave velocity, V_s is the shear wave velocity, E is the Young's modulus of elasticity, ρ is the material density, and ν is the Poisson ratio. The

velocity of sound waves in steel is roughly 5.90 km/s for compression waves and 3.23 km/s for shear waves [11].

The wavelength, λ , of a sound wave is equal to:

$$\lambda = \frac{V}{f} \quad (2-3)$$

where V is the acoustic velocity and f is the frequency of the wave. As the wavelength is directly proportional to the velocity of the sound wave, waves with a higher velocity will have a larger wavelength. Thus, the wavelength of compression waves is approximately twice as large as the wavelength of shear waves due to their higher velocity at a given frequency.

Different types of sound waves propagate with wave fronts of different shapes. A wave front is the boundary separating the volume of material that has been disturbed by the elastic wave from the undisturbed medium, and comes in two shapes, either spherical or cylindrical [12]. Compression and shear waves tend to travel with spherical wave fronts. Thus, compression and shear waves propagate out from their point source in all directions, unless an obstacle is encountered. Surface waves travel with a cylindrical wave front.

2.2.2 Wave Phenomena: Reflection, Refraction and Diffraction

When an ultrasonic wave encounters a boundary between two infinite media with different physical properties, the wave cannot continue to propagate in its original form. Two phenomena of waves may be observed at such a boundary, reflection and refraction of the wave. Reflection is the bouncing of ultrasonic energy off of a boundary and back into the original medium. Refraction is the bending of the path of the ultrasonic beam as it is transmitted through the boundary between the two materials. Reflection and refraction are illustrated in Figure 2.2. This change in the path of the sound energy is caused by the change in ultrasonic velocity as the beam passes into the second medium. Diffraction is the scattering of sound waves when incident energy encounters an obstacle of finite length in its intended path, such as a crack or discontinuity.

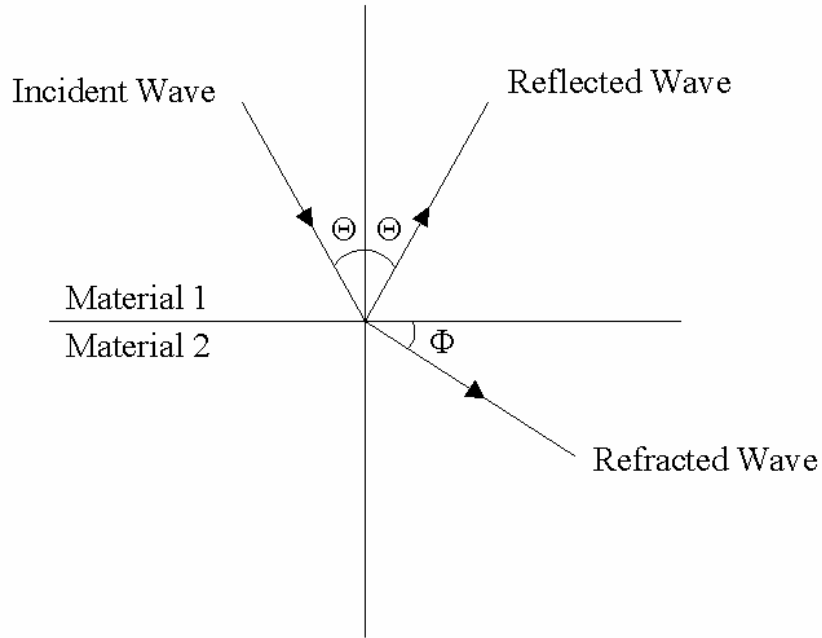


Figure 2.2: Reflection and refraction of a sound wave at material interface

2.2.2.1 Snell's Law for Reflection and Refraction

Snell's Law for the reflection and refraction of sound waves describes the behavior of a sound wave when it reaches a boundary between two materials with different properties. Snell's Law is given by:

$$\frac{\sin \theta}{V_{L1}} = \frac{\sin \Phi}{V_{L2}} \quad (2-4)$$

where θ is the angle of incidence, Φ is the angle of refraction, V_{L1} is the compression wave velocity in material 1, and V_{L2} is the compression wave velocity in material 2.

This equation relates the angle of incidence of the sound wave in the original material to the angle of refraction in the second material based on the corresponding velocities of sound for the two media. This law also states that the angle of incidence will be equal to the angle of reflection.

If the incident angle is not perpendicular to the material boundary, mode conversion of the wave can take place. Through mode conversion, waves of other types than the

incident wave are formed, such as shear and surface waves forming from an incident compression wave [8].

2.2.2.2 Acoustic Impedance

In most cases, when a sound wave encounters a material boundary or discontinuity, both reflection and refraction (transmission) of energy occur. The amount of energy that is transmitted through the material boundary is based on the relative acoustic impedances of the materials:

$$Z = \rho V , \quad (2-5)$$

where Z is the acoustic impedance, ρ is the density of the material, and V is the acoustic velocity in the material. The amount of energy reflected and transmitted is then governed by Equations (2-6) and (2-7):

$$\text{Reflected Energy} = \frac{(Z_1 - Z_2)}{(Z_1 + Z_2)} 100\% \quad (2-6)$$

$$\text{Transmitted Energy} = 100\% - \text{Reflected Energy} \quad (2-7)$$

where Z_1 is the acoustic impedance of material 1 and Z_2 is the acoustic impedance of material 2.

The acoustic impedance of steel is $46.7 \times 10^6 \text{ kg}\cdot\text{m}^{-2}\cdot\text{s}^{-1}$, and the acoustic impedance of air is $0.0004 \times 10^6 \text{ kg}\cdot\text{m}^{-2}\cdot\text{s}^{-1}$. Thus, at a steel-air interface, such as the test specimen surface or a crack, approximately 100% of the sound energy will be reflected. At the interface between steel and water, approximately 88% of the sound energy will be reflected. For other interfaces between steel and non-metallic inclusions most of the energy will be reflected. This reflection results in an indication of a defect during testing [8]. Compression waves are capable of traveling through any medium be it solid, liquid or gas, thus the amount of energy transmitted across a boundary will follow Equation (2-7). Shear waves, however, are only capable of propagating in solids, as liquids and gasses have no resistance to shearing action. When a shear wave traveling through a

solid encounters an interface with a liquid or gas, all of the sound energy will be reflected back into the solid, as the shear wave is incapable of propagating past the boundary [11].

2.2.2.3 Diffraction

Diffraction is caused by the interference of sound waves and will be produced whenever an incident wave encounters an obstacle in its path [13]. As a sound wave encounters a defect or crack, the crack tip will cause a scattering of the wave, resulting in diffracted waves propagating in a cylindrical manner originating at the crack tip, regardless of the orientation of the defect. This cylindrical wave will have an axis perpendicular to the path of the incident wave [14]. Diffracted waves are of the same mode as the incident wave from which they are formed. Thus, a compression incident wave will produce a compression diffracted wave.

Wave diffraction is caused by a discontinuity of stress across crack faces. Any compressive stress that is high enough to produce significant interaction between the two crack faces will decrease the scattering of the waves. Diffracted waves are of smaller amplitude than incident or reflected waves. Thus, any lessening of the signal can make diffracted waves increasingly difficult to detect during testing. No amount of compressive stress will make the signal from the crack tip completely disappear, but it could be greatly diminished [15].

2.2.2.4 Wave Phenomena Detected in Ultrasonic Testing Methods

When an ultrasonic wave encounters a crack-like defect of finite length, reflection and refraction as well as diffraction from the crack tips will take place [14] as shown in Figure 2.3. A portion of the sound energy will be reflected off of the surface of the crack at an angle equal to that of the angle of incidence. This reflected energy will comprise a large portion of the total energy. Many ultrasonic testing methods rely on the reflection of energy at a crack surface, such as the common pulse echo method, or LPA, which was used in this project. A portion of the sound energy will be transmitted through the crack (refracted). If the crack is air filled, the refracted energy will be negligible. The third phenomenon that occurs when ultrasonic energy encounters a crack is diffraction at the crack tip. In this case, the crack tip behaves as a point source, radiating energy in a

cylindrical manner, over a much larger range of angles than the reflected energy [16]. The amplitude of the diffracted energy is smaller than the reflected energy, but in most cases it is still detectable over any noise in the system. Diffracted waves are used for crack detection in methods such as TOFD.

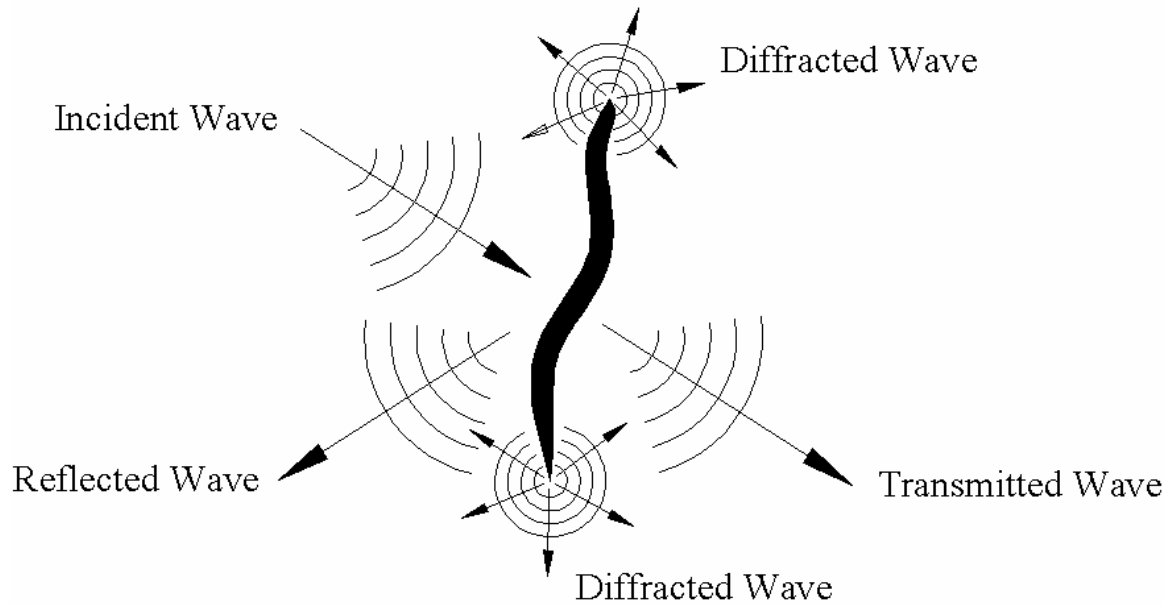


Figure 2.3: Wave phenomena resulting from incident wave encountering crack

2.2.3 Acoustic Wave Attenuation

As a sound wave propagates through a solid, it is subject to attenuation, or a diminishing of the signal. Attenuation is due to both absorption and scattering of sound energy. Absorption is the conversion of sound energy into heat through friction [11]. The higher the frequency of the sound waves the more absorption of sound energy that occurs. Scattering is the reflection of sound waves off of grain boundaries and is more of a problem with coarse-grained materials than fine-grained materials. Scattering results in lost sound energy if these reflections are not detected by the transducer, or added noise if they are detected, which can mask the signal from a defect [8].

Attenuation can weaken the signal returning from flaws and the reflection from the surface opposite that of testing (the back-wall echo), received by the transducer [11]. In order to counteract the effects of attenuation, the proper frequency of testing must be

chosen. Lower frequencies help to counteract the effects of both absorption and scattering. The amount of energy absorbed increases with frequency, thus lower frequencies allow for further penetration of energy [8]. Another option to account for absorption during testing is to increase the amplitude of the sound wave applied to the specimen. Scattering becomes a large problem during testing if the grain size is greater than one-tenth of the wavelength, thus lower frequencies produce less scatter. As low a frequency as possible should be chosen for ultrasonic testing without sacrificing resolution, as the smallest defect dimension detectable is equal to half the wavelength. Attenuation does not greatly affect the use of ultrasonic testing in steel. If the proper frequency is chosen, there will be a sufficiently strong signal in steel for detection of defects [11].

2.2.4 Near Field Versus Far Field

In addition to attenuation, the possible range of testing is determined by the divergence of the beam of sound energy. An ultrasonic testing probe is, in theory, a set of numerous point sources of sound energy which propagate into adjacent media as spherical waves. In the so-called near field, these waves interfere with each other and cause variations in sound pressure, which makes any signal received from the near field during testing unreliable. In the far field, however, the numerous wave fronts combine to support each other, which produces a more uniform pressure intensity than in the near field [9]. The near field distance is found as:

$$NF = \frac{D^2 f}{4V} \quad (2-8)$$

where NF is the near field distance, D is the transducer diameter, f is the frequency of the primary current, and V is the acoustic velocity in the material.

In the near field, the beam of sound is assumed to be cylindrical in shape, whereas in the far field the beam is conical. The beam width increases in the far field with propagation, thus the amplitude of the signal decays exponentially in the far field, reducing the possible range of ultrasonic testing. The divergence of the beam will be the greatest influencing factor in determining the possible testing range in materials that are easily

penetrated, such as fine-grain steel; otherwise attenuation is the predominant factor in determining range [11].

2.2.5 Ultrasonic Testing Equipment

The equipment used in ultrasonic testing is similar for most methods, as described in the following sections. Most ultrasonic testing methods use the same piezoelectric material to construct probes; however the configuration of the material is specific to the method being used. The frequency of testing is also similar across testing methods as this is determined largely by the material being tested. Other materials, such as couplant are commonly used for most ultrasonic testing methods.

2.2.5.1 Piezoelectric Materials

In order to introduce a sound wave into a test specimen, a transducer is used, which converts electrical to mechanical energy and vice versa. Transducers contain piezoelectric materials, which can be naturally occurring mono-crystalline materials, such as quartz, or so called piezo-ceramics which obtain their piezoelectric properties by being polarized in an electric field at elevated temperatures. Piezoelectric materials exhibit two effects which are useful in ultrasonic testing. The direct piezoelectric effect states that when a piezoelectric material is deformed through mechanical pressure, electrical charges will form on its faces. The direct piezoelectric effect is used for probes which receive a signal from the test specimen. Conversely, the inverse piezoelectric effect states that a voltage applied across the faces of a piezoelectric material will produce mechanical deformation. This deformation, on the order of micrometers, is used to transmit sound waves into adjacent material. The transducer typically consists of a piece of piezoelectric material to which thin metal plates are applied in order to introduce or detect a voltage across the faces [11].

To introduce oscillations into the test specimen, an alternating voltage is applied across the transducer. The transducer will vibrate at the same frequency as the alternating voltage. When the transducer is placed on the test specimen, an ultrasonic wave is introduced with amplitude proportional to the applied voltage. Depending on the orientation of the piezoelectric material in the transducer, either compression or shear

waves will be introduced into the material. Then, when a sound wave encounters a receiver transducer, the alternating stresses applied to the piezoelectric material by the wave produce a voltage across the faces of the transducer, which acts as a microphone to detect sound waves [11]. Piezoelectric elements can be considered either resonant, or non-resonant. Non-resonant elements can be used over a wide range of frequencies. These non-resonant elements are generally used at frequencies below their resonant frequency. If it is desired to use the non-resonant element near resonance, high damping is used. Resonant elements, however, are designed to be used at a specific frequency, resonance, or a small band of frequency surrounding resonance. Most transducers used for ultrasonic testing are resonant elements [10].

2.2.5.2 Frequency of Testing

In general, ultrasonic testing is done with frequencies ranging from 200 kHz to 50 MHz. Frequencies ranging from 200 kHz to 20 MHz are used for defect detection, while higher frequencies are used to investigate material properties [9]. When testing steel specimens, the frequency of vibration used is generally 5 MHz or less, otherwise the ratio of the grain size to the wavelength is large enough to produce unwanted scattering of energy. The 5 MHz sound wave produces a wavelength of 1.2 mm in steel [11]. As the smallest flaw that can be detected through ultrasonic testing is equal to half the wavelength, there is generally sufficient resolution at 5 MHz for most flaw detection applications. The resolution found using shear waves will be higher than that using compression waves due to their smaller wavelength.

2.2.5.3 Additional Testing Equipment

For both the linear phased array and the time of flight diffraction methods, the transducer is mounted on an angled probe so that ultrasonic waves are introduced into the material at an angle other than 90° from the test surface. It has been shown that the angle that produces the largest amplitude for compression waves is between 60° and 70°. The optimum angle for the introduction of shear waves is between 40° and 50° [17].

Couplant is needed between the transducer and the test specimen in order to introduce the sound wave into the specimen. If no couplant was used, the sound wave from the

transducer would need to pass through a layer of air between the probe and the material being tested. At the boundary between the probe and the air layer, most of the energy would be reflected back into the probe, allowing very little to pass into the air. Then, another boundary is found between the air and test material which also would not allow for the transmission of sound energy. Common couplants are water, oils with medium viscosity such as SAE 30, and glycerin. Most couplants have a 10% to 15% transmission rate. Glycerin has the highest transmission rate of common couplants at 15% due to its high acoustic impedance [8].

2.2.6 Pulse Echo Method

The most common method of ultrasonic testing is pulse echo. In this method, a sound wave is introduced into the material by a probe. When this wave encounters a defect, a portion of the sound energy is reflected back to the probe and the defect is detected.

The pulse echo method relies heavily on the proper placement and orientation of the probe relative to the defect for its detection, as seen in Figure 2.4. If the defect and probe are not properly oriented with respect to each other, the incident sound wave could be reflected away from the probe, and the defect would be more difficult to characterize. If the sound energy is directed away from the probe due to an unfavorably oriented defect, the back wall echo will be affected, indicating to the operator the possible existence of a defect. However, if the defect is oriented parallel to the probe, the back wall echo would not be affected and the crack could go undetected. Thus, it is common for an operator to use several probes or varying angles of incidence during testing to increase the probability of crack detection.

During testing, the amplitude of the reflection is recorded versus travel time. If the defect is smaller than the diameter of the ultrasonic beam introduced into the test specimen, the size of the defect can be estimated by comparing the amplitude of the reflected signal to the signal resulting from a standard reference reflector. The difference in the two signals, called the decibel drop, is used to determine the size of the defect. In order to accurately size the defect using the pulse echo method with a standard 90° probe, the crack must be in a plane parallel to the surface at which the ultrasonic wave was introduced, the surface

roughness cannot be larger than $5\ \mu\text{m}$, and the defect must be in the far field of the beam. If the defect is much larger than the sound beam, the size of the defect can be determined by tracing the outline, independent of relative amplitude [10].

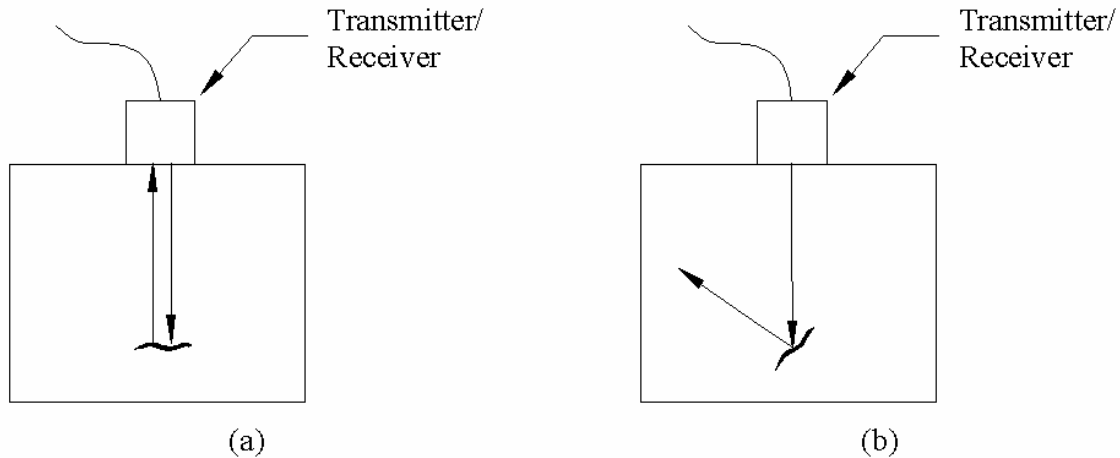


Figure 2.4: Pulse echo probe with (a) favorable orientation relative to defect (b) unfavorable orientation to defect

2.2.7 Phased Array Method

The phased array method of ultrasonic testing utilizes the basic principles of pulse echo testing. However, unlike the pulse echo method, which uses only one transducer, a phased array uses many transducers working simultaneously to focus sound energy at a specific point in the test specimen. These transducers are arranged into a single probe which is used for both transmission and reception of the signal. By using a phased array, the operator is better able to determine the size, shape and orientation of a defect versus traditional pulse echo techniques [10].

In the phased array method, the sound energy from the various transducers combines through constructive and destructive interference [18] to create a unified wave front which can be manipulated to focus at desired locations in the test specimen. In order to scan the prescribed area, the ultrasonic beam can be moved electronically. Thus, different inspection configurations can be completed with little to no physical probe movement. A picture of the area of interest, called a sectorial scan (S-scan), can be created by sweeping the ultrasonic beam through a range of angles, rather than using a raster scan of an individual transducer as in the pulse echo method. To control both the

shape and direction of the ultrasonic beam, the firing of each transducer is carefully timed. With a carefully defined focal law, or the combination of firing times for all of the transducers in the array, the ultrasonic beam can be electronically moved to focus at any depth, or sweep through a prescribed range [19]. This wave front can be electronically steered laterally from $\pm 20^\circ$ to $\pm 80^\circ$ from the center element, depending on the frequency of testing and the element configuration [20]. Reception of an ultrasound signal from a phased array is then the opposite of transmission. The signals received at each element must be delayed before they are combined in order to realize the steered and focused beam [21].

Several configurations of transducers can be used in the phased array method. A linear phased array consists of several transducers arranged in a one-dimensional line, as seen in Figure 2.5. Alternatively, transducers can be arranged in a two-dimensional grid called a planar array, or a two-dimensional set of concentric circles called an annular array. Linear arrays allow for beam movement and focusing in only one direction, either laterally or through the cross section. This limited movement of linear arrays is generally all that is necessary for most applications [21], thus it was the method used for this project.

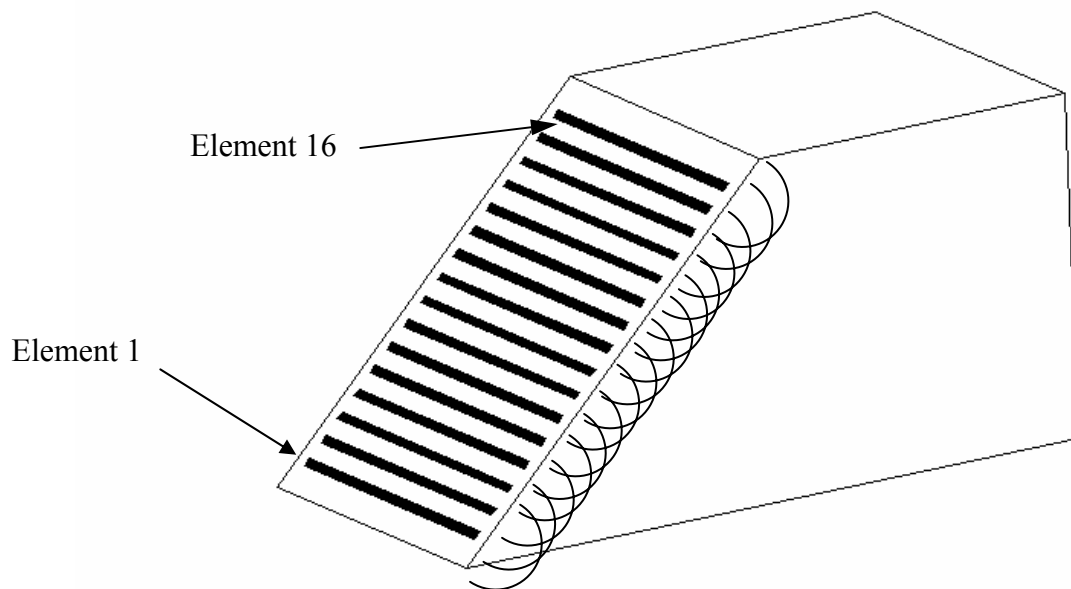


Figure 2.5: Linear phased array probe with 16 elements

Each transducer in an array can be modeled as a point source. When electrically excited, each of these point sources is assumed to produce a cylindrical shear wave which has a constant phase at a given distance from the center of the transducer. Shear waves are used for phased array testing as they have a higher resolution than compression waves. By correctly timing the ultrasonic transmission of each of the transducers in the array, firing first the outer elements and working inward, a unified wave front can be created, as shown in Figure 2.6. In reality, the wave may not behave as modeled when the size of the elements is larger than half the wavelength, $\lambda/2$, of the ultrasonic pulse. With these larger elements, a distinct near and far-field are created which have phase distributions that are unlike an ideal cylindrical source, where the phase is constant, however beam focusing and steering are still possible. Elements with a dimension less than $\lambda/2$ are often too small to be practical, thus it is still common to use larger elements with a dimension greater than $\lambda/2$ with little ill effects [22].

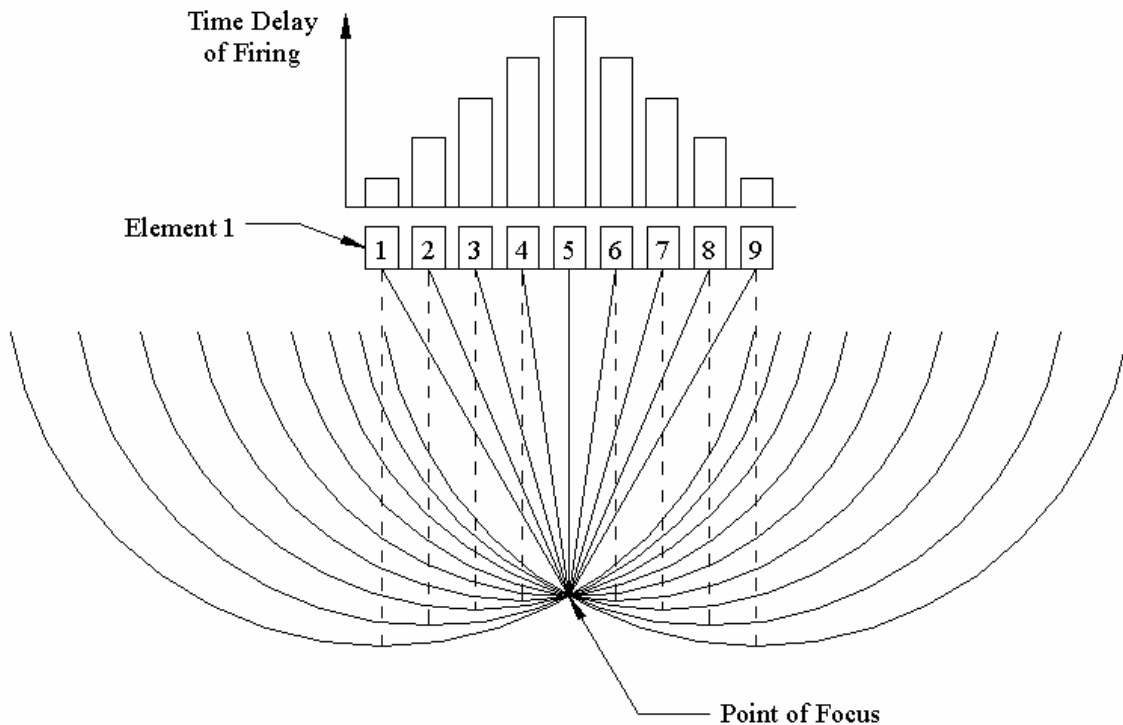
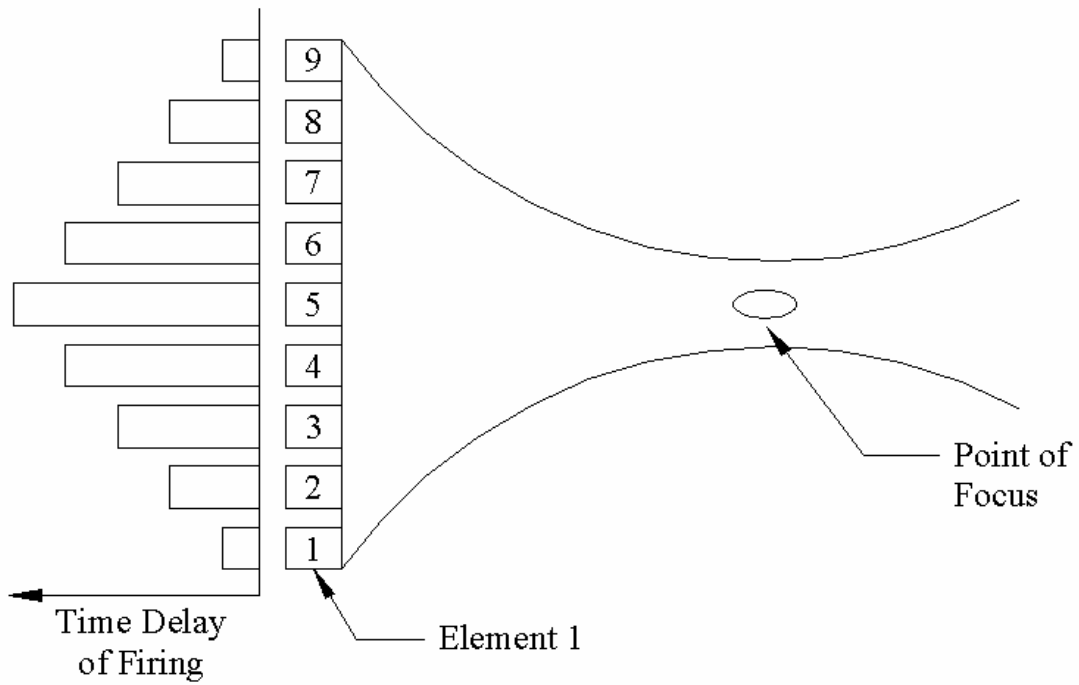


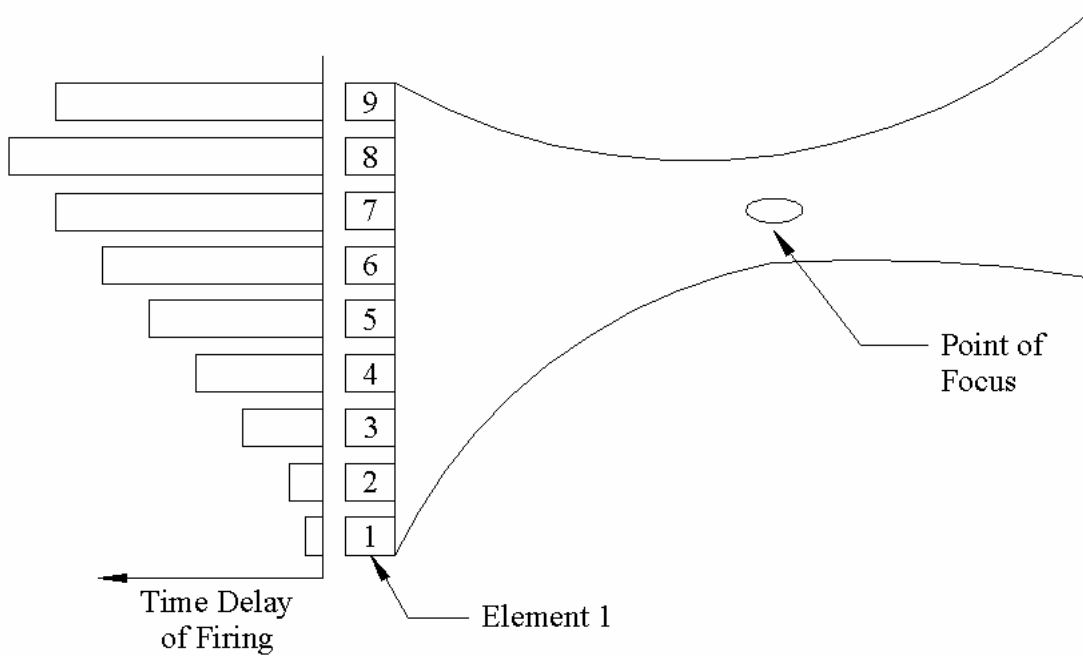
Figure 2.6: Constructive interference of sound waves forming focused beam in linear phased array testing

Focal laws must be created to transmit and receive phased array signals. These focal laws consist of both a delay law, which defines the set of time delays of each element, and the amplitude law, which defines the gain, or amplification of signal, of each element. A focal law can be created by first tracing a line from the center of each element to the point of interest in the test specimen. Then, the time needed for each element to transmit energy to the desired point is determined and becomes the basis for a delay law. Equations used to determine the firing times of each element in a phased array given the distance and angle to the desired point of focus can be found in Huang [23]. Example delay laws are shown in Figure 2.7. By changing focal laws during testing, the operator can sweep the ultrasonic beam through an area without moving the probe. While beam steering is useful for areas of complex geometry, for simpler test specimens, such as a weld lying in a plane, it may be unnecessary to investigate a wide range of angles. In these cases, it is common to use phased array probes in a static mode, where a single delay law is used for scanning along a flat surface, focusing the beam at a constant angle and depth from the surface while the probe is drawn along the length of the area of interest, such as a weld.

In standard phased array focusing techniques, only one focal law is used for transmission and reception of the ultrasonic signal. Standard phased array focusing tends to ignore potential reflectors or defects that are outside the focal area. This shortcoming can be overcome by using dynamic depth focusing techniques. Dynamic depth focusing uses one focal law for the transmission of ultrasound, as in standard focusing. However, dynamic depth focusing uses multiple focal laws for the reception of signals. By using more than one focal law for reception, the focal point is effectively moved through the depth of the region of interest in order to increase the likelihood of defect detection. With dynamic depth focusing, the depth of field is increased by a factor of four, and the signal to noise ratio is increased over standard focusing techniques [24].



(a) Focusing of beam



(b) Steering of beam

Figure 2.7: Delay laws for linear phased array testing

2.2.7.1 Linear Phased Array Transducer Design

To create a linear phased array set of transducers, a single piezoelectric element is cut into individual elements, or slotted, to form an array of transducers. These arrays are typically 13 to 25 mm long consisting of 16 to 64 elements, however upwards of 512 elements can be used. It is optimal to use between 20 and 30 elements in a linear phased array. Using less than 20 transducers in an array reduces the resolution of the testing method, while using more than 30 transducers achieves little increased resolution [10,25].

The array of transducers in a phased array configuration emits energy in all directions, not just the direction of interest. This energy is concentrated into a series of locations, or lobes. The main lobe, which is of high amplitude, is produced in the direction of the steering angle. A narrow, well-defined, focused main lobe is necessary for high resolution and probability of detection. A grating lobe, which is of similar amplitude to the main lobe, is created in the direction perpendicular to the main lobe. The grating lobe can create strong signals in directions other than the steering angle, confusing test results, thus small amplitude grating lobes are desirable. Side lobes exist between the main and grating lobes, which are caused by energy leaking from the main lobe. Although side lobes are smaller in amplitude than the main lobe, it is beneficial to suppress these lobes to avoid confusing signals [26].

Woo [26] performed computational modeling of phased array transducers. Through this modeling, it was found that the relative amplitude of the lobes is dependent upon the number of elements used, element width, and spacing. An increase in the number of elements used in the array will increase sharpness and resolution of the signal. Arrays with large numbers of elements have an increase in the main lobe sharpness, a higher overall sound pressure, or strength of signal resulting in a higher signal to noise ratio, and exhibit suppression of side lobes. However, arrays with large numbers of elements are more complex to control and more expensive to manufacture than arrays with fewer elements. Also, by increasing the number of elements, the near field zone is increased making it more difficult to detect cracks near the surface of the specimen. Increasing the size of individual elements will also create a higher sound pressure. Wider elements, however, tend to create an increase in side lobe amplitude resulting in a lesser-defined

main lobe. For the design of arrays, inter-element spacing should always be less than one-half the wavelength used in testing to avoid grating lobes. The element width should always be smaller than the inter-element spacing. Wooh determined that, in general, an array consisting of 16 transducers with the largest possible element size, spaced at less than $2/3$ of the wavelength will perform optimally.

2.2.7.2 Linear Phased Array Output

Linear phased array testing produces a wedge shaped scan image, as seen in Figure 2.8, similar to those seen in medical ultrasound [27]. This two-dimensional scan, called an S-scan, depicts the material cross section at one probe location. For a single delay law, or angle of focus, the amplitude of signal versus time is recorded. Then, as the beam is swept through a range of angles, the amplitude versus time data is compiled for the entire cross section into a two-dimensional S-scan. A color scale represents the amplitude of the signal. Any defect encountered will cause a change in amplitude of the received signal, which would appear as an area of color other than the standard background color on the S-scan. The S-scans for all locations can be analyzed to detect and size defects. As seen in Figure 2.8, cursors are placed on the scan to aid in locating and sizing the defect.

2.2.7.3 Phased Array Detection Trials

Various researchers have performed trials for the detection of defects using the phased array ultrasonic testing method. Flaw depth measurements as accurate as 0.25 mm have been reported, if the defect can be detected above the noise level [20]. Much of this research has been performed for the nuclear power industry interested in inspecting welds in various locations on pressure water reactors constructed from low alloy carbon steel and stainless steel.

Inspection trials were performed on internal welded joints of boiling water reactors (BWR) used in nuclear power plants by Komura [28]. The test specimens contained artificial defects, side-drilled holes, machined slits and stress corrosion cracking. In these trials, Komura used a 256-element phased array probe. The experimental results were found to closely match the machined crack depths.

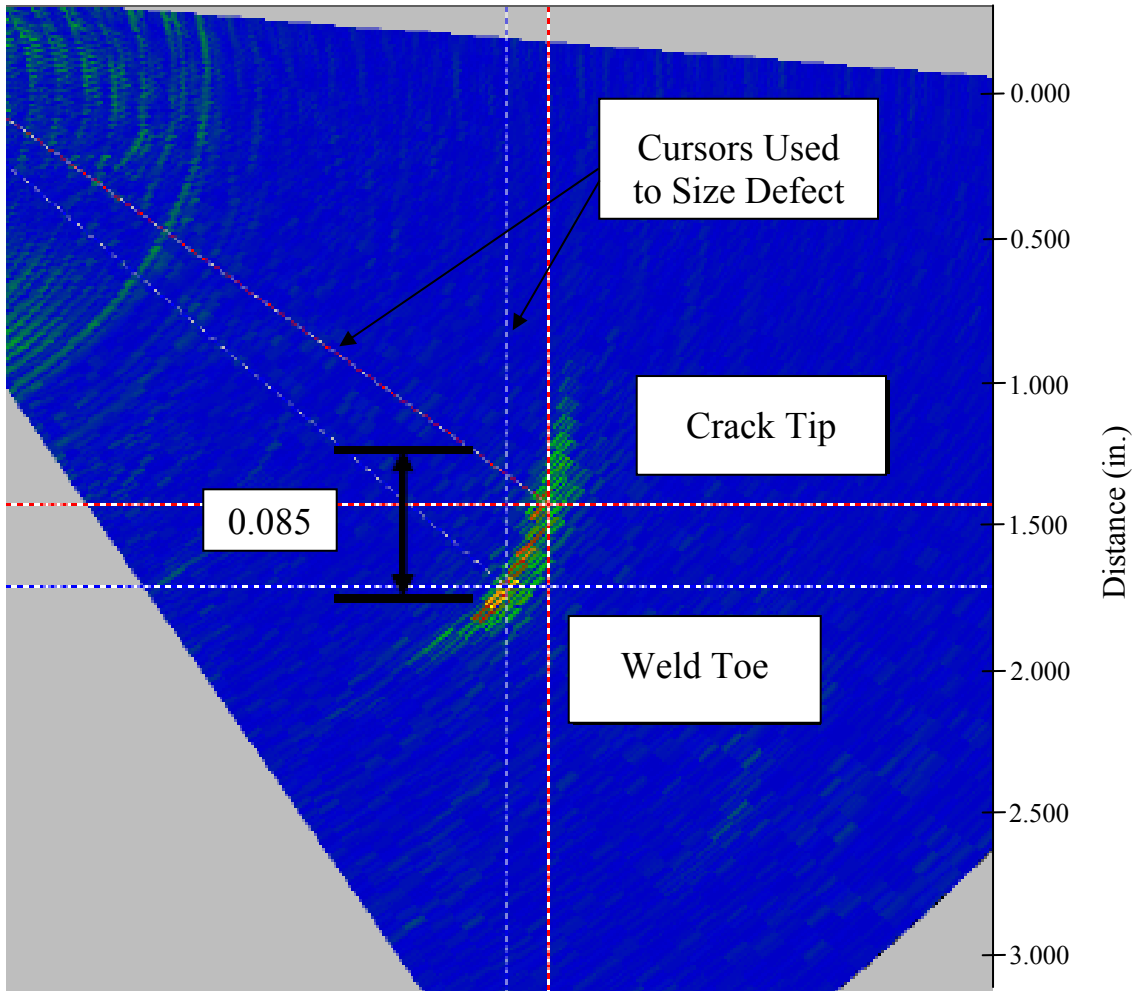


Figure 2.8: Linear phased array S-scan

Shipp [29] investigated the reliability of the phased array method for the detection of defects in the fillet welds of boiler beam support brackets which support boiler tube structures and are attached to the outer shell of boilers found in power stations. For this application, the method needed to reliably detect defects with minimum dimensions of 1.5 mm wide by 10 mm long. Also, the defect dimensions needed to be estimated within 1.5 mm of their size. Blind trials were conducted by three pairs of data analysts, where the teams were given sample specimens which contained defects, but were not told the quantity, location, or size of the defects. One member of each pair was responsible for data collection, while the other member performed the data analysis. After the appropriate training of each of the data analysts, the experimental results met the required detection standards.

Mahaut [30] performed inspection trials using the phased array technique on thick cast stainless steel. Specimens were prepared with artificial defects, such as machined notches and drilled holes, to simulate defects found in cooling components of pressurized water reactors. Using two matrix array probes, each with 3 x 12 elements, in a tandem mode with one transmitter and one receiver, it was found that defects of height between 3 mm and 15 mm were detectable over a reasonable signal-to-noise ratio. It was also found that all defects over 10 mm in height could be accurately sized using this method in the 70 mm thick specimens.

MacDonald [27] investigated the capabilities of the phased array method for the detection and sizing of defects in piping welds. These dissimilar metal welds are used to join a low alloy carbon steel reactor pressure vessel to stainless steel piping. A matrix array probe with 10 x 3 elements was used to search for both circumferential and axial flaws in the weld. An extensive electronic scan pattern was used to limit the physical movement of the probe. The depth of the circumferential defects was found within an average of 0.48 mm of the depth of the crack, with the length being estimated within 3.84 mm of the crack length. The depth of crack ranged from 4 mm to 45 mm, with lengths from 12 mm to 145 mm. MacDonald had similar accuracy in sizing axial flaws in the weld with depth of 5 mm to 20 mm and length between 5 mm to 16 mm with an average error of 2.87 mm in depth and 0.38 mm in length.

Mahaut [30] and Shipp [29] both report the ability to detect machined defects larger than a given size with reasonable accuracy. Shipp was able to size defects with errors less than 1.5 mm. MacDonald, however, was not able to achieve consistent results, with errors differing greatly for the two flaw types. When measuring circumferential flaws, MacDonald was able to achieve accuracy much greater than Shipp for the depth of the crack, but had error more than two times larger than Shipp in length sizing. MacDonald found the opposite results when sizing axial flaws with much greater accuracy in sizing the length rather than the depth of the flaw.

Choqueuse and Lamarre [19] investigated the feasibility of using the phased array method for the detection of fatigue cracks in welded tubular joints made of low alloy

carbon steel in offshore structures. Fatigue cracks of depth between 2 mm and 5 mm were introduced into specimens of 22 mm thick steel in a tee butt joint configuration. Then, four different configurations of 16-element phased array probes were used to estimate the extent of cracking. The size of cracks was compared to dimensions found using the alternative potential drop method, an electromagnetic method of non-destructive testing. For the phased array technique used which produced the most accurate results, the estimated depths of the cracks were all within 3 mm of the depth measured by the alternative potential drop method. This reported error in depth sizing is twice as large as that found by Shipp [29], suggesting that there is a large difference in the detection capabilities of the phased array method for fatigue cracks versus machined defects.

2.2.8 Time of Flight Diffraction Method

The time of flight diffraction method (TOFD) of ultrasonic testing attempts to overcome the difficulties associated with defect orientation of the pulse echo method. TOFD does not depend on the orientation of the defect for detection, and detection capability is independent of the amplitude of the received signal. This allows for improved accuracy in the quantification of the defect encountered, such as the size and through thickness extent, over traditional pulse echo methods [31].

The TOFD method relies on the detection of diffracted waves originating at crack tips in the path of the incident wave, rather than reflected waves off of a crack surface. As such, TOFD is capable of detecting defects independent of their orientation in the test specimen. This method allows for accurate estimation of the crack location, size and orientation [32]. However, the TOFD method is most accurate in determining the dimension of a defect that is oriented perpendicular to the surface of the specimen containing the transducers [14], which is the typical orientation of fatigue cracking found in ship structures. This is unlike pulse echo methods which are most accurate in sizing cracks parallel to the surface containing the transducer.

Instead of using amplitude to estimate various crack characteristics, the TOFD method uses only the transit time of the diffracted wave to size a crack. The amplitude of a

received signal can be affected by many material parameters, making amplitude dependent defect sizing methods somewhat inaccurate and unreliable. Such amplitude affecting factors include the surface roughness of the test material, the coupling efficiency or temporary loss of coupling, the orientation of the defect, and performance of the ultrasonic testing equipment itself [33]. By depending only on transit time, which is a reliable quantity, TOFD is more accurate in sizing defects than amplitude dependent methods. When using TOFD, the amplitude of the received signal cannot be completely ignored, however, as the signal must be of amplitude great enough to be observed over any noise in the system [14].

In general, two probes are used for TOFD which work together in a directly opposed configuration, one probe transmitting the sound wave with the second probe acting as receiver. In TOFD, the signal received by the probe is amplified in order to detect the waves resulting from the crack tips for defect detection. TOFD uses compression waves in testing, thus the diffracted waves will also be compression waves. Shear waves, which have a greater resolution than compression waves, can be used for TOFD, but as they have a slower velocity, the shear waves arrive at the receiver probe amid various mode-converted waves making it difficult to distinguish a signal from a defect from other waves with similar arrival times.

When using compression waves, the transmitter and receiver probes should be spaced such that the back-wall echo, or the reflection from the opposite surface of the test specimen, arrives before any mode converted waves. Then, the various waves of interest are easy to distinguish and arrive in a predictable manner [15] as shown in Figure 2.9. First, the lateral wave will arrive at the receiver probe. The lateral wave represents the most direct path from the transmitter to the receiver generated by the edges of the ultrasonic beam. Generally, the lateral wave will flow along just under the test surface, however if the surface of the specimen is curved, the lateral wave will take a straight path between the two transducers. After the lateral wave, any diffracted waves arising from a crack tip will arrive followed by the back-wall echo. The lateral wave and back-wall echo occur in a predictable manner with a consistent time delay [34]. Thus, if the probes are spaced appropriately, the lateral wave and back-wall echo form natural reference

signals between which any indications of a defect must appear. Any wave arriving after the back-wall echo is a mode converted wave that generally is ignored.

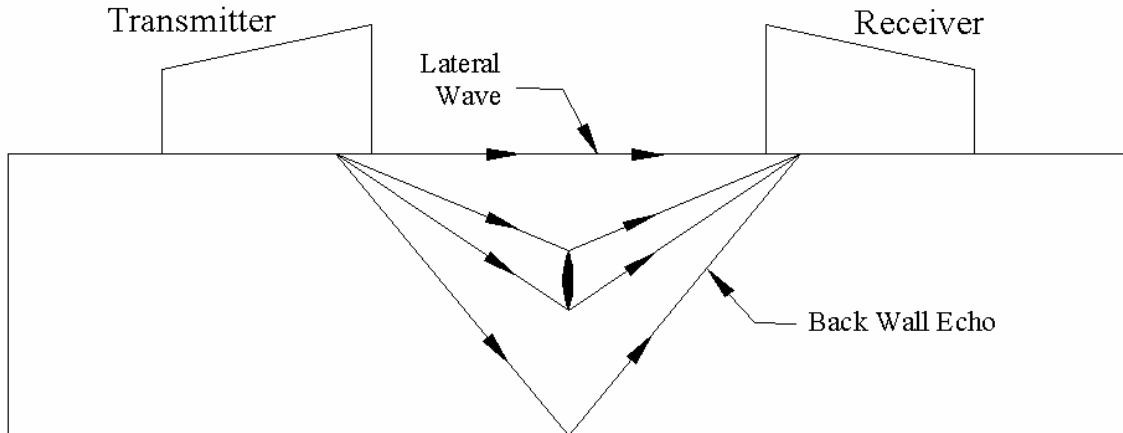


Figure 2.9: Ultrasonic waves detected during TOFD testing

The signals from the upper and lower tips of the crack can be distinguished by two characteristics. First, the two signals will be opposite in phase. Also, the signal received from the lower crack tip will likely be stronger than the signal received from the upper crack tip. The higher strength of the signal from the lower tip of the defect is due to the shape of a typical defect as viewed from the probe location. The lower crack tip is concave, which acts to focus the acoustic energy. The upper crack tip is convex and produces no focusing effect, thus this signal is weaker than the signal from the lower crack tip. The signal from the lower crack tip tends to be less sensitive and vary less with defect position than the indication of the upper crack tip. This allows for great accuracy in the estimation of the through-wall extent of the defect [14].

If the defect is surface breaking, either the lateral wave or the back-wall echo can be interrupted. When the defect breaks the upper surface, which contains the probes, the lateral wave will be reduced, possibly eliminated. If instead, the defect is open to the back surface, the back-wall echo will be affected. As the back-wall echo is a much stronger signal than the lateral wave, it is less likely to disappear than the lateral wave. The back-wall echo can be skewed for small cracks. For larger cracks the back-wall echo may be delayed, or for very large cracks possibly eliminated [35].

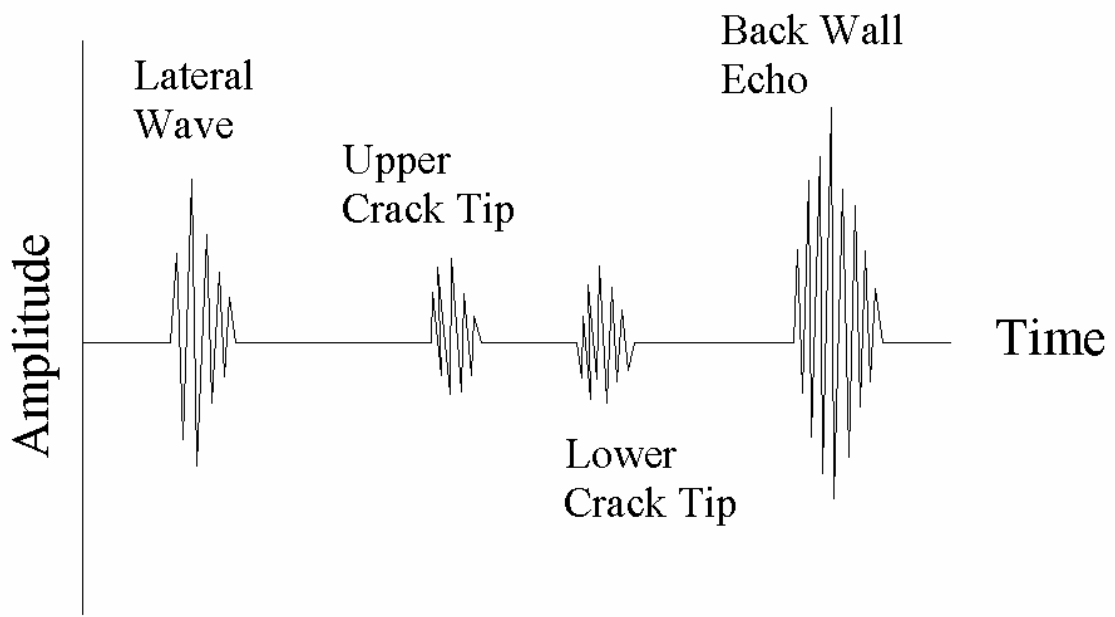
2.2.8.1 Time of Flight Diffraction Output

The output from TOFD testing can be displayed in either a one- or two-dimensional representation. The most basic TOFD output format is the A-scan, which is a one-dimensional representation of a single position of the transducers on the test specimen. In an A-scan, the signal received by the transducer during TOFD testing is plotted as amplitude versus time.

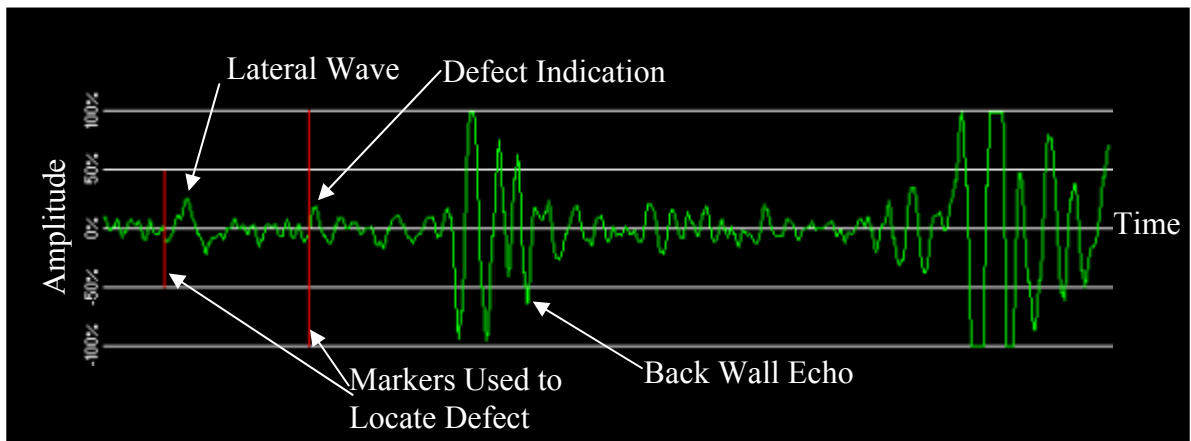
The back wall echo determines the length of the A-scan. Only the signals received by the transducer between the lateral wave and the back wall echo are considered, as these would be an indication of a defect. Figure 2.10 shows a typical A-scan with an indication of a defect. The operator has placed markers at both the lateral wave and the indication of a crack tip in Figure 2.10(b) to aid in locating the defect. It is not possible to determine the exact position of the defect using an A-scan. With an A-scan, both the depth and position of the crack lying in the plane containing the transducers are unknown. These two quantities are related, however. The defect must lie on an ellipse, of which the transducer locations are the foci [13]. A defect placed at any location on this ellipse will produce the same time delay of signal, as seen in Figure 2.11 where the path length from the transmitter to any point on the ellipse and then to the receiver is equal. Thus, it is not possible to determine the location of the defect from only one A-scan. The location of the crack tip can be determined by monitoring the delay time of the signal as the transmitter and receiver probes are moved across the specimen. The delay time will reach a minimum when the defect is centered between the probes [13], as seen in Figure 2.12. Once the crack tip is located, the defect depth can be determined as [32]:

$$d = \frac{1}{2} \left(V_c^2 t^2 - (2S)^2 \right)^{1/2} \quad (2-9)$$

where d is the depth of crack tip from the inspection surface, V_c is the compression wave velocity, t is the arrival time of the signal, and $2S$ is the probe separation. Estimates of error in depth determination are discussed in [36].



(a) Theoretical A-scan with no noise in signal



(b) A-scan with realistic noise

Figure 2.10: A-scan representation of TOFD

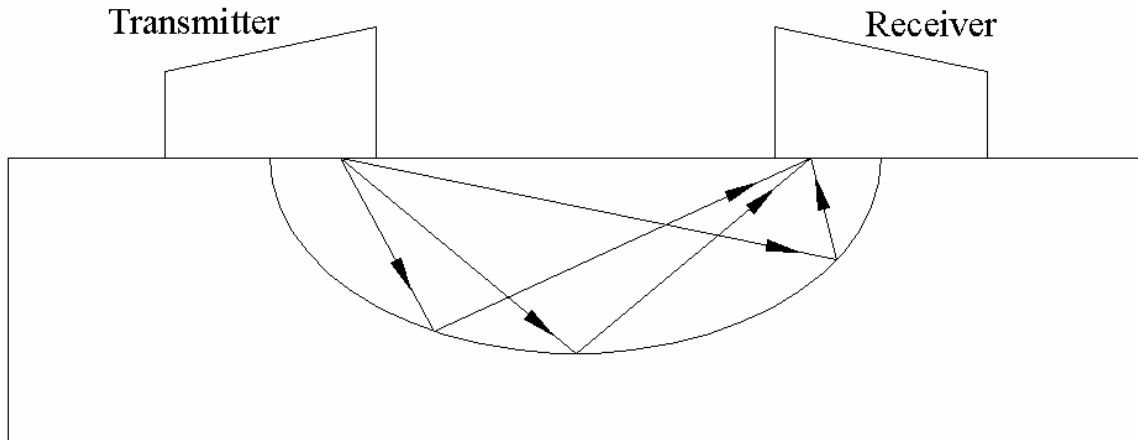


Figure 2.11: Indication with given time delay lies on ellipse with location of transducers as foci

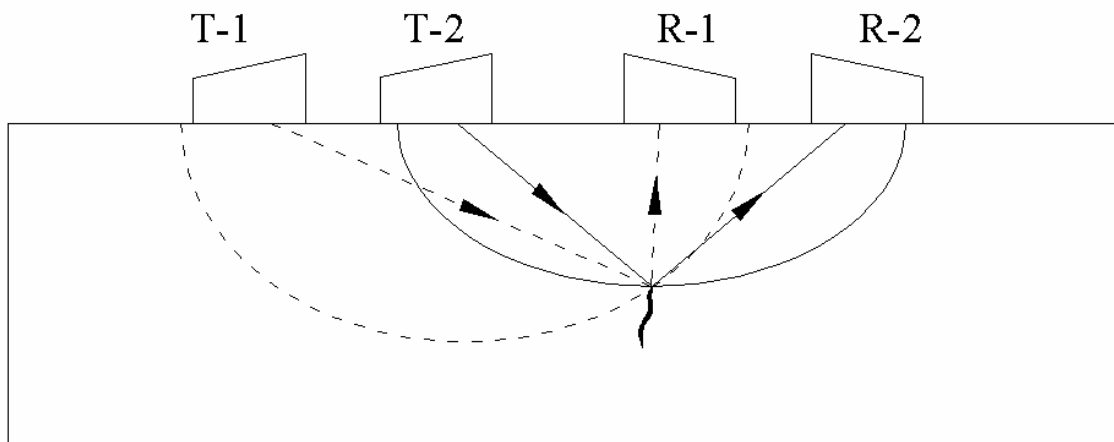
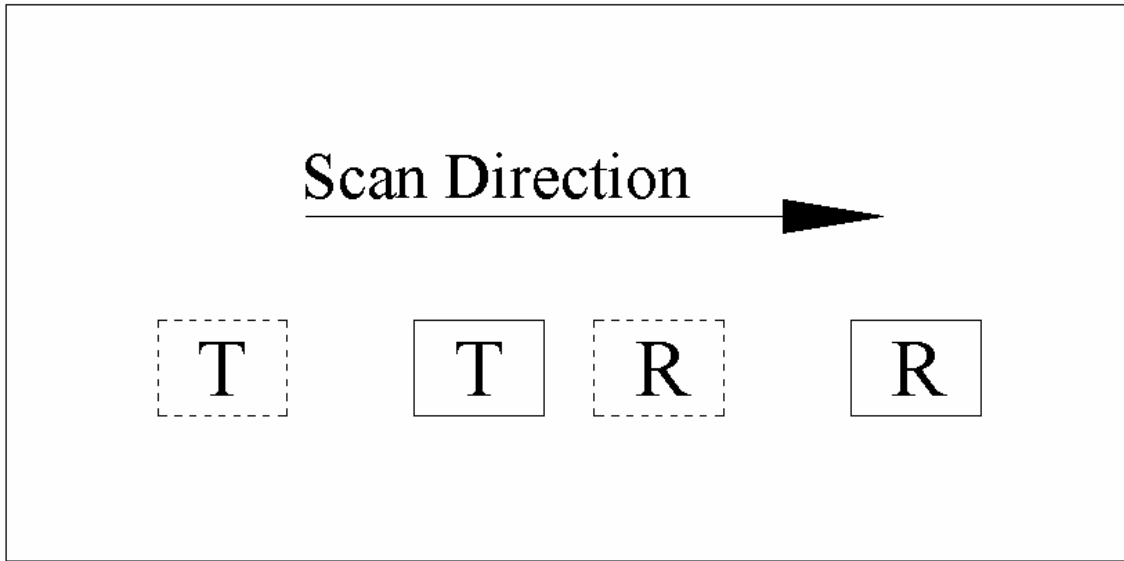


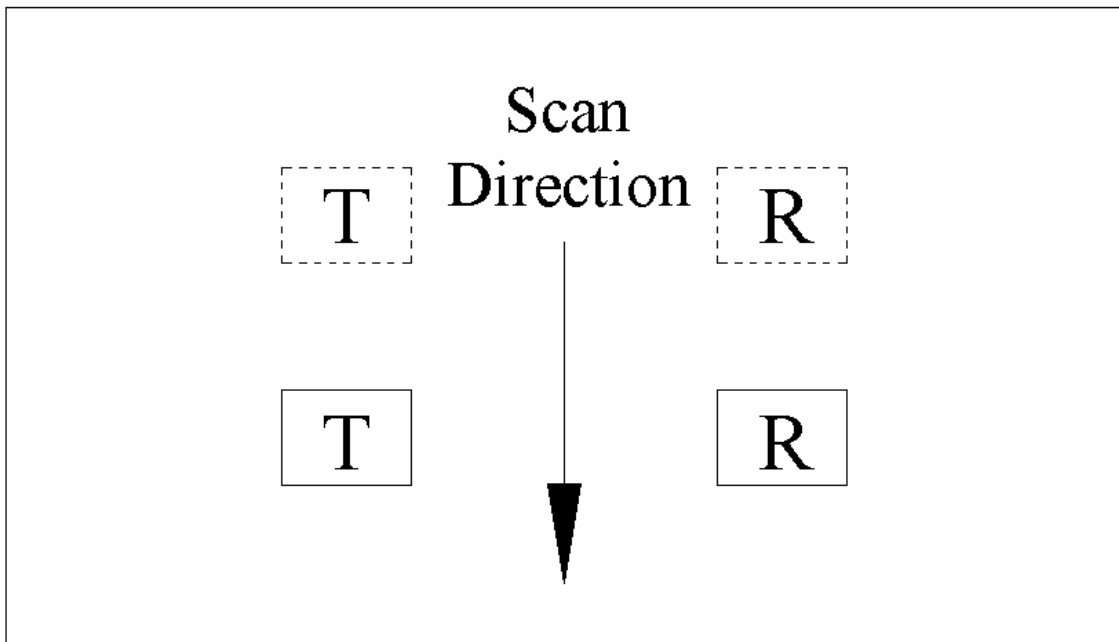
Figure 2.12: Minimum time delay for cracks reached for transducer pair T-2 and R-2, as defect is centered between probes

A-scans are the basis for all other forms of TOFD ultrasonic data display. By combining many A-scans, a two-dimensional representation of the test specimen can be created. These two-dimensional scans are formed by aligning many A-scans as the probes are moved across the specimen surface to include position in the output data, and are representative of a cross section of the test specimen. A B-scan is formed when the probes are moved parallel to the line between the transducers, as shown in Figure 2.13(a), whereas moving the probes perpendicular to the line between the transducer forms a D-

scan [37], shown in Figure 2.13(b). As with the A-scan, the useful length of the B- or D-scan is determined by the back wall echo.



(a) B-Scan



(b) D-scan

Figure 2.13: TOFD scan directions

A B- or D-scan is viewed as a gray scale image with axes representing time delay of the signal versus position of the transducers, as shown in Figure 2.14. The intensity of the shading is related to the amplitude of the signal at a given point. White or black areas on the scan both denote signals of high amplitude, opposite in phase. Any sudden change in intensity of gray indicates an incoming signal, such as that from a defect. The lateral wave will appear as a line at the beginning of the scan. The back-wall echo, which is of greater amplitude than the lateral wave, will be indicated by a series of black and white stripes at the end of the scan [37]. Defects will appear as arc shaped indications between the lateral wave and back wall echo. These arcs are not the shape of the detected defect; instead they indicate the tips of any flaws in the specimen. The lateral position of the flaw tip is found by locating the apex of the arc. At the apex, the defect tip is in the center of the transducer pair, where the delay time is minimized. A B- or D-scan displays time delay, rather than position in the cross section of the specimen; however the defect depth can be determined from the time delay for a given material with a known compression wave velocity [13]. Also, a C-scan can be created, which represents a two-dimensional plan view of the specimen.

B- or D-scans can be viewed in real-time while in the field. When performing TOFD, these scans can be monitored for any gaps in the data, which would indicate a loss of good coupling. Once identified, this problem can be corrected and the gaps in data can be filled [34].

Defect locating and sizing is done manually using the B- or D-scan. The scan is studied to locate any defect indications. Once an indication is located, the operator places a cursor at the apex of the arc, as shown in Figure 2.15. The depth of the defect can be found using the time of flight of the indication in Equation (2-9) as compared with a reference wave, either the lateral wave or back wall echo. The accuracy of defect sizing is dependent on the resolution and quality of the scan and on individual operator capabilities.

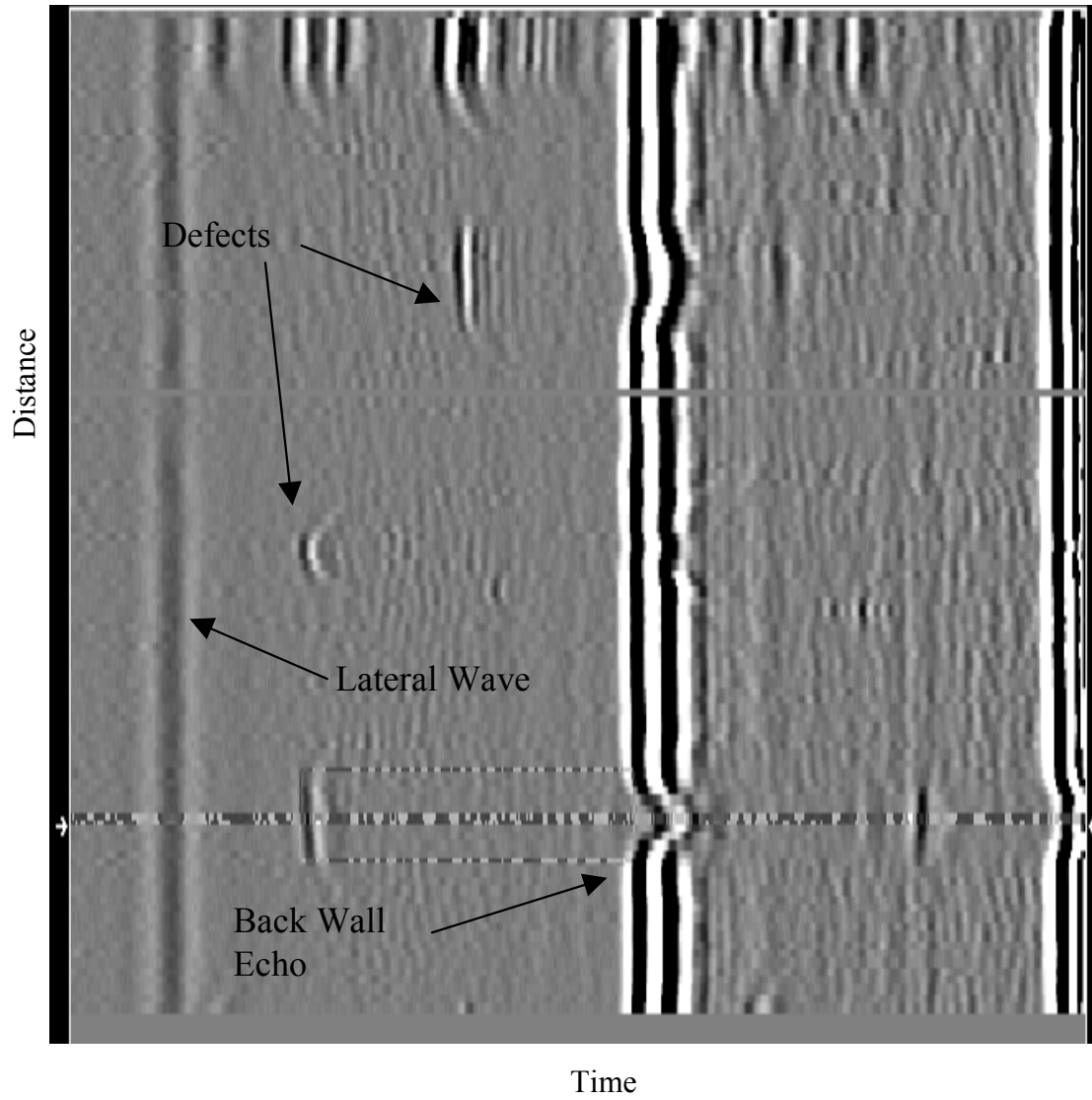


Figure 2.14: Typical TOFD B-scan with defect indications

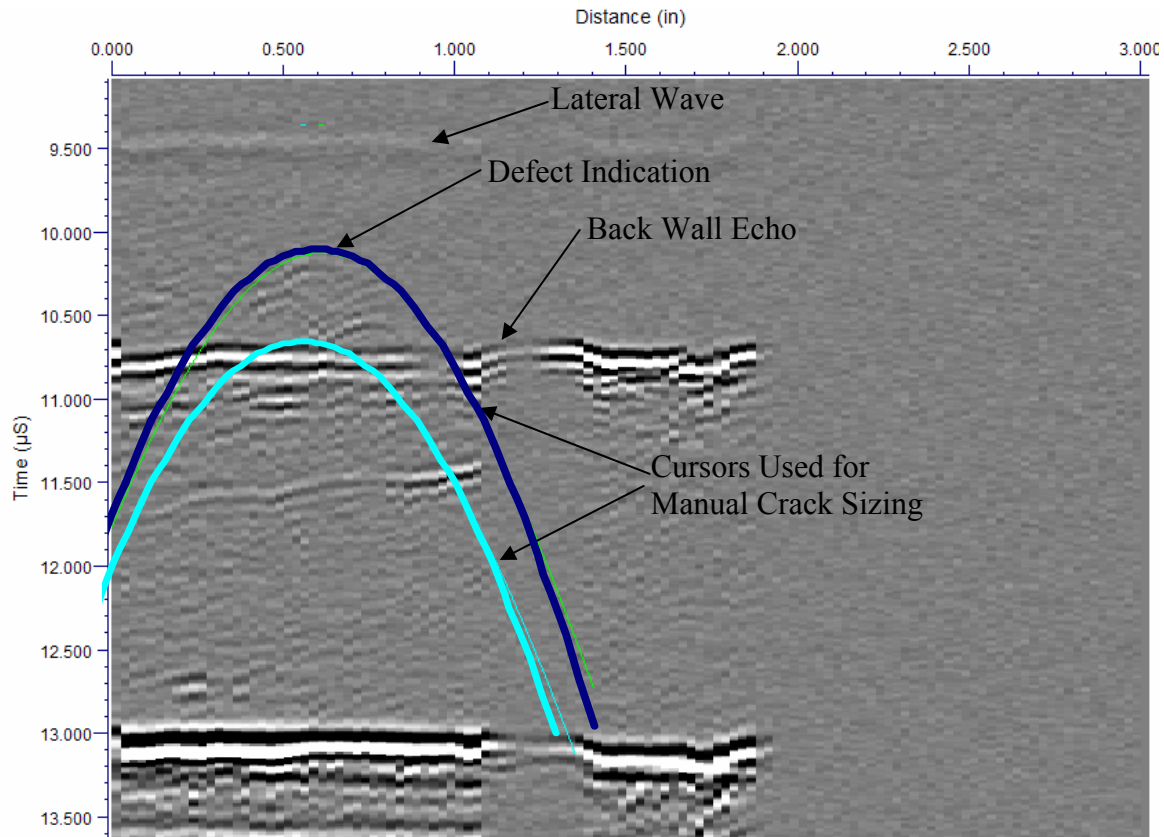


Figure 2.15: TOFD B-scan with indication at upper cursor

2.2.8.2 Detection of Fatigue Cracks Using the Time of Flight Diffraction Method

The scattering of an ultrasonic wave at an interface, such as a defect, is caused by a discontinuity in stress across the crack faces. However, if the crack is under a compressive stress, there will be interaction between the crack faces that may reduce the difference in stress across the faces, depending on relative surface roughness and contact area between the faces. This interaction can allow large amounts of acoustic energy to pass through the interface. Through transmission will increase as either surface roughness decreases, or the frequency of the test signal is increased [38]. When there is an increase in energy that can pass through an interface, the reflected or diffracted energy from a defect will decrease making detection more difficult. The closed defect becomes effectively transparent or semi-transparent to ultrasonic beams [17]. This interaction between crack faces can be a problem in the detection of fatigue cracks.

Fatigue cracks inherently produce relatively small amplitude signals during ultrasonic testing because of crack closure, the variation in depth of the crack along its length and a

rough surface, all of which can produce scattering of ultrasonic energy [33]. This scattering produces a small signal-to-noise ratio making fatigue cracks much more difficult to characterize than wide, machined slits. As the crack tip opening displacement (CTOD) of a fatigue crack decreases, the amplitude of the diffracted wave decreases [39,40]. Decreased amplitude becomes problematic for detection of cracks with thickness less than $\frac{1}{2}$ micron [13].

The amplitude of diffracted signals from closed cracks can be lower by tens of decibels than open cracks. A significant reduction in signal received from fatigue cracks can be found when the crack is subjected to a compressive stress equal to 20% of the material yield stress. The signal from the crack will continue to decrease as the compressive stress increases. While the signal will never completely disappear, it can decrease to a level similar in amplitude to the noise level [17] where the detection of fatigue cracks becomes nearly impossible. Thus, the time of flight diffraction method can be very accurate for the measurement of open cracks or machined slits, but reaches its limitation in the detection of tightly closed cracks.

The accuracy of detection of fatigue cracks can be improved by using shear waves instead of compression waves. The signals received when using compression waves incident on fatigue cracks can be difficult to detect, while it is possible to receive high amplitude signals for a similar closed crack when using shear waves [17].

Whapham [41] investigated the relationship between the amplitude of signal diffracted by a fatigue crack and the applied static load using both shear and compression waves. It was found that although the signal amplitude decreased, the fatigue crack tip could still be detected using either wave type. However, when the specimens were subjected to a compressive stress, the crack tip appeared to be located several tenths of a millimeter away from its location. This error was deemed to be negligible.

In his experiments, Temple [38] found that surface interaction in fatigue cracks in steel did not completely disappear until a tensile stress of 88 MPa was applied to the crack. Using TOFD with 10 MHz compression wave transducers, it was found that the maximum decrease in signal was 13 dB for fatigue cracks under a compressive stress up

to 70% of the loading used in the growth of the crack, or up to 2/3 of the material yield strength. The signal may decrease further near welded joints where the material is locally yielded from the welding process, or if a substance other than air fills the void. Temple used stresses in his experiments that were higher than would normally be seen in practice, and did not believe it likely that an ultrasonic signal would decrease by more than 8 dB in the field.

2.2.8.3 Time of Flight Diffraction Testing Trials

Many detection trials have been performed on the capabilities of TOFD in locating and sizing defects. Errors in sizing less than 0.5 mm and as small as 0.1 mm in height have been reported [12,34,35], depending on test conditions.

Often times, for detection trials, researchers will prepare specimens with artificial defects, such as machined slits or drilled holes. In general, these defects model actual defects with sufficient accuracy for research purposes. Machined slits are favored over fatigue cracks because their depth can be measured without breaking open the specimen, as is necessary with fatigue cracks. However, it should be noted that machined slits can be considerably wider than fatigue cracks, thus they do not experience crack closure effects, such as transmission, like those of fatigue cracks. The amplitude of signals received from slits is in general at least 3 dB higher than that from fatigue cracks [12].

During the development of TOFD, Silk [42] performed detection trials using various types of slits. Experiments were performed on specimens containing slits of constant depth, ranging from zero to 40 mm, and on specimens with stepped slits with variable depths between 1 mm and 5 mm. For all experiments, the slits were sized accurately within 0.2 mm to 0.3 mm.

Other researchers have found similar accuracy for the estimation of height of machined slits using TOFD. Date [31] found average error of 0.79 mm with a standard deviation of 0.48 mm for slits ranging in height from 0.82 mm to 9.97 mm. Baby [32,43] obtained sizing estimates within 0.1 mm in depth and 0.36 mm in length of slit for slits ranging in

height from 0.91 mm to 19.98 mm. These three researchers performed TOFD from the surface containing the slit.

Zippel [37] investigated the possible use of TOFD for the detection of fatigue cracks in bridges. Saw-cut notches were introduced into the steel specimens. The probes used for the TOFD testing were two 5 MHz compression wave transducers both mounted in a 60° wedge. Two plates were prepared, each with 3 notches. The depth of notches in the plates varied from 3.18 mm to 12.7 mm, with a width of 0.6 mm. The location of the notches was found to within 5% of specified values using TOFD, which equates to 0.64 mm for the deepest slits. When scans were performed on the underside of the specimens, that is the surface not containing the crack, crack depth, often overestimated, was found with errors within 5%. This is a similar result to Silk [42], Baby [32,43], and Date [31]. However, when the scans were performed on the surface containing the crack, as done by the other three researchers, the depth estimates were much less accurate, with errors up to 50% for shallow cracks.

The effect of angle on the detection of slits using TOFD was also studied by Baby [32,43] and Date [31]. Date prepared test specimens with machined slits of varying depths, ranging from less than 1 mm to 15 mm. Slits were introduced at two angles, either normal to the surface or at a 30° angle, to investigate the detection capabilities for inclined cracks. Date found that TOFD was quite accurate in sizing cracks, with little difference between the normal and inclined cracks. Baby found that it was possible to resolve the angular disposition of machined slits ranging in height from 5 mm to 19.82 mm with an error of less than 3°.

Yokono [44] performed a study on the capability of detecting subsurface defects using TOFD. Each 14 mm thick steel specimen used in this experiment contained a machined slit of height ranging from 1 mm to 3 mm at a depth of 0.5 mm to 2 mm from the surface. Two methods of detection were used, both a single transducer configuration, and dual transducer configuration. Both methods overestimated the depth of the cracks, however, the dual probe method was more accurate in sizing defects than the single probe, with errors less of than 1 mm in slit height.

Several researchers investigated the use of TOFD to size fatigue cracks in addition to machined slits, as fatigue cracks are the type of defect found in the field. Lidington and Silk [45] furthered their earlier work [42] on the accuracy of TOFD by investigating implanted fatigue cracks in steel specimens. Depths of crack ranged from approximately 7 mm to 15 mm. The depths of crack were measured at various points along the crack length, with the TOFD probes being placed on the surface containing the crack. Overall, the mean error in depth estimates for each specimen was 0.41 mm or less. It was found that the error in depth measurement increased as the depth of the crack changed suddenly along the crack length. Average error decreased for cracks with more regular profiles.

Zippel [37] introduced a fatigue crack into four plates and one full-scale plate girder. The depth of the fatigue cracks ranged from 0.79 mm to 3.0 mm. Scans performed on the underside of the plates yielded depth estimates with average error of 5%. Scans performed on the surface containing the cracks, however, yielded poor estimates for the crack depth. The crack depths were greatly overestimated, up to 8.35 times in some cases. TOFD was performed at six times during fatigue testing of the plate girder. Values of the depths during various testing times were found by inspecting the specimen after failure. TOFD estimates of crack depth were found to be within 7% of the visually determined depth of the crack.

Bloodworth [46] investigated the possible use of TOFD to size defects in the nozzle attachment welds in a boiling water reactor. This application posed several challenges for the TOFD method. The specimen was composed of ferritic steel with an austenitic stainless steel cladding on the inner surface. Also, the geometry of the nozzle was complex; thus, the TOFD transducers were not able to lie on the same flat surface. Despite these difficulties, TOFD was able to size the defects, including fatigue cracks, lack-of-fusion defects, and slag inclusions, within the allowable tolerance of 2.3 mm. This error was up to 5 times as large as error found by other researchers. The specimens used by Lidington and Silk [45] and Zippel [37] were flat plates which posed little difficulty for the TOFD method as the transducers were able to lay on the same flat surface. The increase in error found by Bloodworth was likely due to the complex geometry of the specimens used.

Golan [17] used TOFD to determine the depth of fatigue cracks in 46.8 mm thick steel plates. TOFD was performed while the specimens were subjected to fatigue loading, unlike other researchers who performed TOFD on specimens which were not subjected to loading during testing. By performing TOFD during loading, the accuracy of size estimation would be less affected by crack closure. Golan found that the diffracted signal from the crack tip fluctuated less during cycling than the reflected signal, thus TOFD measurements are a better estimate of fatigue crack depth than other ultrasonic methods, such as pulse echo, which use reflected signals. Error in estimation of crack depth ranged from 0.1 mm to 1.7 mm for the crack ranging in height from 6 mm to 9 mm, similar to estimates made on fatigue cracks not subject to loading during testing.

Most researchers find that the accuracy of TOFD increases as the distance between the crack tip and the scanning surface increases. Many found it difficult to size shallow cracks from either surface of the specimen as dead zones exist near the lateral wave and back wall echo which can mask the signal from a crack. Zippel [37] found it possible to detect all defects with depth greater than 0.8 mm, otherwise the crack signal could not be distinguished from the back wall echo. Yokono [44] found the dead zone of the probe to extend only 0.5 mm when placed on the cracked surface, with all defects deeper than this reliably detected. Baby [32,43], however, was not able to achieve these results. Baby found it difficult to accurately size cracks less than 2 mm in depth when scanning from the surface containing the slit due to interference from the lateral wave.

Baskaran [16] studied the use of TOFD on thin steel sections, that is those with thickness between 6 mm and 10 mm. It is more difficult to detect and size defects in thin sections as the accuracy of TOFD decreases as crack tips become closer to the test surface. Two types of test samples were prepared. The first type of sample was made from 10 mm thick aluminum plates with simulated defects, including slits and side-drilled holes. The second type of test sample was 7 mm thick steel plate with fatigue cracks grown at a weld toe. Baskaran found it difficult to size cracks in these thin specimens using standard manual TOFD sizing methods. As the thickness of the specimen decreased, the signals of interest, that is the lateral wave, back wall echo, and any indication of a defect, arrived closer together and appeared to be superimposed, making it difficult to distinguish

between the various signals. It was suggested that a higher frequency, above 5 MHz, be used for testing thin sections to increase resolution. Baskaran also described the use of an alternate technique to analyze TOFD data, the embedded signal identification technique (ESIT). When multiple signals are superimposed, the shape of the A-scan is altered. ESIT works to identify and separate superimposed signals at a location of interest to better determine the time of flight of a signal from a defect. ESIT can also be used to automatically size defects.

The average error in depth estimation for the machined flaws using 10 MHz probes was 7% of the depth of the defect. This error reduced to below 3% for the automated ESIT technique. Average error in estimates increased considerably, to over 20%, when 5 MHz probes were used. ESIT was also found to be superior to manual sizing of defects for the specimens containing fatigue cracks.

2.2.8.4 Time of Flight Diffraction Operator Error

In order for TOFD to accurately size defects, these defects must first be detected. Verkooijen [47] reports a probability of detection rate for TOFD of 82.4% with a false call rate of 11.1% found during a project conducted for the Dutch Welding Institute. This probability of detection is higher than for many other non-destructive testing methods, including X-ray and manual ultrasonic methods.

Silk [48] recognized that the probability of detection and false call rates are dependent on both the detection method and the operator. Thus, using artificially created B-scans, Silk investigated the probability of detection and the probability of false indications based on human performance and error. Fifty realistic B-scans were created containing a randomly chosen type, size, and location of a single defect with varying levels of noise. The defects were made to represent both surface breaking cracks and slag lines of depth between 1 mm and 7 mm from the back surface of a 5 mm thick specimen. These B-scans were analyzed by five operators, working independently, who were all experienced in visual analysis of TOFD data. The operators were given no knowledge of the defect characteristics before the study, they were only told that each scan contained 3 defects or

less. Each operator recorded the location of any signal they determined to be a flaw. They then attempted to size the supposed flaw.

For the moderate noise levels, expected in the field, the probability of detection was 100%. As expected, the probability of detection tended to fall as noise levels increased. Detection fell to as low as 40% for very high noise levels, that is where the noise level reached 80% of the amplitude expected from the defect. The probability of false indication rose with increasing noise level, from 3% percent at moderate noise levels that would be encountered in the field to 11% at very high noise levels. The probability of detection was similar for all operators involved, however they differed in their false call rates.

Defects were sized with an average error of 0.23 mm in depth and from 5 mm to 10 mm in length. Errors in sizing were consistent no matter what the noise level in the scan.

Silk [49] furthered this research by creating an additional set of 26 artificial B-scans. These scans were used to determine the capability of TOFD in estimating the profile of a defect. Two types of defects were used: a straight profile and a curved profile open to the back wall surface. The artificial test specimen was 50 mm thick containing one defect in a known location. Again, five operators independently analyzed each B-scan. Each operator used five different sizing methods for each scan. Average error in depth estimation was 0.12 mm. Estimation of length of flaw differed greatly by method from 3.4 mm to 12.1 mm, depending on the type of defect, as some methods were more useful for straight profiles than curved profiles, and vice versa. When multiple sizing procedures were used in combination to exploit the strengths of each method, errors in length estimation decreased to an average of 3.7 mm or 4.4 mm, depending on the combination. There was little difference found between the average errors in measurements between operators. Thus, when operators receive proper training, there should be little error introduced into measurements due to human performance.

2.3 Eddy Current Testing

Eddy current testing (ET), an electromagnetic testing method, was first used for non-destructive testing by D.E. Hughes in 1879 to conduct metallurgical sorting tests [8]. It was not until the 1940's, however, that eddy current became widely used for NDT due to the efforts of Friedrich Forster [50]. Today, eddy current testing is used for many applications including finding defects in test specimens, detection of conductivity variations in materials, determining the thickness of conductive materials or the thickness of a non-conductive material, plating, or cladding overlaying test specimens, and finding the spacing between conductive layers [8]. In order to use eddy current testing successfully, only one or possibly two of the above variables can be allowed to vary, otherwise it is difficult to determine the cause of a fluctuating eddy current signal [9].

2.3.1 Eddy Currents

Eddy currents are closed loops of current flowing in a large conductor. They are similar in shape to the swirling eddies found when fluid flows around an obstacle. Eddy currents are created when a conductor is subjected to a fluctuating magnetic flux. The fluctuating magnetic flux will create a voltage in the conductor, causing current to flow, in a process called inductance.

2.3.2 Mutual Inductance

Eddy current testing works on the basis of mutual inductance, which states that a fluctuating current in a primary circuit will induce a voltage in an adjacent, secondary circuit. This induced voltage will cause an induced current to flow in the secondary circuit. The principle of mutual inductance is illustrated below in Figure 2.16 where an alternating current generator produces a current in the primary circuit, which in turn creates an induced current in the secondary circuit. As applied to eddy current, the primary circuit, provided by the test probe, will induce a current in the test specimen (the secondary circuit).

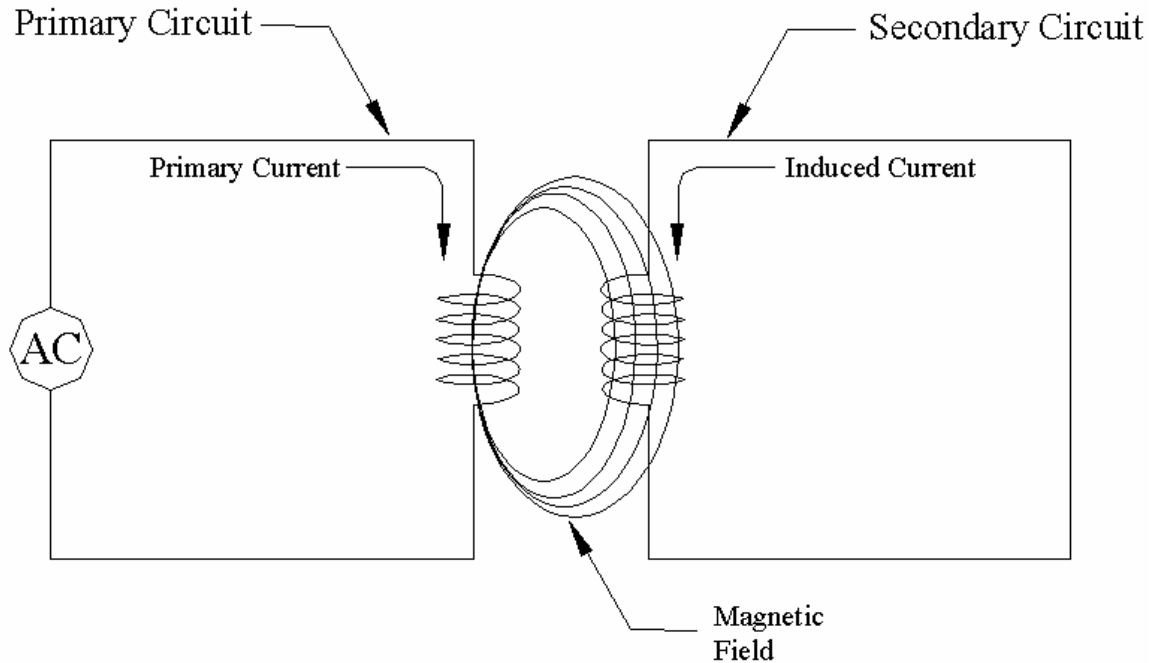


Figure 2.16: Mutual inductance in circuit

In ET, an alternating voltage is placed across the probe which will produce an alternating current in the probe. This alternating current will produce an associated magnetic field, which is concentrated around the coil, with flux lines being perpendicular to current flow. The primary magnetic field will induce a back voltage in the coil providing added resistance to current flow in the coil called inductive reactance. Then, the probe is placed near the test specimen. The primary magnetic field will induce a voltage in the test specimen which will cause eddy currents to flow perpendicular to the flux, thus parallel to the primary current, but in the opposite direction. The eddy currents produce an associated secondary magnetic field, which is in opposition to the primary magnetic field. The secondary magnetic field will decrease the inductive reactance of the coil. This process is shown in Figure 2.17.

Any changes in the eddy currents due to defects or changing material properties will disturb the secondary magnetic field, and hence its effect on the primary magnetic field and the inductive reactance in the coil. By monitoring the impedance of the coil, or the coils total opposition to current flow as defined by:

$$Z = \sqrt{R^2 + X_L^2} \quad (2-10)$$

where Z is the amplitude of the impedance, R is the resistance of the coil, and X_L is the inductive reactance of the coil, indications of defects in the test specimen can be found [8].

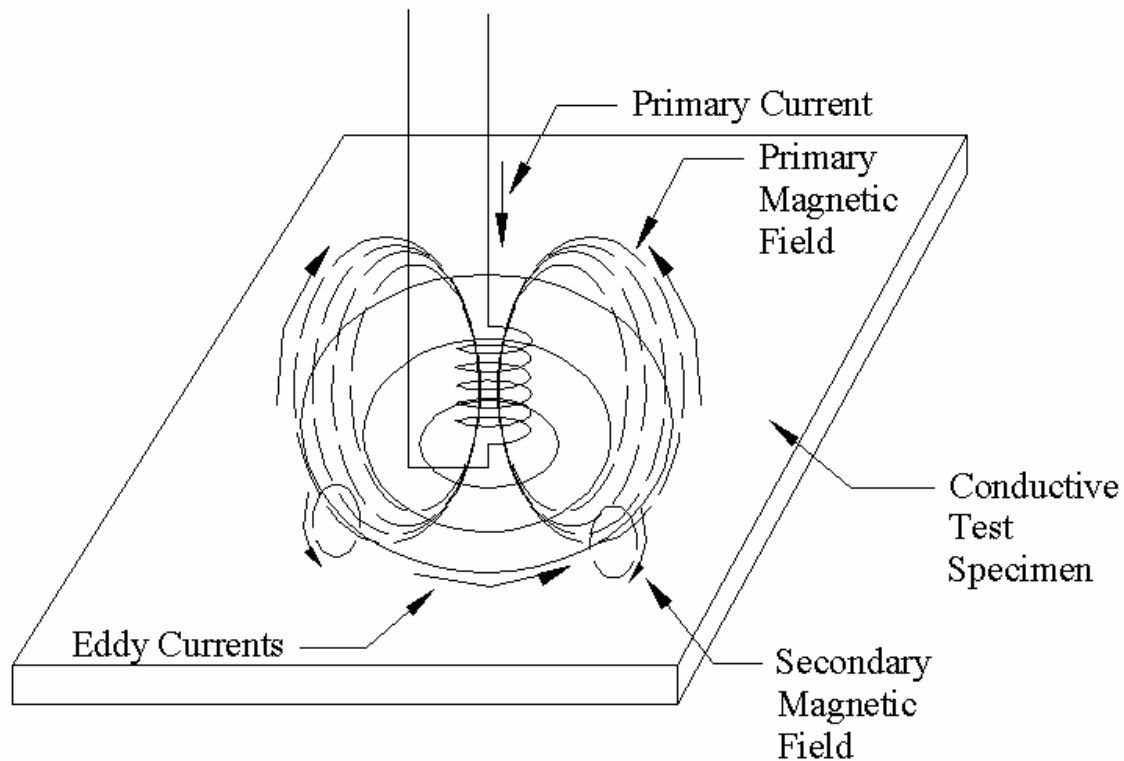


Figure 2.17: Mutual inductance for eddy current testing

2.3.3 Eddy Current Behavior (Defect Detection)

In order for ET to be used on a specimen, the material must have sufficient conductivity for eddy currents to flow. Conductivity is the ability of electrons to flow in a material. Materials with higher conductivity have a higher current flow at a given voltage than materials with a lower conductivity. Thus, the flow of eddy currents is proportional to the conductivity of the test specimen. Conductivity, and its inverse, resistivity, are affected by defects, vacancies, plastic and elastic deformation, and corrosion [9]. In a material free of defects or material property changes, eddy currents will flow in closed, concentric circular loops as seen in Figure 2.18 (a). When an eddy current encounters a change in conductivity, for example if a defect intersects its path, the eddy current will be forced to flow around the defect. In general, eddy currents will take the path of least resistance, flowing around short, deep cracks or under long, shallow cracks [8]. When

the eddy currents flowing in the test specimen are forced to alter their path due to a defect, the secondary magnetic field will change, causing the impedance of the coil to change, and indicating to the operator that a defect is present. The eddy currents must be sufficiently disturbed by the defect in order for the change in impedance of the coil to be significant enough to be detected.

The orientation of the defect with respect to the path of the eddy currents plays a large role in whether or not the defect will be detected. If the eddy currents encounter a defect perpendicular to their path, the current will be greatly disturbed, and the defect is likely to be detected, as seen in Figure 2.18 (b). However, if the defect is oriented parallel to the eddy currents, it will not greatly disturb the path of the eddy current and it is likely to go undetected as seen in Figure 2.18 (c).

2.3.4 Current Density and Depth of Eddy Current Penetration

Should a given defect be oriented favorably to the eddy currents, there must also exist sufficient current density at the depth of the defect to adequately affect the impedance of the coil for detection. Current density is at a maximum on the surface of the test specimen and decreases exponentially with depth based on a factor called the standard depth of penetration, δ .

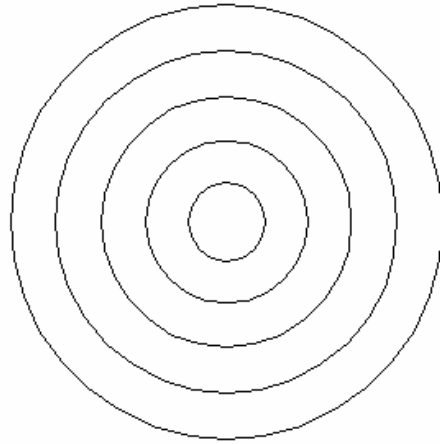
The standard depth of penetration for a material is given by:

$$\delta = 25 * \sqrt{\frac{\rho}{f * \mu_r}} \quad (2-11)$$

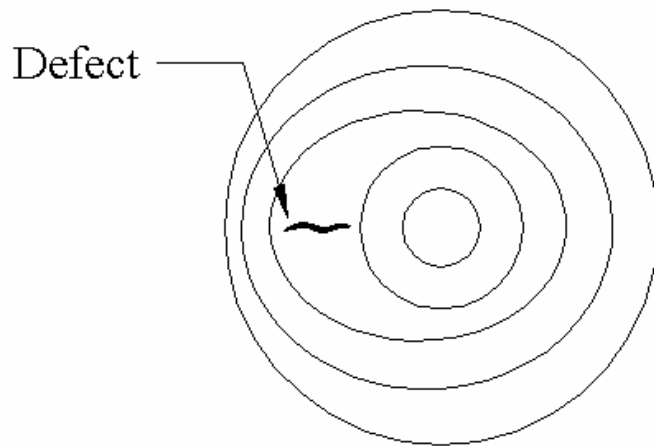
where ρ is the resistivity of the material, f is the frequency of current, and μ_r is the relative permeability of the material. The current density at any depth can then be found as:

$$\text{current density} = \frac{1}{e^\delta} \quad (2-12)$$

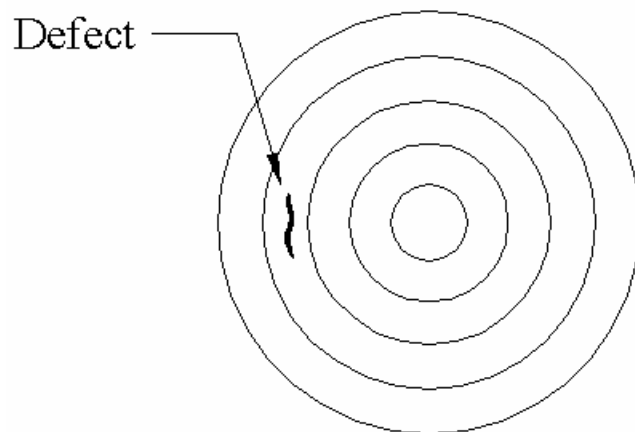
Thus, at one standard depth of penetration, the current density is approximately 36.8%. The current density decreases to 5% at three standard depths of penetration, also called



(a) Eddy currents in material free from defects



(b) Eddy currents flowing around defect oriented perpendicular to current



(c) Eddy currents in material with defect oriented parallel to current

Figure 2.18: Pattern of eddy currents flowing in test material

the effective depth of penetration, as 5% current density is the least amount needed at the defect depth for detection to be possible. The effective depth of penetration is also approximately limited to the diameter of the coil. Below the effective depth of penetration, the current density is too small to be of use for detection purposes [8].

The standard depth of penetration will decrease with decreasing resistivity, or an increase in conductivity. A material with high conductivity yields a high sensitivity to surface defects, but there is a low penetration of eddy currents in the test specimen. A rise in permeability, the ability of the material to become magnetized, will also decrease the standard depth of penetration of eddy currents. Permeability produces noise in the eddy current output signal which increases with depth, thus eddy current testing is only reliable at shallow depths for materials with high permeability. Permeability can be made constant through saturation, as for ferromagnetic materials discussed below in section 2.3.8 [8]. Decreasing the frequency of the primary current can increase the depth of penetration. However, this decreases resolution, as the smallest dimension of a defect that can be detected is inversely proportional to the frequency of the primary current.

2.3.5 Eddy Current Equipment

The equipment necessary to perform eddy current testing includes an alternating current generator with a measuring circuit, which can sense changes in the magnitude or phase of the coil current or voltage, an amplifier, an output indicator and recorder, and the test probe [9].

2.3.5.1 Probe/Coil

A eddy current testing probe consists of a length of copper or other non-ferrous metal wire wrapped in a coil around a cylindrical tube, called a former. By coiling the wire, the magnetic field produced by the current in the coil is concentrated, making the flux large enough to produce eddy currents of sufficient magnitude to cause measurable changes in impedance of the primary circuit [9]. The wire is generally wound in more than one layer, which will increase the inductance of the coil. Thus, the coil will be able to induce larger eddy currents in the test material with the same amount of coil current versus a coil

made with a single layer of wire. A rise in inductance will also produce an increase in sensitivity to small defects [50]. The inductance of the coil, L , can be approximated as:

$$L = \frac{\mu n^2 A}{l} \quad (2-13)$$

where μ is the magnetic permeability of core, n is the number of turns in the coil, A is the cross-sectional area of the coil, and l is the length of the coil.

The former prevents the coil from deforming during use. Generally, the former is made of a dielectric material. These coils are called “air” cores, as the permeability of a dielectric material is approximately equal to that of air. Other core materials can be used, such as ferrites, which have permeability greater than air. Ferrite cores can raise the inductance of a coil by five or ten times versus an air core. These cores are useful for testing materials which do not have variable permeability. If a ferrite cored probe is used on a material with a variable permeability, the secondary magnetic field due to the eddy currents could be significant enough to induce eddy currents in the ferrite core, thus the impedance of the coil would no longer be constant and the test output would be difficult to interpret. Coils with ferrite cores are useful for detecting defects in steel that may be otherwise difficult to detect, as the increased inductance of the coil is able to produce larger eddy currents in the test material which are more likely to reach buried cracks [50]. The resolution, or ability to detect and separate discrete flaws, of eddy current testing is increased with the use of ferrite cores. The smallest flaw detectable is approximately equal to the diameter of the coil. However, a ferrite core concentrates the magnetic flux resulting from the primary current, and reduces the effective diameter of the coil [9].

2.3.5.2 Frequency

The range of frequency of the primary coil current can range from a minimum of 50 Hz to a maximum of 10 MHz for different eddy current applications [8]. It is best to keep the coil current frequency as low as possible while retaining sufficient frequency to achieve the desired level of resolution. Lower coil currents prevent a rise in the

temperature of the coil, which can lead to expansion of the wire and a rise in inductance of the coil, producing adverse noise in the output signal [50].

2.3.5.3 Impedance Measurements/ Bridge Circuit

In order to measure variations in impedance or voltage across the coil during testing, a bridge circuit is used. It is common to use Maxwell's inductance bridge for eddy current testing instruments [50].

Bridge circuits generally have a high sensitivity to changes in impedance [50]. Before testing of the specimen begins, the bridge is first balanced with the probe over an area of the material with no defects in order to get a reference signal. Then, during testing, any measured bridge imbalance can be attributed to a defect in the specimen or a changing material property [8].

2.3.6 Lift-off and Probe Wobble

During eddy current testing, it is important to keep lift-off, or distance between the coil and the test specimen, as constant and as small as possible. Increased lift-off decreases the eddy currents induced in the test specimen, and therefore also decreases the amplitude of any change in coil current due to a defect. In order to detect a defect while using a large lift-off, the output signal can be amplified [9]. Also, the orientation of the probe relative to test specimen should be kept as constant as possible. By changing the orientation of the probe, known as wobble, the operator can introduce unnecessary noise into the signal which can make defect detection more difficult [8].

2.3.7 Output

The output signal from eddy current testing, or the impedance of the coil, is plotted in the impedance plane. The impedance plane is a plot of inductive reactance versus resistance of the test coil. When the coil is over a defect-free section of test material, the impedance of the coil will be constant and will be plotted on the impedance plane at the so-called air point. As the probe travels over a defect, or other area with a changing material property, the point on the impedance plane will move to the new impedance of the coil through a

unique path. The path that the point takes will be characteristic of the type of defect or changing material property encountered [8].

Any indication of a defect will be largely qualitative, however several characteristics may be determined from the output data. The approximate depth of the defect can be determined, as the phase lag of the signal will increase with the depth of the defect at one radian per standard depth of penetration [8]. The maximum impedance of the coil is only related to the depth of the defect below the surface, it is independent of the width of the crack.

2.3.8 Simple Calibration of Instruments

A simple calibration of the testing instruments can be done by using a test block of the same material as the test specimen with saw cuts of various lengths made on the block surface. The probe is positioned over a defect-free portion of the test block and the bridge is balanced. Then, the probe is positioned over each of the saw cuts and the amplitude of the potential difference and phase angle of the output is recorded. This data is used to create a calibration curve for the size of the defect versus output signal for a given frequency of primary current and input voltage. More complex methods of calibration can also be carried out [50].

2.3.9 Testing of Ferromagnetic Materials

Ferromagnetic materials, such as steel, need special treatment during eddy current testing in order for testing to be successful. The concept of ferromagnetism is based on the Bohr-Sommerfeld atomic model which states that electrons orbit around the positively charged nucleus in certain circular or elliptical orbits. Each orbiting electron spinning on its axis forms a magnet with the sign of the magnetic field dependent on the direction of the spin. In most materials, there are an equal number of electrons spinning in each direction which cancel each other out, thus the material is not magnetic. In ferromagnetic materials, however, there exist unpaired electrons which line up parallel to each other on the atomic level in regions called domains. These domains are generally randomly oriented, thus there will be no net magnetic field and the material will not be magnetic.

The presence of an external magnetic field will cause these domains to line up parallel to each other and the material will become magnetized [9].

Ferromagnetic materials have a high and often non-constant permeability, or ability to be magnetized. This variable permeability allows for little penetration by eddy currents into the material and introduces excess noise into the signal which can mask defects while testing. In order to successfully test ferromagnetic materials using eddy current, the material must first be saturated, where any increase in magnetizing force produces negligible increase in the magnetic field produced by the test specimen, or at least a magnetic bias must be applied. Saturation makes the permeability of the material constant which allows for greater penetration of the eddy currents and decreased noise in the signal, while a magnetic bias will only reduce permeability, but not to the point of saturation. In order to apply a magnetic bias to a ferromagnetic material, an additional direct current coil is used [9].

2.3.10 Advantages/Limitations

Eddy current testing has several advantages over the other methods of non-destructive testing. Eddy current is useful for locating surface or near surface defects in conductive materials, with a high sensitivity to small defects. There is no contact required between the probe and the test specimen. Eddy current testing requires no surface preparation of the test specimen or couplant between the probe and specimen [8]. Also, the equipment required for eddy current testing is relatively low cost and can be portable [9].

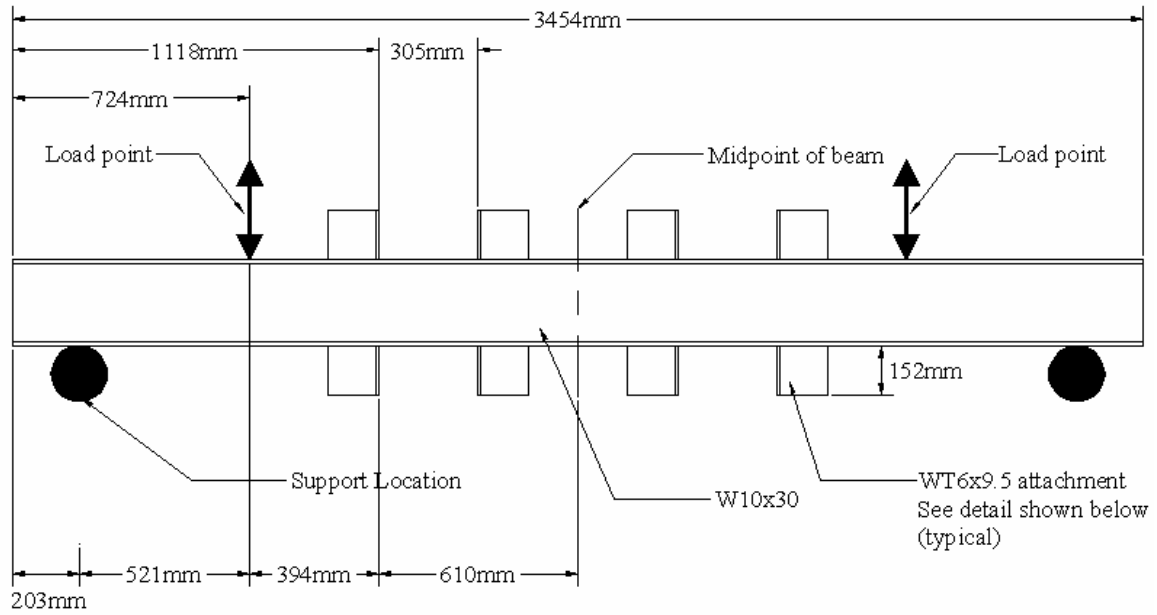
There are several limitations or disadvantages of eddy current testing as well. The test specimen must be conductive, which greatly limits the possible applications of eddy current testing. Any indication of a discontinuity is largely qualitative, and it is difficult to determine the dimensions of the defect [9]. Eddy current testing is only able to detect surface or near surface defects up to a depth generally on the order of a few millimeters, making it impossible to detect deeper buried defects in thicker materials [8]. Also, ferromagnetic materials must be magnetically biased or saturated before testing and then usually demagnetized after testing to prevent debris from being attracted to the specimen, which increases the testing time [9].

3 EXPERIMENTAL PROCEDURE

Testing was performed to determine the feasibility of correlating crack lengths estimated using non-destructive testing to the remaining fatigue life of welded joints. Fatigue tests were conducted on large-scale specimens which realistically modeled details found in ship hulls. Ultrasonic non-destructive testing was performed three times during testing to determine the extent of fatigue cracking. After the final UT investigation, the fatigue testing was continued until failure of several attachments occurred.

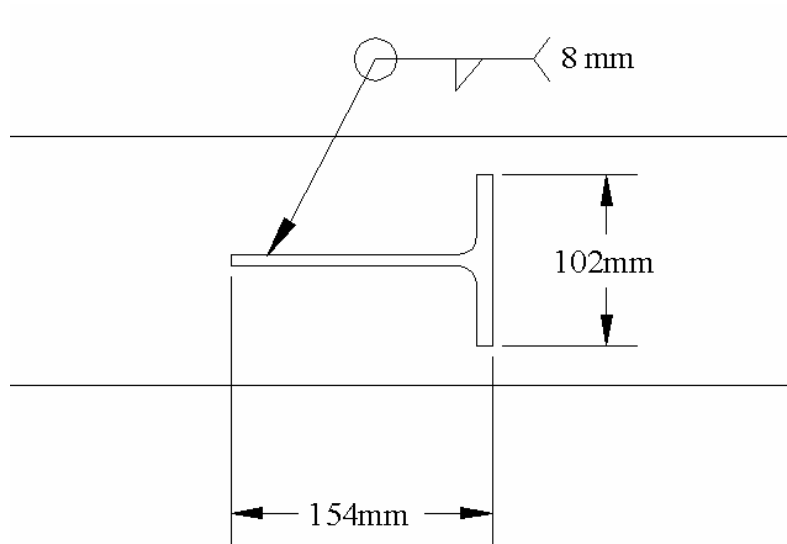
3.1 Test Specimens

Three similar test specimens, Specimens A, B and C, were tested in this project. The specimens were models of a simple girder with eight non-load-bearing attachments. These attachments represented transverse plates with rib attachments as in a typical ship detail. Each specimen was made from a W10 x 30 wide-flange section approximately 3.5 meters long, as shown in Figure 3.1. A photograph of a typical specimen is shown in Figure 3.2. A572 Grade 50 structural steel was used to construct the specimens, as this steel is similar to the steel used in ship structures. The specimens each had eight attachments fillet welded to their flanges, four each on the top and bottom flange, symmetrically placed. The attachments were WT6 x 9.5 rolled tee sections approximately 152 mm in length. The tee sections had a 9 mm thick flange with a 6 mm thick web. The tees were welded to the 13 mm thick flanges of the W 10 x 30 beam using an 8 mm fillet weld, which extended around the entire perimeter of the tee section. The attachments were placed such that the web of the tee aligned with the web of the beam. The clear distance between the tees was 305 mm. This distance was chosen to ensure that there was no interaction between the attachments during testing and that fatigue cracking of one tee would not affect adjacent attachments. The numbering of tee attachments is shown in Figure 3.3. An error was made in the fabrication of Specimen C, with Tee 4 being placed 150 mm closer to the beam center than intended. This error did not affect testing of the specimen.



NOTE: Symmetric about midpoint

(a) Typical specimen, showing load, reaction points and attachment details



(b) Weld detail for WT6 x 9.5tee-section attachment

Figure 3.1: Typical specimen



Figure 3.2: Photograph of typical specimen

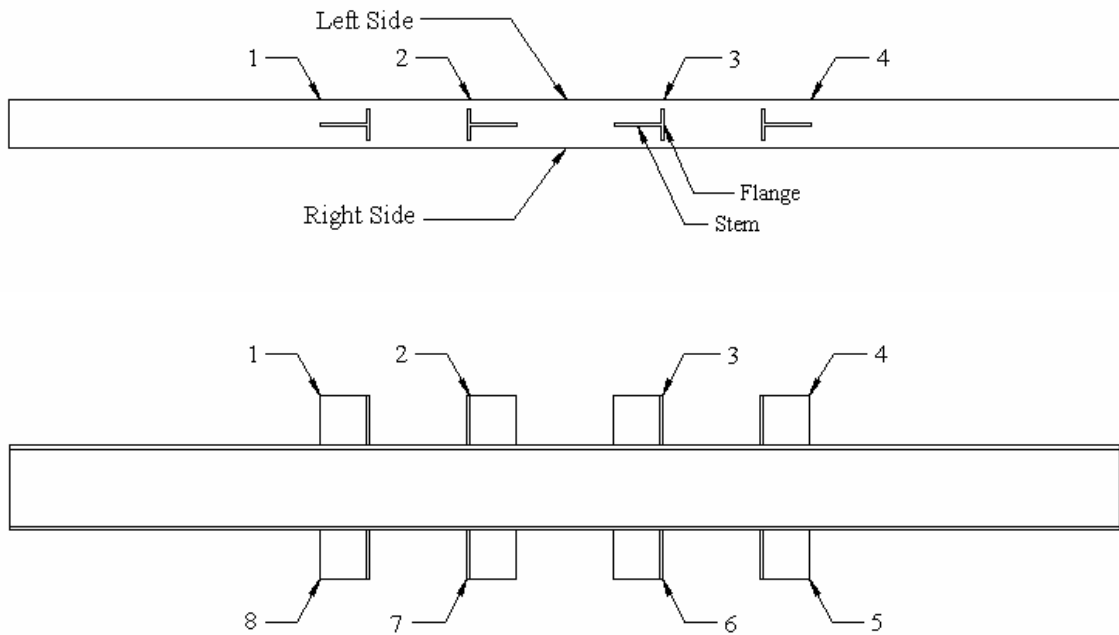


Figure 3.3: Numbering of tee attachments

Specimens A and B were originally used in Project SSC-425 on the Fatigue Strength and Adequacy of Weld Repairs [51]. In the course of this previous project, these two specimens were treated with hammer peening of the weld toes. The weld toes of all of the attachment details of both Specimens A and B were hammer peened with a chisel tool approximately 13 mm wide with a 3 mm radius at the tip. Normal shop air,

approximately 450 KPa, was used to run the peening hammer. The peening hammer was passed over each weld toe four times, determined to be the optimal number of passes in a study by Knight [52]. During the course of Project SSC-425, Specimens A and B underwent fatigue cycles at a stress range of 100 MPa. One of the specimens was subjected to 2,666,079 cycles, while the other specimen underwent only 2,000,000 cycles. At the beginning of the current project, it was not possible to identify which specimen was the one with more fatigue cycles, as no labeling was left on the specimen at the end of the previous project. At the end of Project SSC-425 Specimens A and B had no visible signs of cracking.

The third specimen, Specimen C, was fabricated for the current project from excess materials from Project SSC-425. The weld toes of the attachments on this specimen were not subjected to hammer peening. This specimen was newly fabricated, and thus had not undergone fatigue cycles prior to the start of this project, unlike the other two specimens.

3.2 Test Set Up

Each specimen was loaded in four-point bending as shown in Figure 3.4. A photograph of the load frame with a specimen in place is shown in Figure 3.5. The specimens spanned 3,050 mm between outer supports. The load was applied with a 342 kN hydraulic actuator through a spreader beam to the two load points, located 521 mm inside the outer supports. Rollers were clamped to the beam at the support locations and the load points, as shown in Figure 3.6. These rollers simulated the ideal boundary conditions of a roller. By loading the beam in four-point-bending, all of the eight attachments were in the constant moment region of the beam, subjecting all of the attachments to an equal stress range.

3.3 Static Calibration

The specimens were tested statically to ensure that the proper stress range was being achieved, and that the beam was behaving as predicted by typical strength of material relationships. That is, all of the attachments were being subjected to the same stress range during testing and that the stress was linear through the cross section of the beam

with the neutral axis at mid-depth of the beam. In order to investigate the stress distribution within the beam, strain gauges were placed on Specimens B and C as shown in Figure 3.7. It was assumed that the Young's modulus of the beam was 200 GPa for all calculations. There was good agreement between the predicted and measured stresses in the beam, as can be seen in Tables 3.1 for Specimen B and Table 3.2 for Specimen C. Figures 3.8 and 3.9 show that the stress distribution through the cross section of the beam (gauges 1, 2, 3, and 4) was linear as expected for Specimens B and C, respectively. Figures 3.10 and 3.11 show the stress at the extreme fiber along the length of the beam (gauges 1, 5, 6, and 7) for Specimens B and C, respectively. There was a fairly constant moment region encompassing the tee attachments, consistent with the strength of material predictions.

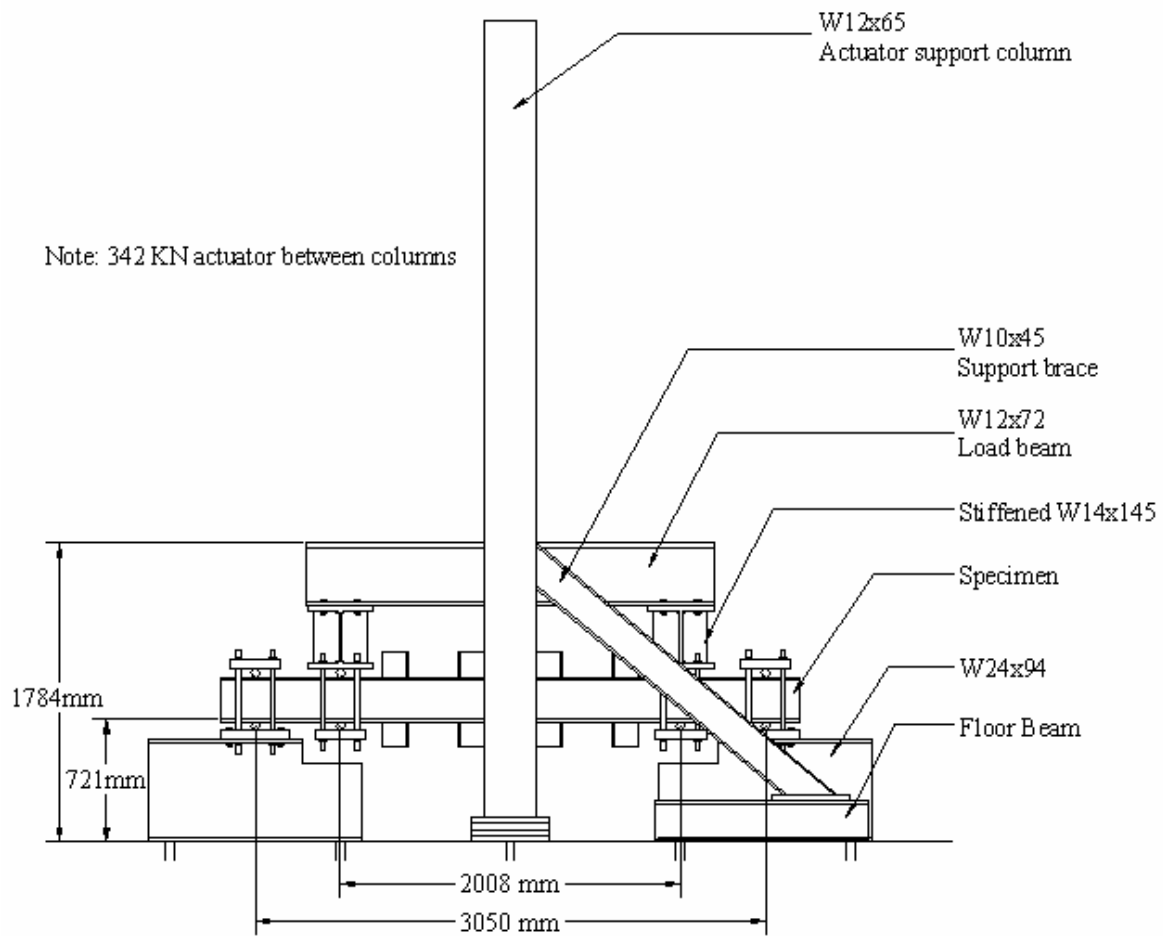


Figure 3.4: Load frame

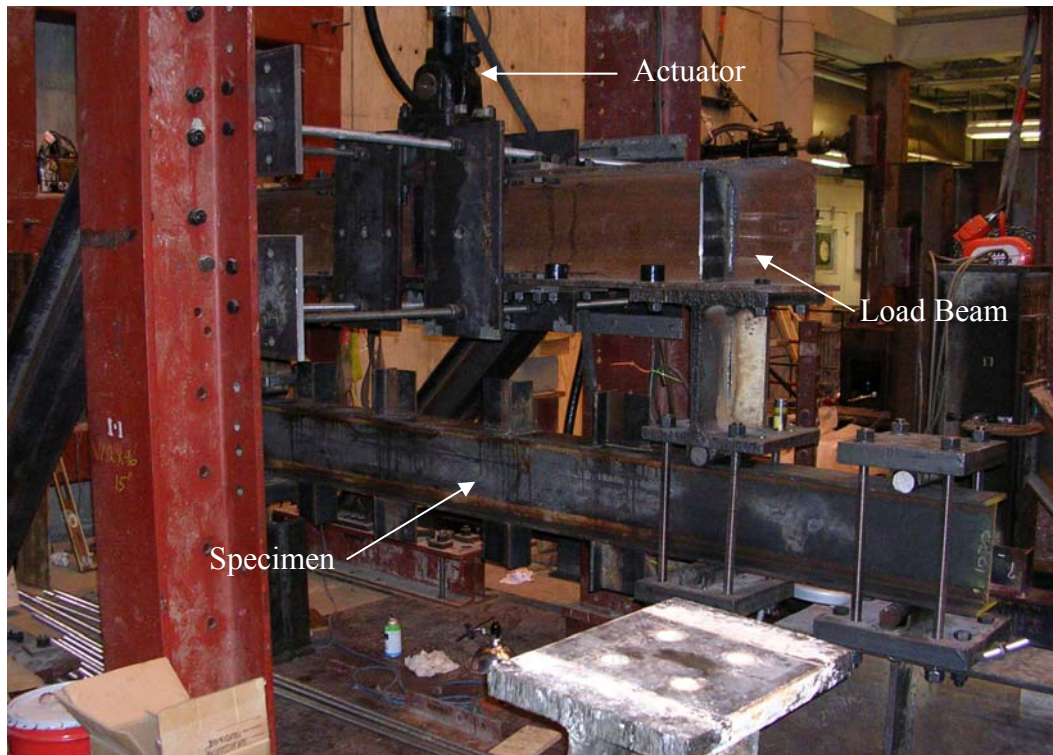


Figure 3.5: Load frame with specimen in place



Figure 3.6: Clamped roller connection

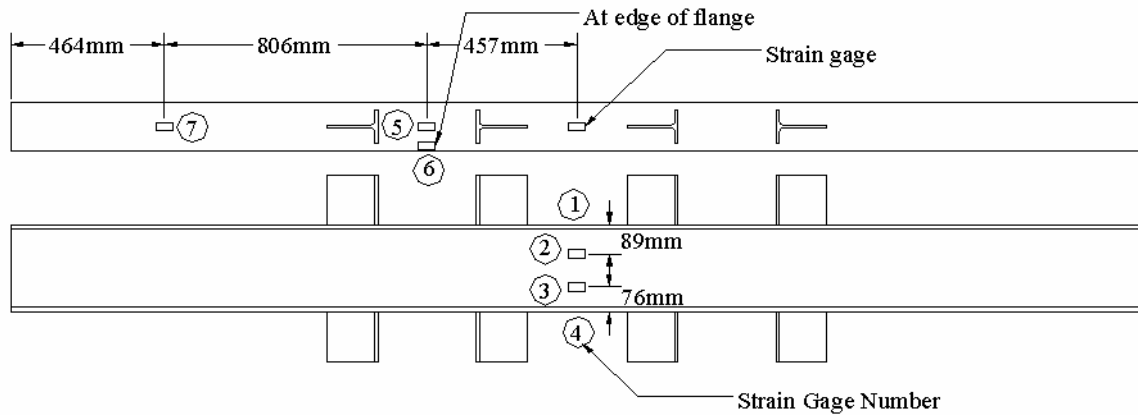


Figure 3.7: Strain gauge layout

Table 3.1: Comparison of predicted versus measured stress in Specimen B at points of maximum loading, with maximum moment of 53.0 kN-m

Location	Actuator in Compression		Actuator in Tension	
	Calculated Stress (MPa)	Measured Stress (MPa)	Calculated Stress (MPa)	Measured Stress (MPa)
Gauge 1	100	98.42	-100	-98.65
Gauge 2	33	31.53	-33	-31.61
Gauge 3	-42.8	-40.96	42.8	41.06
Gauge 4	-100	-98.77	100	99.00
Gauge 5	100	99.12	-100	-99.36
Gauge 6	100	102.23	-100	-102.48
Gauge 7	50	50.41	-50	-50.53

Table 3.2: Comparison of predicted versus measured stress in Specimen C at points of maximum loading, with maximum moment of 26.5 kN-m

Location	Actuator in Compression		Actuator in Tension	
	Calculated Stress (MPa)	Measured Stress (MPa)	Calculated Stress (MPa)	Measured Stress (MPa)
Gauge 1	50	48.88	-50	-48.84
Gauge 2	16.5	15.81	-16.5	-15.79
Gauge 3	-21.4	-20.31	21.4	20.30
Gauge 4	-50	-49.20	50	49.16
Gauge 5	50	50.26	-50	-50.21
Gauge 6	50	50.32	-50	-50.27
Gauge 7	25	26.08	-25	-26.06

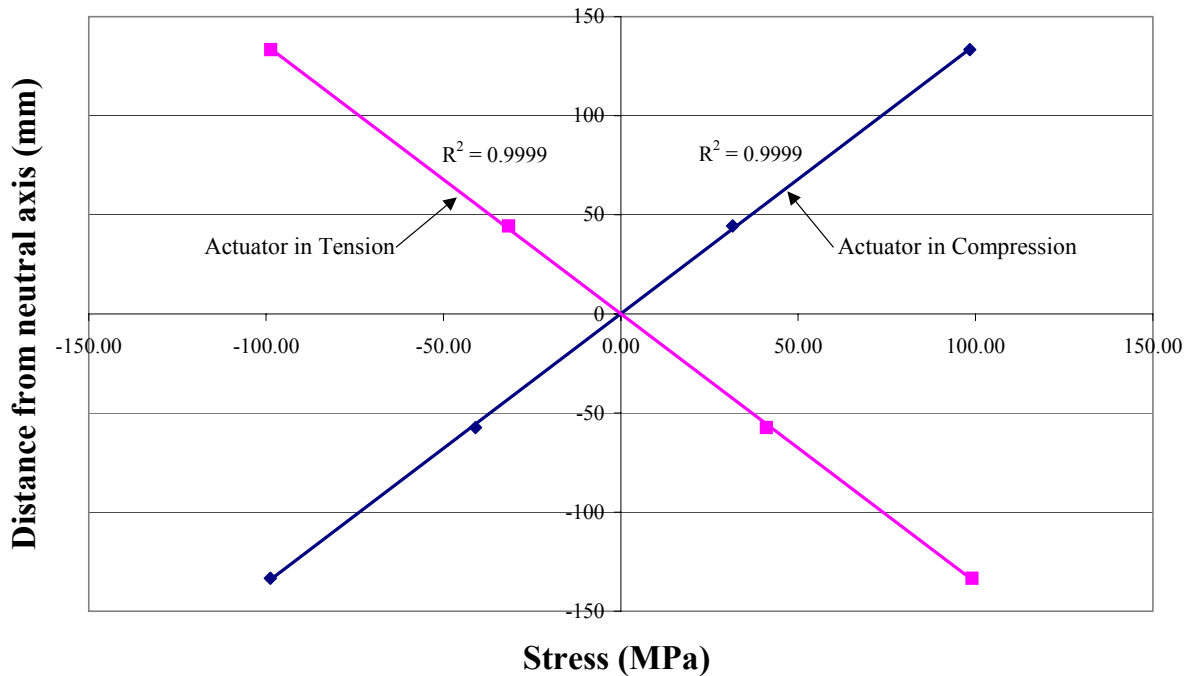


Figure 3.8: Stress distribution through beam cross section for Specimen B, at maximum moment of 53 kN-m

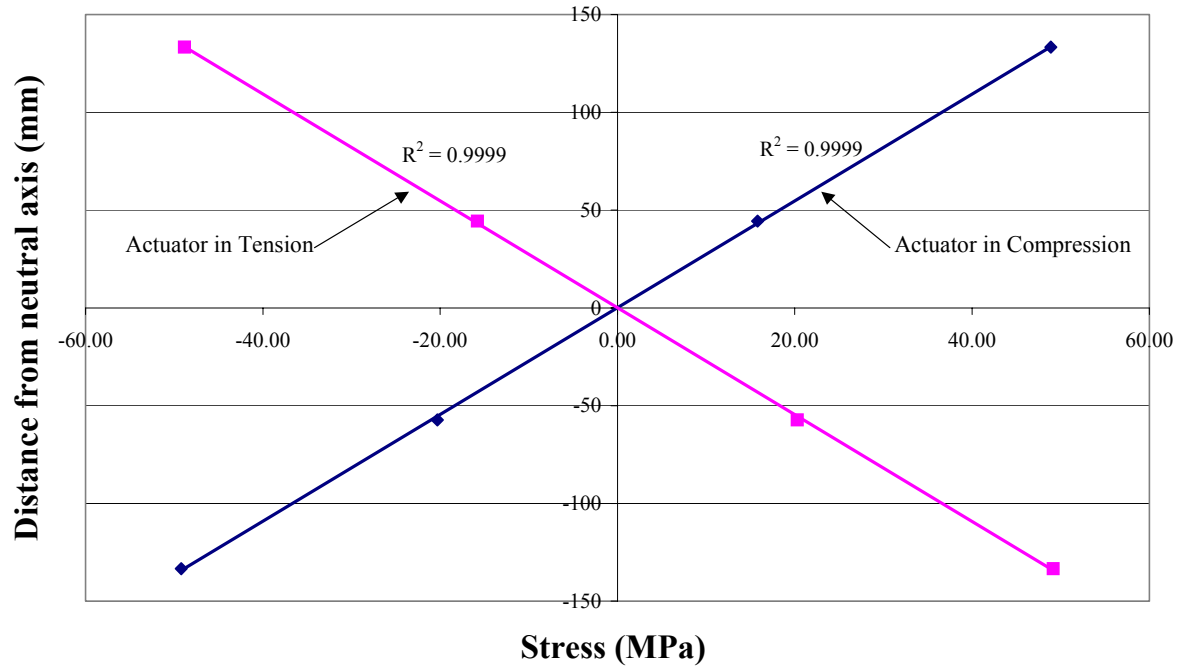


Figure 3.9: Stress distribution through beam cross-section for Specimen C, at maximum moment of 26.5 kN-m

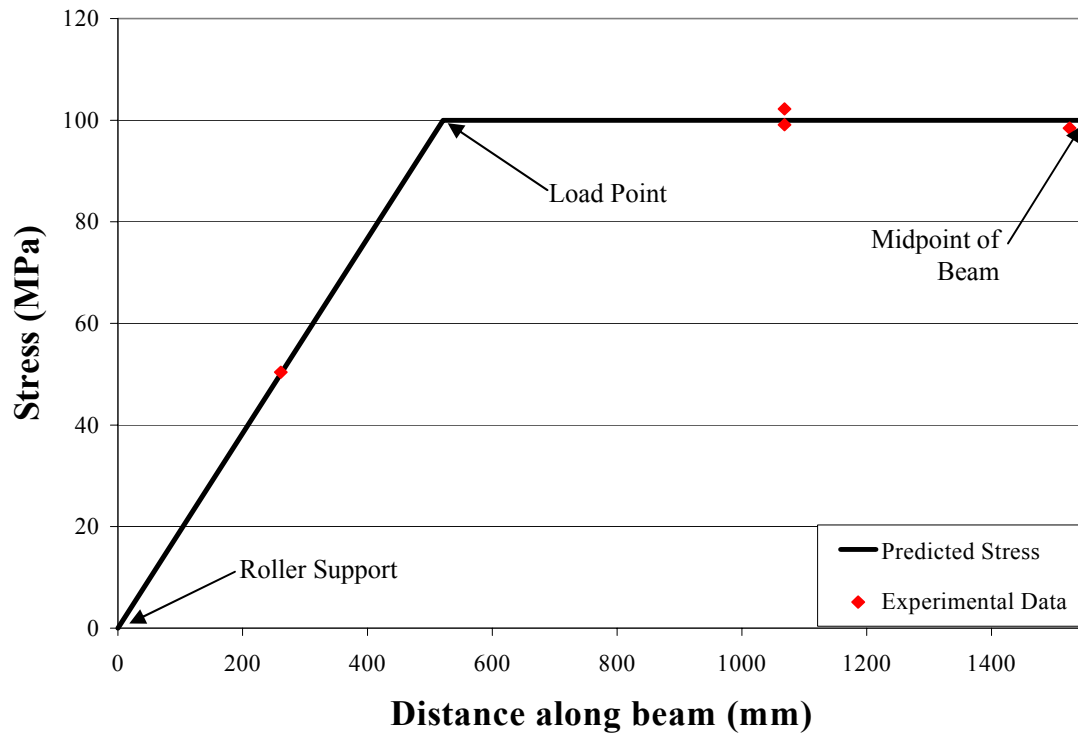


Figure 3.10: Stress along length of beam for Specimen B, at maximum moment of 53 kN-m

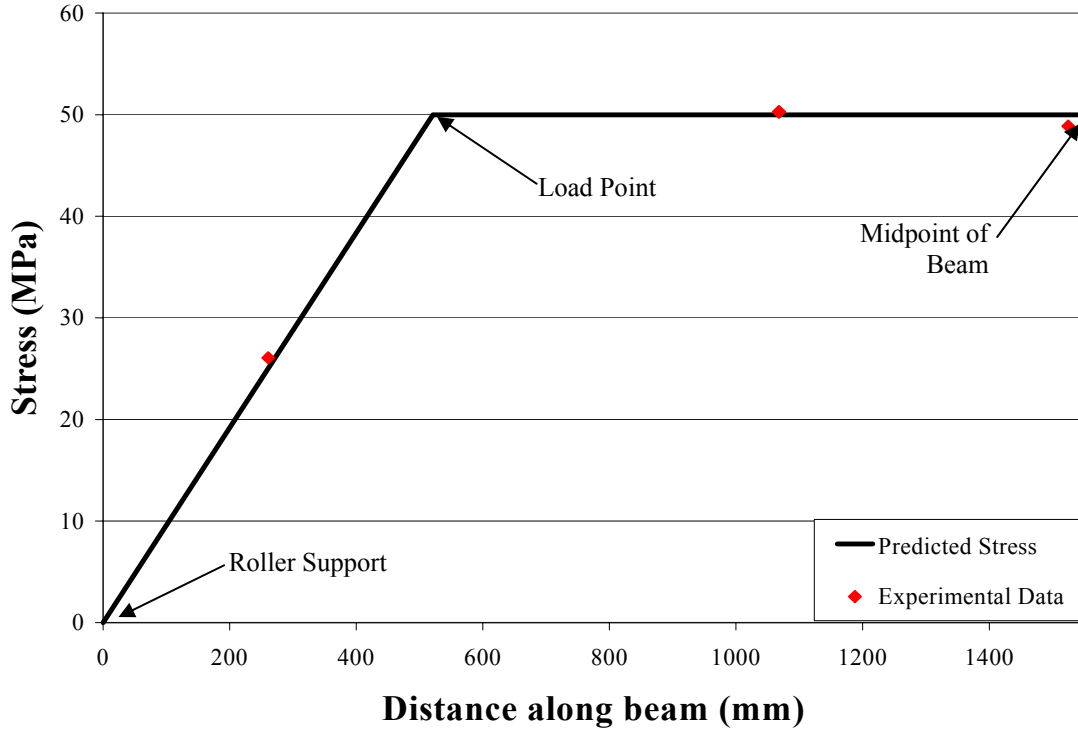


Figure 3.11: Stress along length of beam for Specimen C, at maximum moment of 26.5 kN-m

3.4 Fatigue Test Procedure

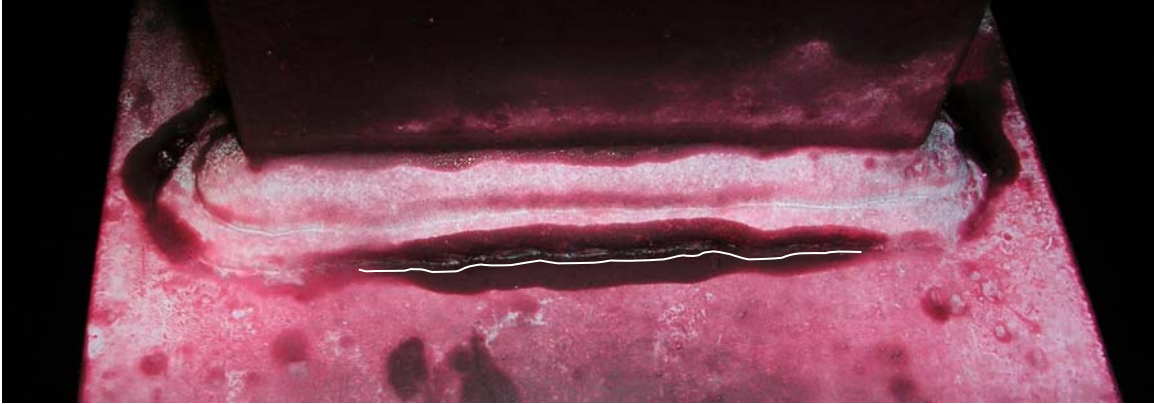
The specimens underwent reversed cyclic loading ($R = -1.0$) to produce fatigue cracking. Specimen C, the newly fabricated specimen, and Specimen A were subjected to a load range of 220 kN (+/- 110 kN) at 1.25 Hz, which produced a maximum nominal stress range of 100 MPa (+/- 50 MPa) at the attachments. Previously, in the course of similar testing for project SSC-425, it was found that at this load range, the expected life of the non-hammer peened specimen was approximately one million cycles. Specimens A and B have already undergone at least two million fatigue cycles at a stress range of 100 MPa, with no visible cracks detected. Thus, the load range for Specimen B was doubled to 440 kN (+/- 220 kN), producing a nominal stress range of 200 MPa at the attachment details, in hopes that failure would be reached. Initially, both Specimens A and B were to be subjected to this higher load range, however after Specimen B suffered a fracture early in the course of fatigue testing for this project, it was decided that the load range applied to Specimen A, and any remaining cycles done on Specimen B, would be reduced to 220 kN.

Throughout fatigue testing, the specimens were closely monitored for visible signs of fatigue cracking and failure. Failure at an attachment was defined as a through-thickness crack of at least 50 mm in length along the weld toe. Cracking was expected to occur at both the stem and the web of the attachment details. Figure 3.12 shows typical cracks at the attachment details. A white curve approximating the crack outline slightly offset from the crack was added to the photographs in Figure 3.12 to aid the reader in identifying the crack locations.

3.5 Weld Repair Procedure

Weld repair was performed on any attachments that reached failure before testing was completed in order to continue fatigue testing and produce failure at additional attachments. Two sided weld repairs were performed at each of the failed sections. The first step of the repair was to drill an 18 mm hole in the web of the beam at the crack tip. This hole was drilled approximately 5 mm past the apparent location of the crack tip to allow for errors in estimation of the crack length and ensure that the tip of the crack was removed. Next, carbon air-arc gouging was used to create an access hole by enlarging the drilled hole. Access holes were oval in shape, approximately 50 mm long and 30 mm wide. All welding was done using the shielded metal arc welding process (SMAW) with E7018 electrodes. The top of the crack was gouged out to form a vee-shaped groove. This groove was then filled with 4 to 6 passes. The bottom of the crack and the root of the weld were then arc gouged to approximately three-quarters of the beam flange thickness to form a vee-shaped groove. Again, this groove was filled with 4 to 6 passes.

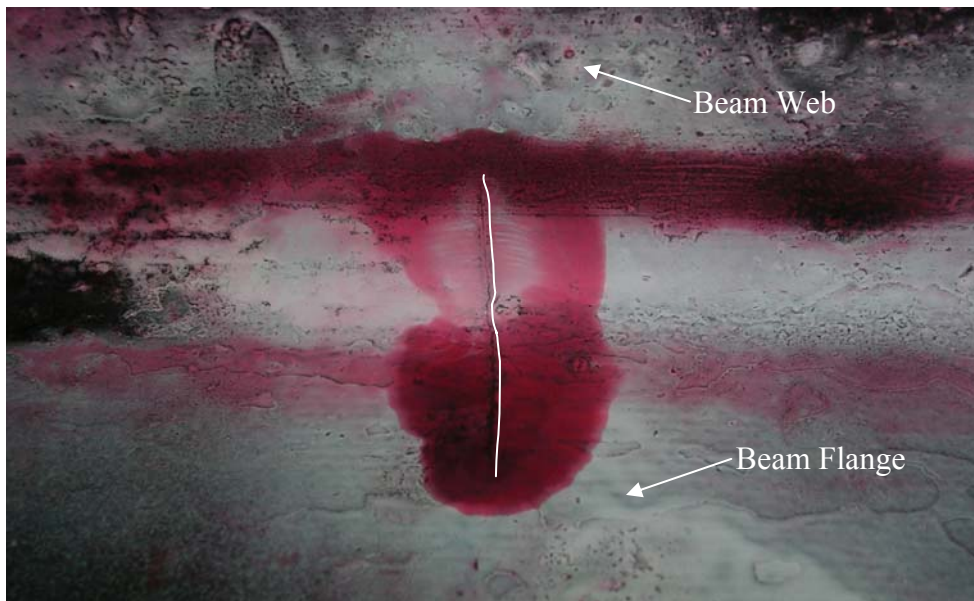
The weld toes of each repair were hammer peened to increase the life of the section. A completed weld repair is shown in Figure 3.13.



(a) Crack at surface of beam flange on Specimen C at flange of Tee 6



(b) Crack at surface of beam flange on Specimen C at stem of Tee 3



(c) Through thickness extent of crack on Specimen C at flange of Tee 4

Figure 3.12: Typical crack at failure of attachment



(a) Repair of attachment side of beam flange, Specimen C at flange of Tee 4



(b) Repair of web side of beam flange, Specimen C at flange of Tee 4

Figure 3.13: Typical repair weld

3.6 Non-Destructive Testing Procedure

Ultrasonic testing was performed three times during the course of this project by an American Society of Nondestructive Testing (ASNT) level III certified operator. The specimens were tested using two UT procedures: time of flight diffraction and linear phased array. During each round of UT, the areas where fatigue cracking was predicted, both the stem and flange of the tees, were inspected. The specimens were tested initially, prior to any cycling associated with the current project, to produce a baseline measurement. At this time, only time of flight diffraction was used. Originally, eddy current testing was to be used as the second method of NDT for this project. After the first NDT, it was found that the capabilities of eddy current testing were limited in this application because the geometry of the attachments and welds led to excessive probe lift off and wobble. Therefore it was not be feasible to use eddy current methods to detect fatigue cracks in the welds. Thus, linear phased array ultrasonic testing replaced eddy current testing and was used for the remaining two inspections. The specimens were tested a second time during the course of the project, after the first crack appeared or after approximately half a million cycles, whichever came first. A final UT was done when either failure of an attachment detail was reached, or the specimen reached 1 million cycles, whichever came first. Table 3.3 shows the number of cycles on each specimen for each round of UT. NDT results are presented in Chapter 4.

Table 3.3: Number of cycles undergone by each specimen at each round of NDT

Specimen	Number of Cycles at First NDT (Baseline)	Number of Cycles at Second NDT (Midlife)	Number of Cycles at Final NDT
A	2,000,000 ^a	709,419 ^b	1,209,419 ^b
B	2,000,000 ^a	386,648 ^b	1,000,000 ^b
C	0	368,395	645,020

a Cycles from previous project SSC-425, one specimen, either A or B underwent 2,666,079 cycles, while the other specimen underwent 2,000,000 cycles

b Number of cycles undergone during current project

3.6.1 Linear Phased Array Procedure

The LPA testing of the specimens was done with a single linear 32-element probe, which acted as both transmitter and receiver. This probe was mounted on a 45-degree wedge. Shear waves were used for the LPA testing. The sound beam was focused at a distance of 13 mm, which was the full depth of the beam flange.

Only the flanges of the tee attachments were scanned using LPA. To perform LPA testing, the probe was placed on the underside of the beam flange, the side not containing the attachment. The probe was first placed as close to the web of the beam as possible. Then, the probe was moved parallel to the flange of the tee. At numerous locations along the flange, the beam was swept from an angle of 30° to 88° in one-degree increments to create an S-scan of the cross section. The probe was attached to an encoder which tracked the position of the probe allowing for the collection of data versus position on the specimen. Two scans were performed to cover the entire flange area. The area covered by each LPA scan is shown in Figure 3.14. The equipment used for the linear phased array testing is shown in Figure 3.15.

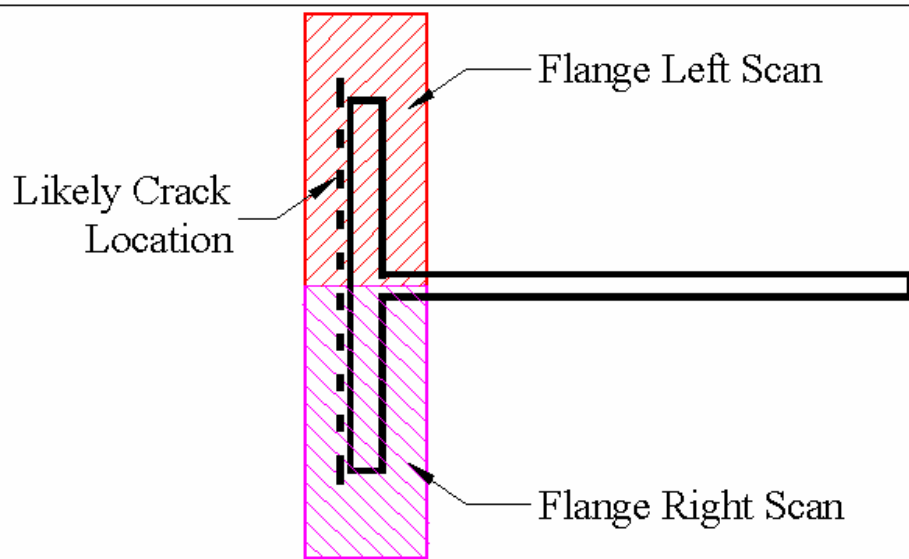
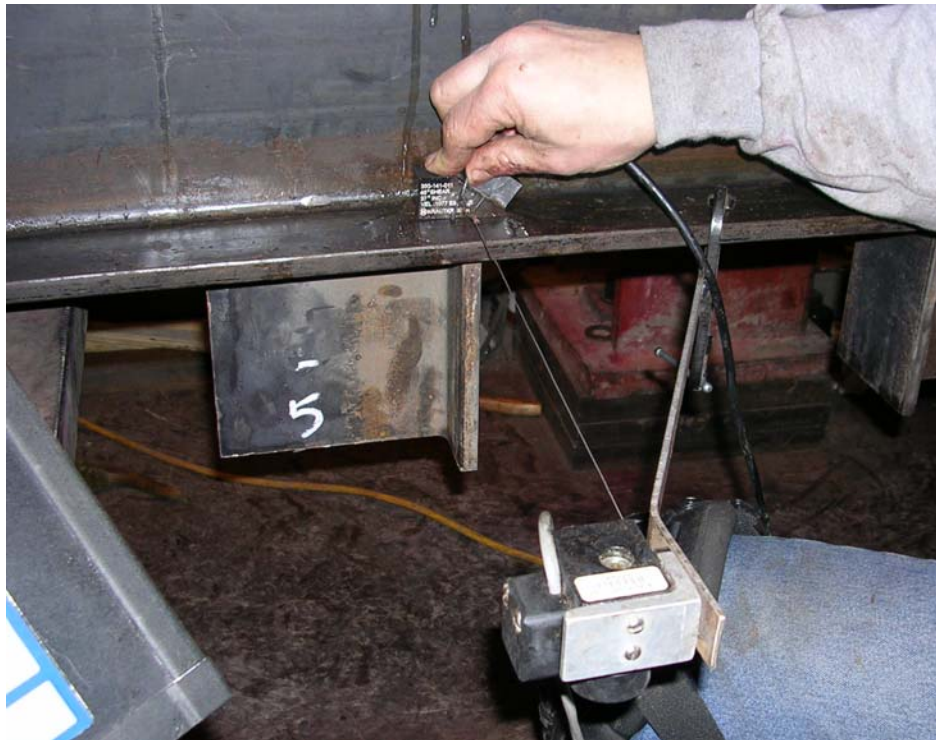


Figure 3.14: Area covered by each LPA scan



(a) Linear phased array probe



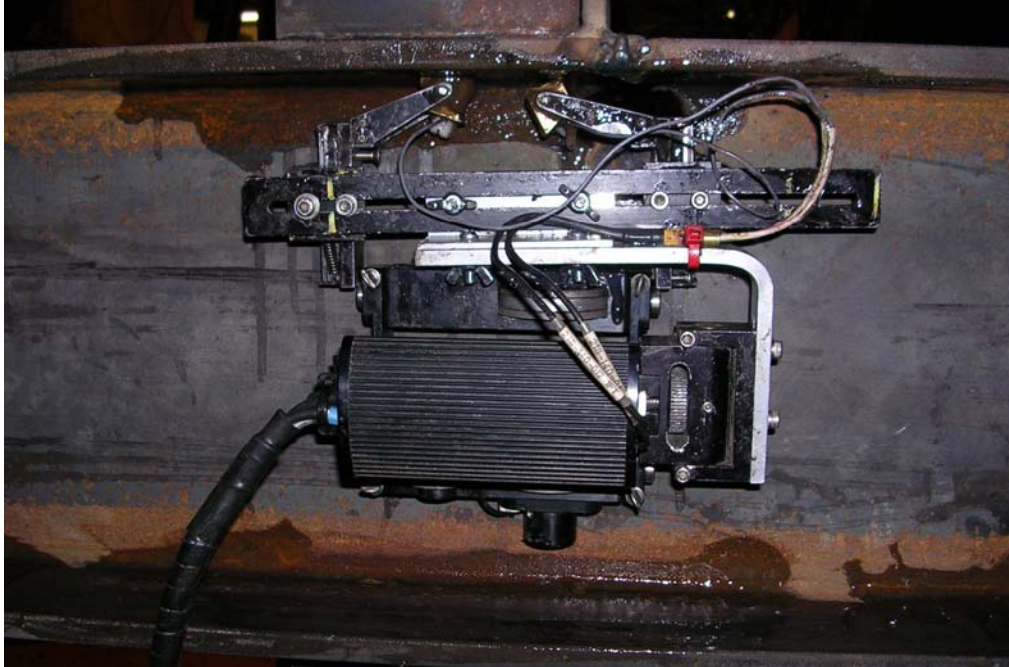
(b) Linear phased array probe and encoder

Figure 3.15: Linear phased array testing equipment

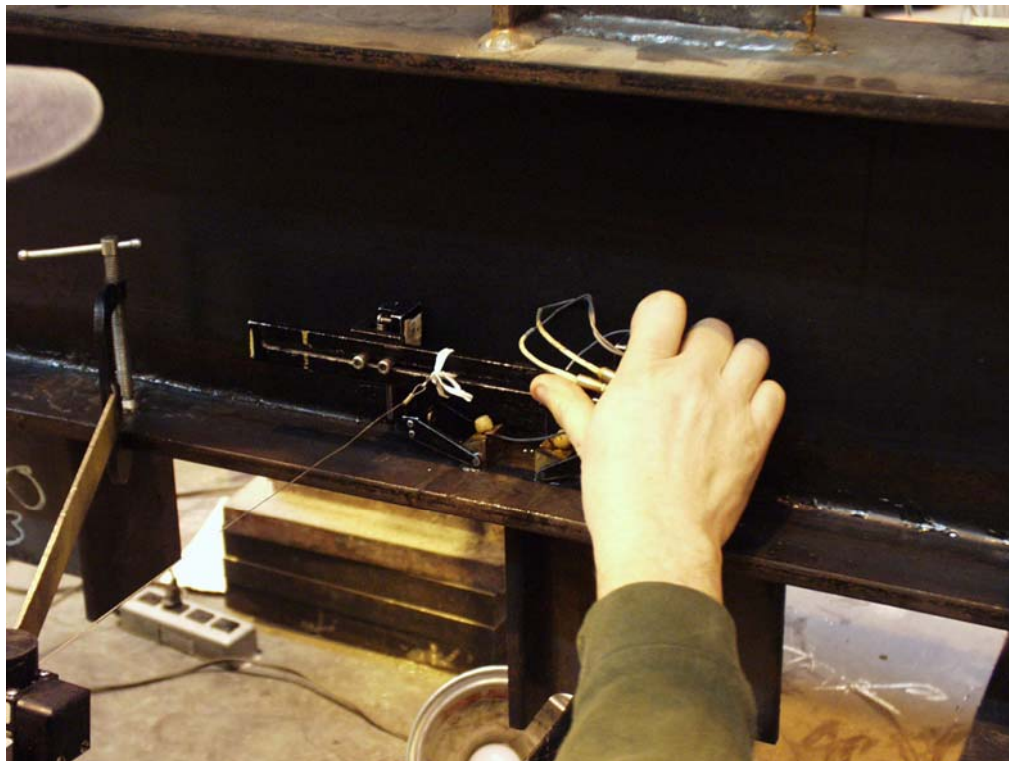
3.6.2 Time of Flight Diffraction Procedure

To perform time of flight diffraction testing on the specimens, dual transducers were used in a pitch-catch configuration. The transducers were mounted on a frame to keep them at a constant spacing during testing. The transmitting transducer introduced compression waves into the beam at a frequency of 10 MHz. Each of the two transducers was mounted in a 60-degree wedge. Two different offsets, or angle of skew transverse to the line between the transducers, were used during testing, both a zero degree and a 19° offset. The scans were performed by placing the transducers on the underside of the specimen flange, that is the side not containing the fillet weld. The transducer frame was attached to an encoder, which tracked the position of the transducers along the beam. This allowed for a B- or D-scan to be created from which the positions of defects along the weld toe were determined. The equipment used to perform the TOFD testing is shown in Figure 3.16.

Several scans of the tee attachments were performed. One scan was done along the flange of each tee attachment on either side of the beam web. To scan the tee flange, the transducers were placed such that the line connecting the transducers was transverse to the flange, as seen in Figure 3.17 (a). The transducers were then drawn along the beam surface parallel to the flange of the tee to obtain a D-scan of the fillet weld toe. In order to detect cracking along the weld toe of the stem of the tee, two similar scans were performed. For each of the scans along the tee stem, the transducers were placed as close to the beam web as possible with the line connecting the transducers parallel to the stem. The transducers were then drawn along the beam parallel to the tee stem to obtain a B-scan of the area, as seen in Figure 3.17 (b). This scan was performed from both sides of the beam web. Two transducer configurations, both a 0° and a 19° offset, were used in the scans of the tee stem in order to detect cracking. The 19° offset scan was used to capture any cracking that may be occurring in line with the beam web, an area that may not be completely visible during the zero offset scan. The area covered by each scan is seen in Figure 3.18. Through analysis of these scans, the crack depths at each location of interest were estimated.

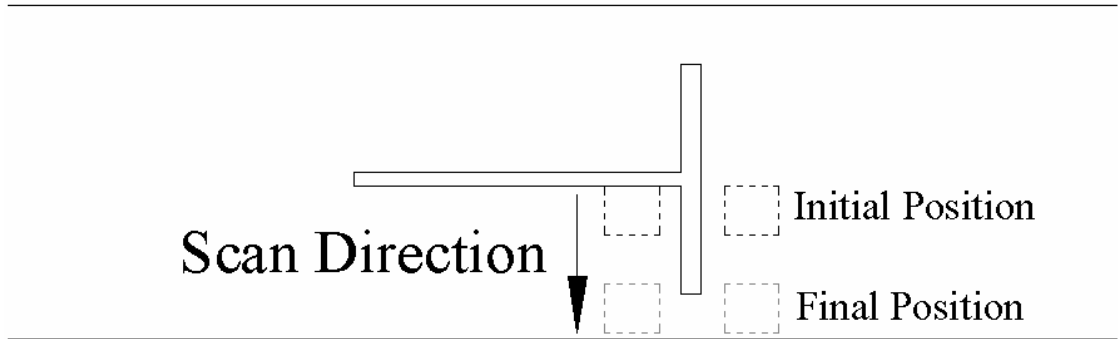


(a) TOFD equipment used for scanning stem of tee attachments

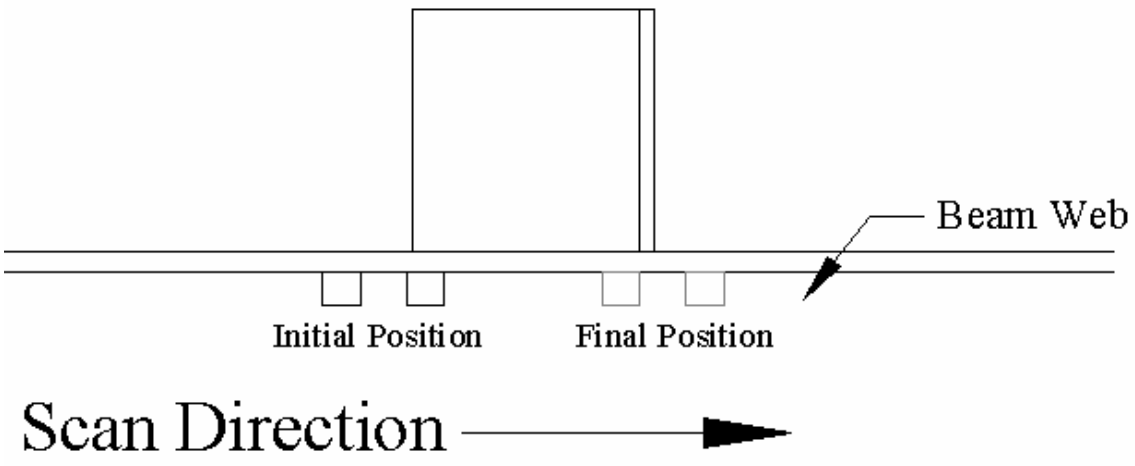


(b) TOFD equipment used for scanning flange of tee attachments

Figure 3.16: TOFD testing equipment



(a) D-scan of tee flange



(b) B-scan of tee stem

Figure 3.17: Probe placement for the TOFD scanning of flange and stem of tee attachment

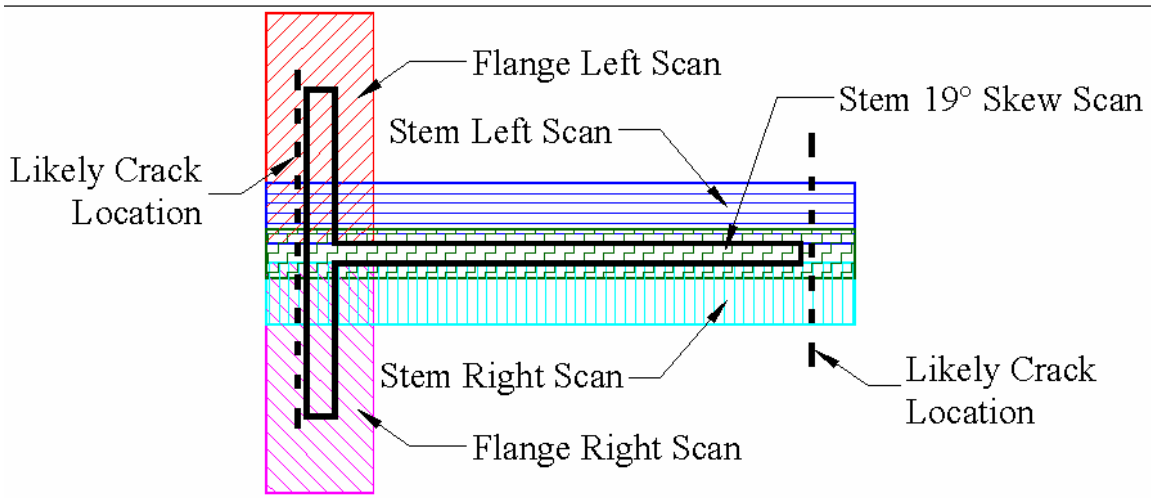


Figure 3.18: Area covered by each UT scan

3.6.3 Dye Penetrant Testing

Dye penetrant testing was performed periodically during fatigue cycling to monitor the specimens for signs of visible cracking. To perform dye penetrant testing, the specimen was first cleaned to remove any debris or residue. A red dye was sprayed on the area of interest and allowed to sit for several minutes. Then, the area was again wiped clean. Finally, a developer was sprayed on the test surface. When surface breaking cracks existed, the dye seeped out of the cracks staining the white developer so cracking could be identified and measured.

3.7 Fatigue Testing History

During fatigue testing, each specimen was monitored closely for cracking. The detailed fatigue history of each specimen is described in the following sections.

3.7.1 Specimen A

A tabulated fatigue history of Specimen A is found in Table 3.4. The weld toes of Specimen A were hammer peened. This greatly increased the fatigue life of this specimen over the non-hammer peened specimen. As part of Project SSC-425, this specimen underwent at least 2 million fatigue cycles at a stress range of 100 MPa. Specimen A had no visible signs of cracking at the end of Project SSC-425. As part of the current project, this specimen underwent an additional 5,932,869 cycles, all at a stress range of 100 MPa. During the first round of fatigue testing for this project, Specimen A was subjected to 709,419 cycles. No visible cracking was found in the specimen at that time.

During the second round of fatigue testing, Specimen A was subjected to an additional 500,000 fatigue cycles, for a total of 1,209,419 cycles. There were no visible signs of cracking at the end of this period.

After 3,063,309 total cycles, visible signs of cracking were found at the stem of Tee 1. The crack at the stem of Tee 1 grew to become a through thickness crack 50 mm in length after 5,932,869 total cycles, at which time fatigue testing was ended. This was the only failure suffered by Specimen A during this project.

Table 3.4: Fatigue history of Specimen A

Cycle Count ^a	Event
0	Baseline NDT Begin fatigue testing at stress range of 100 MPa
709,419	Second NDT (no visible cracking)
1,209,419	Final NDT (no visible cracking)
5,932,869	Failure at Stem of Tee 1, 50 mm through thickness length End of cycling

a Includes only cycles endured during the current project

3.7.2 Specimen B

A tabulated fatigue history of Specimen B is found in Table 3.5. As with Specimen A, Specimen B underwent fatigue cycles during the course of testing for Project SSC-425 at a stress range of 100 MPa. During the first round of fatigue testing for the current project, Specimen B was subjected to a load range of 440 kN, for a stress range of 200 MPa, in order to assure that the attachments reached failure. After 386,648 cycles, this beam suffered a fracture at Tee 3. A crack originating at the weld toe along the flange of Tee 3 severed the entire flange of the beam and propagated 7.5 cm into the beam web, as seen in Figure 3.19. There was no visible indication of cracking prior to the failure of this attachment. In order to continue cycling this beam, the fractured portion was repaired as described in Section 3.5. In addition to the two-sided weld repair of the flange, however, a two-sided weld repair of the cracked portion of the web was also necessary. Photos of this weld repair are shown in Figure 3.20. There were no visible indications of cracking, besides the obvious fracture at Tee 3 at the time of the second round of NDT.

After the first round of fatigue testing, it was decided to cycle Specimen B at a reduced stress range to prevent another fracture. The stress range was reduced to 100 MPa, which was the stress range applied to both of the other specimens in the project. During the second round of testing, 613,352 cycles were put on specimen B at this lowered stress range. Thus, Specimen B was subjected to a total of one million cycles before the final

NDT, however at differing stress ranges. At the time of the final NDT, there were no visible signs of cracking in Specimen B.

After the final NDT, an additional 1,695,748 cycles, were put on Specimen B before any visible signs of cracking were found. At this point, the specimen suffered from a large, rapidly growing crack, similar to the crack that formed earlier in testing. The stem of Tee 8 cracked along the root of the weld, severing the entire right side of the beam flange, extending 50 mm through the left side of the beam flange and 45 mm into the beam web. This crack was repaired as described in Section 3.5 before cycling continued.

Visible signs of cracking began to appear after 2,825,568 cycles. Three visible cracks appeared on Specimen B before the end of the project, at the stems of Tees 5 and 6 and the flange of Tee 6. None of these cracks grew to become through thickness cracks before the end of cycling. After 4,765,176 cycles, the repair weld at the stem of Tee 8 suffered a failure and cycling was ended.

Table 3.5: Fatigue history of Specimen B

Cycle Count ^a	Event
0	Baseline NDT Begin fatigue testing at stress range of 200 MPa
386,648	Failure at flange of Tee 3 (completely severed beam flange, cracked 75 mm into beam web), repaired Second NDT Reduce stress range to 100 MPa
1,000,000	Final NDT (no visible cracking)
2,695,748	Failure at stem of Tee 8 (severed right side of beam flange and 50 mm left side of beam flange, cracked 45 mm into web), repaired
2,825,568	Visible crack at stem of Tee 5
4,021,108	Visible crack at flange of Tee 6
4,189,688	Visible crack at stem of Tee 6
4,765,176	Failure at stem of Tee 8 (repair weld) End of cycling

a Includes only cycles endured during the current project



(a) Crack along beam flange



(b) Crack in beam web

Figure 3.19: Crack in flange of Specimen B at flange of Tee 3



(a) Weld repair of beam flange



(b) Weld repair of beam web

Figure 3.20: Weld repair of large crack in Specimen B at flange of Tee 3

3.7.3 Specimen C

A tabulated fatigue history of Specimen C is found in Table 3.6. Specimen C was the only non-hammer peened specimen, thus the fatigue life of this specimen was considerably less than that of the other two specimens, both of which were hammer-peened. At the beginning of this project, Specimen C was newly fabricated, thus it had not undergone any fatigue cycles before the baseline NDT. At the end of the first round of fatigue testing, 386,395 fatigue cycles had been applied to Specimen C. At that time, a small visible crack was found along the weld toe at the stem of Tee 6. This was assumed to be the approximate midlife of the specimen. Then, an additional 276,625 cycles were applied to Specimen C after the second round of NDT. During this time, many visible surface cracks formed at the attachment details. Visible cracks were detected at 15 locations on the beam, that is at the stem of each tee, and at the flange of all tees with the exception of Tee 5. These cracks varied in length between 30 and 60 mm along the weld toe. However, only one crack grew through the entire thickness of the beam flange, at the flange of Tee 4. The second round of fatigue testing was ended when this crack grew to become 50 mm in through thickness length, which was considered the end of the attachment fatigue life.

After the final round of NDT, the crack at the flange of Tee 4 was repaired as described in Section 3.5 and fatigue cycling continued. After an additional 61,800 fatigue cycles, or 706,820 total cycles, through thickness cracks 50 mm in length had formed at the stem of Tees 3, 6 and 8. These three crack locations were repaired.

Testing was continued for an additional 114,114 cycles, for a total of 820,934 cycles. After 777,820 cycles, failure was reached at the flange of Tee 6. This crack was not repaired. Cycling was continued until the crack nearly severed the beam flange, at which time it was impossible to continue cycling without performing repairs. During that time, three additional through thickness cracks formed and failure was reached at the flange of Tee 1 and the stem of Tees 2 and 7.

Table 3.6: Fatigue history of Specimen C

Cycle Count	Event
0	Baseline NDT Begin fatigue testing at stress range of 200 MPa
368,395	Visible crack at stem of Tee 6 Second NDT
375,129	Visible cracks at stem of Tees 2, 3, and 7
395,655	Visible cracks at stem and flange of Tee 4
415,095	Visible cracks at stem of Tees 1, 5, and 8
427,230	Visible crack at flange of Tee 6
445,295	Visible cracks at flange of Tees 1, 2, 3, 7, and 8
645,020	Failure at flange of Tee 4, 50 mm through thickness length, repaired Final NDT
706,820	Failure at stem of Tees 3, 6 and 8, all 50 mm through thickness length, repaired
777,820	Failure at flange of Tee 6, 50 mm through thickness length
820,934	Failure at stem of Tees 2 and 7, and flange of Tee 1, all 50 mm through thickness length End of cycling

4 TESTING RESULTS

The results of both fatigue testing and NDT are presented. The NDT measurements are correlated as best as possible with the remaining life of the attachment details as described below.

4.1 Fatigue Testing Results

Failure was reached at eleven total locations on the three beams. Specimen B, a hammer-peened specimen failed at two locations. Specimen A, the other hammer-peened specimen failed at one location during the course of testing. Specimen C, the non-hammer-peened specimen failed at eight locations. The locations of failure with the number of cycles at failure can be found in Tables 4.1 to 4.3 for Specimens A, B, and C, respectively.

Specimen C was monitored throughout testing for visual signs of cracking during fatigue testing. Surface crack lengths were measured several times during testing. It was observed that the fatigue cracks growing on the flange side of the attachments would grow to large lengths, extending along a large portion of the weld toe, which extends most of the width of the beam flange. These cracks would grow rapidly on the outer surface of the flange, then the growth rate would appear to slow, which likely indicated that the crack was growing through the thickness of the beam flange. Once the crack broke through to the inner surface, failure was rapid as the length of the crack on the inner surface of the beam flange extended to the length of the crack as seen from the outer surface. The cracks growing at the tee stems, however, behaved somewhat differently due to the different geometry. These cracks still grew rapidly to extend along the length of the weld toe, which is much shorter than for the tee flange. Then, the growth rate of the surface crack would slow until the crack grew to be through thickness. Once the crack grew through the thickness of the beam flange, it appeared to grow at a similar rate on both the outer and inner surfaces of the beam flange. All cracks appeared to grow roughly symmetrically over the beam web. Figure 4.1 shows the crack length versus number of cycles for Specimen C for the locations that reached failure during the course of testing. As can be seen, the fatigue cracks grew in a consistent manner.

Table 4.1 NDT results for Specimen A

Location	Cycles at Failure	Crack Depth (mm)			
		Second NDT (709,419 cycles)		Final NDT (1,209,419 cycles)	
		TOFD	LPA	TOFD	LPA
Tee 1-Flange	5,932,869			1.17	
Tee 1-Stem			--	1.14	--
Tee 2-Flange					
Tee 2-Stem			--		--
Tee 3-Flange		0.79			
Tee 3-Stem			--	0.2	--
Tee 4-Flange				2.67	1.65
Tee 4-Stem			--		--
Tee 5-Flange				2.08	1.27
Tee 5-Stem			--		--
Tee 6-Flange					
Tee 6-Stem			--		--
Tee 7-Flange				2.72	2.54
Tee 7-Stem		0.2	--	0.2	--
Tee 8-Flange		0.13		1.67	
Tee 8-Stem			--	0.2	--

-- No LPA scan performed at this location

Table 4.2 NDT results for Specimen B

Location	Cycles at Failure	Crack Depth (mm)			
		Second NDT (386,648 cycles)		Final NDT (1,000,000 cycles)	
		TOFD	LPA	TOFD	LPA
Tee 1-Flange					
Tee 1-Stem			--	2.49	--
Tee 2-Flange				3.07	
Tee 2-Stem			--		--
Tee 3-Flange	386,648				
Tee 3-Stem			--		--
Tee 4-Flange				1.37	Possible Indication
Tee 4-Stem			--	1.52	--
Tee 5-Flange				4.42	
Tee 5-Stem			--	0.69	--
Tee 6-Flange				0.25	
Tee 6-Stem			--	0.38	--
Tee 7-Flange				0.25	
Tee 7-Stem			--		--
Tee 8-Flange				0.86	Possible Indication
Tee 8-Stem	2,695,748	0.76	--	0.76	--

-- No LPA scan performed at this location

Table 4.3 NDT results for Specimen C

Location	Cycles at Failure	Crack Dimension (mm)					
		Second NDT (368,395 cycles)			Final NDT (645,020 cycles)		
		TOFD Depth	LPA Depth	Surface Crack Length	TOFD Depth	LPA Depth	Surface Crack Length
Tee 1-Flange	820,934				0.25		25
Tee 1-Stem		0.48	--		3.18	--	40
Tee 2-Flange		1.52			1.27		30
Tee 2-Stem	820,934		--		2.11	--	30
Tee 3-Flange							25
Tee 3-Stem	706,820		--			--	30
Tee 4-Flange	645,020				N/A	Possible Indication	Failed and Repaired
Tee 4-Stem			--		3.4	--	30
Tee 5-Flange					0.25	Possible Indication	0
Tee 5-Stem			--		4.78	--	20
Tee 6-Flange	777,820				1.8		50
Tee 6-Stem	706,820		--	10	4.78	--	30
Tee 7-Flange		0.13			0.13	1.27	38
Tee 7-Stem	820,934		--		2.95	--	25
Tee 8-Flange					3.2	3.18	50
Tee 8-Stem	706,820	1.14	--		3.05	--	40

-- No LPA scan performed at this location

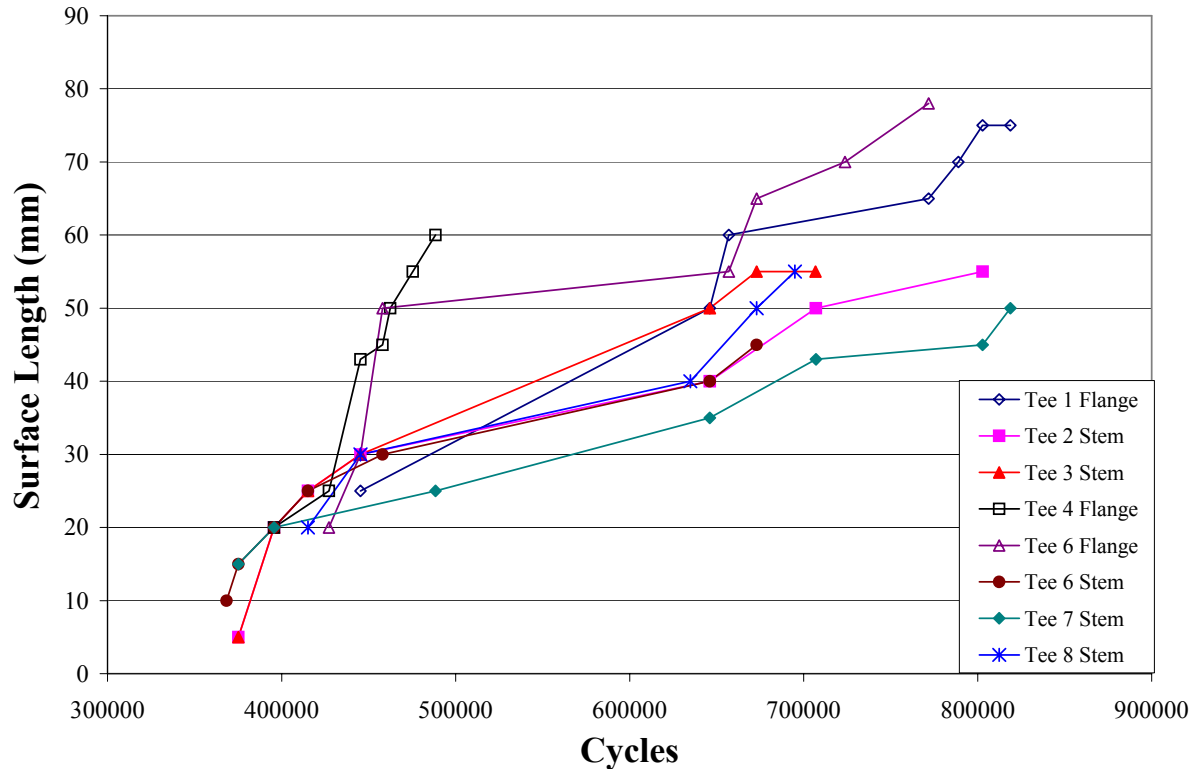


Figure 4.1: Number of cycles vs. surface length for attachments on Specimen C

4.2 Non-Destructive Testing Results

No indication of cracking was found during the baseline UT inspection for any of the three specimens. Indications of cracking were found at various locations on all specimens during the second UT inspection. Numerous indications of cracking were found during the final UT inspection, especially for Specimen C, the non-hammer peened specimen, which suffered eight failures. A tabulated summary of the results of NDT testing is found in Tables 4.1 to 4.3 for the three specimens. Because the UT inspections were performed from the inner side of the beam flange, several scans were needed to cover a single area of interest due to the beam web. The area covered by each scan is seen in Figures 3.14 and 3.18 for LPA and TOFD, respectively. Thus, there was the potential for a crack at a single tee flange to appear on two scans for each UT method, and three TOFD scans for the stem of tees. Tables 4.1 through 4.3 include only the largest crack depth found at a single location over the various scans. Also included in Table 4.3 are any visual indications of cracking at the time of UT found using dye penetrant testing for Specimen C. There were no visual indications of cracking before

failure for Specimens A or B. Full NDT results including indications of cracking from each scan are found in the Appendix Tables A.1 to A.9.

The TOFD method appears to be much more receptive to the type of cracking found in this application than LPA. LPA found no indication of cracking during the second NDT investigation and only five indications of cracking at the flange side of an attachment over the three specimens during the final NDT investigation. In contrast, TOFD found indications of cracking at eight locations over the three specimens during the second NDT investigation, four each on a stem and a flange side of an attachment. Indications were found at 33 locations, 17 at the flange of a tee and 16 at the stem of a tee, during the final NDT investigation using TOFD. At 13 locations over the three NDT investigations, LPA failed to detect a crack where TOFD found an indication. At three additional locations, LPA found only a possible indication of cracking while TOFD found a definitive indication.

At only five locations, during the final NDT investigation, did both TOFD and LPA find a quantifiable indication of cracking. The relationship between the crack depths found using the two UT methods at these five locations was not strong, as shown in Figure 4.2. The square of the correlation coefficient from a linear fit of the crack depths between the two methods was only 0.50. Ideally, this relationship should be one-to-one with a slope of unity, assuming that the crack was detectable by both methods.

Other inconsistencies in the UT data were found. On two scans of the specimens, the flange right scan of Tee 3 of Specimen A and the flange right scan of Tee 2 of Specimen C, there was an indication of cracking during the second TOFD investigation, which did not appear during the final TOFD investigation. At three locations on Specimen C, TOFD was unable to detect a crack which was visible from the beam surface. These visible cracks were located at the stem of Tee 6 during the second TOFD investigation, and during the third TOFD investigation at both the flange and stem of Tee 3. The visible crack at the flange of Tee 3 also went undetected by LPA.

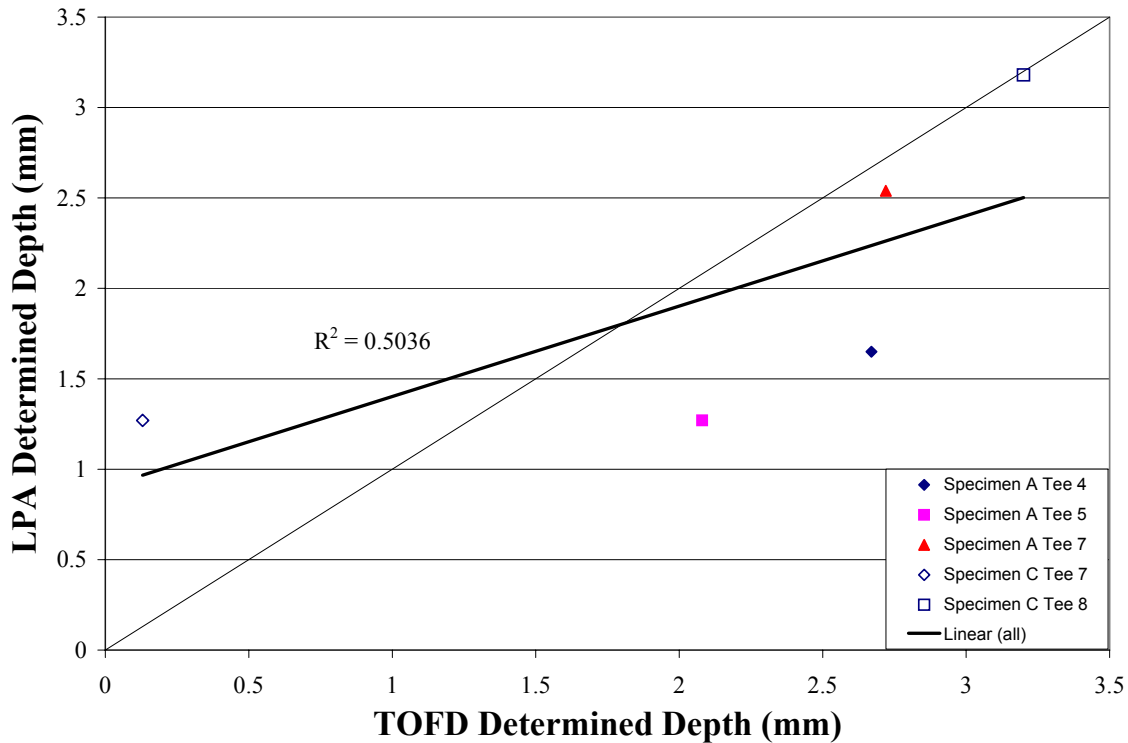


Figure 4.2: Depth of crack found using TOFD vs. LPA

It is possible the fatigue cracks in this study were subject to crack closure, which leads to transmission of ultrasonic energy through the crack and a lower amplitude signal returned to the transducer. Golan [17] found that the signal from a closed fatigue crack could be lower by tens of decibels than open cracks. Temple [38] found that surface interaction, which allows for transmission, could occur with applied tensile stresses up to 88 MPa. As the specimens in this project were under no load at the time of ultrasonic testing, there was likely enough surface interaction for transmission to be problematic. This transmission could account for the limited results found by LPA which is dependent on the amplitude of a reflected signal for the detection and characterization of defects. Past researchers have found difficulty in sizing fatigue cracks using LPA with error of less than 3 mm in depth [19]. TOFD is less sensitive to crack closure effects, as it is not dependent on the amplitude of a returned signal. However, if the amplitude of the signal from a closed crack was reduced to the point of the noise level, the crack could have gone undetected. This crack closure effect could be responsible for the failure of TOFD to detect the three visible cracks.

The accuracy and reliability of any non-destructive testing method is dependent on both the method itself and the operator performing the testing. Silk [48,49] found that when an operator is properly trained in the performance and analysis of TOFD, the probability of a defect being detected and characterized accurately is not dependent on the capabilities of the operator. Shipp [29] found similar results for LPA. Thus, the large amount of variability and inconsistencies in the UT data found in this study are likely method dependent, not operator error. The results presented give a reasonable representation of results that would be obtained using TOFD and LPA in practice for this application.

LPA detected few defects during testing and found no indications of cracking at locations which failed. Because of this lack of defect detection, and the supporting evidence in the literature review that LPA is probably not the appropriate method for measuring fatigue crack growth, it will not be discussed further in this chapter.

4.3 Correlation of TOFD Results to Remaining Fatigue Life

Data of crack depth found using TOFD versus cycles to failure of an attachment was collected. Only the largest depth of crack at a single location was used in the correlation efforts.

It can be seen from Figure 4.3 that using the small amount of data collected, only seven data points, some correlation was found between the depth of crack found using TOFD with the remaining fatigue life for this configuration of a non hammer-peened welded joint. Using a linear regression, the R^2 value was found to be 0.42. The correlation is somewhat better when only the data representing the failure at the stem side of the tee attachment is considered (five data points), increasing the R^2 value to 0.74. On the two occasions where multiple attachment details failed at the same time, it can be seen that the difference in TOFD indication of depth is over 13% of the beam flange depth. There appears to be a general trend to the data, but with so few data points conclusions cannot be drawn. This method of correlation does not seem viable for the given application, however it may be proved feasible to use TOFD for the prediction of remaining fatigue life with additional testing.

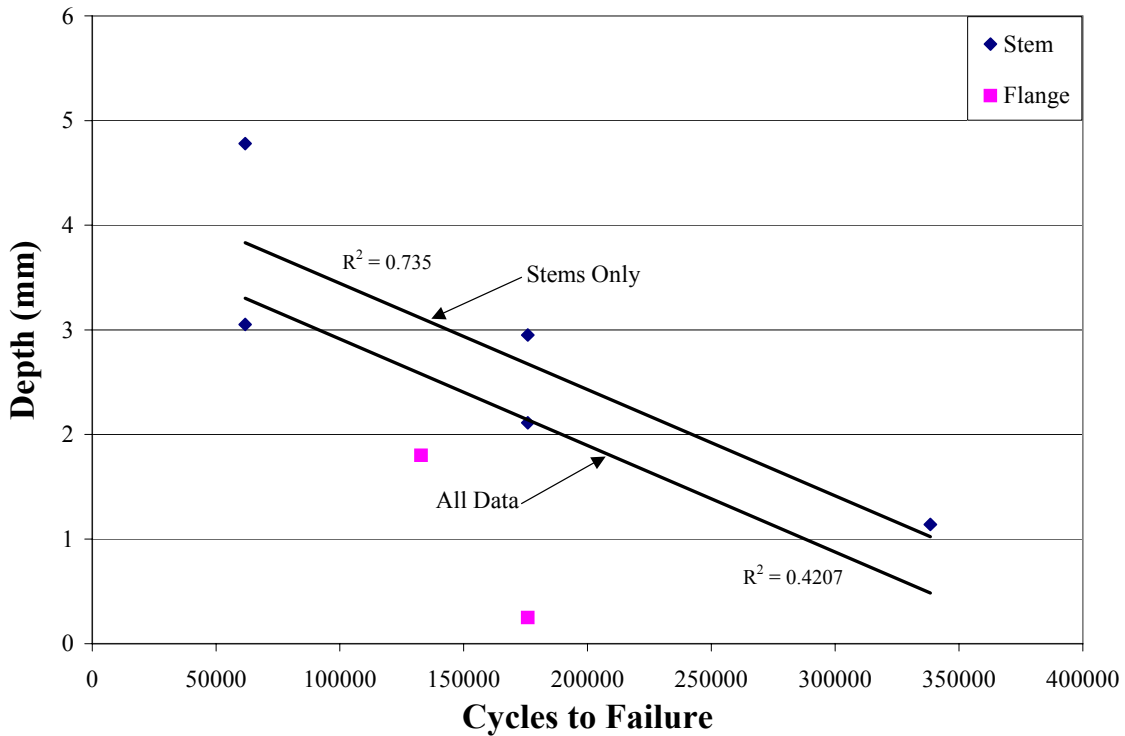


Figure 4.3: Cycles to failure vs. TOFD estimated crack depth for non hammer-peened attachment details

There was too little data to determine if there was a correlation between the TOFD data and the remaining life of the hammer-peened detail as only three locations reached failure during the course of fatigue testing, shown in Figure 4.4.

4.4 Correlation of Visual Observations to Remaining Fatigue Life

The relationship between the visual observations of surface crack length and the remaining fatigue life of the attachment was investigated. As shown in Figure 4.5, there was a strong linear relationship between these two quantities with an R^2 value of 0.71. Again, as for the TOFD data, the correlation improved when the data was split into stems of attachment which produced an R^2 value of 0.81 and flanges of attachments which produced an R^2 value of 0.85.

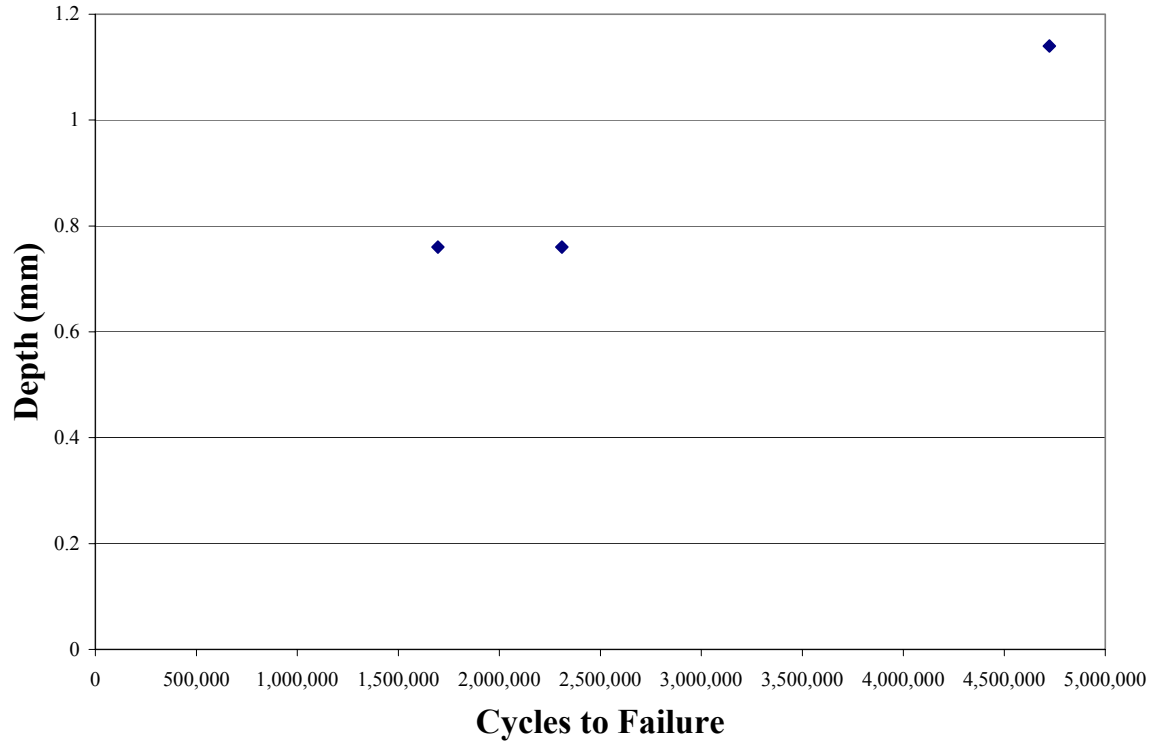


Figure 4.4: Cycles to failure vs. TOFD estimated crack depth for hammer-peened attachment details

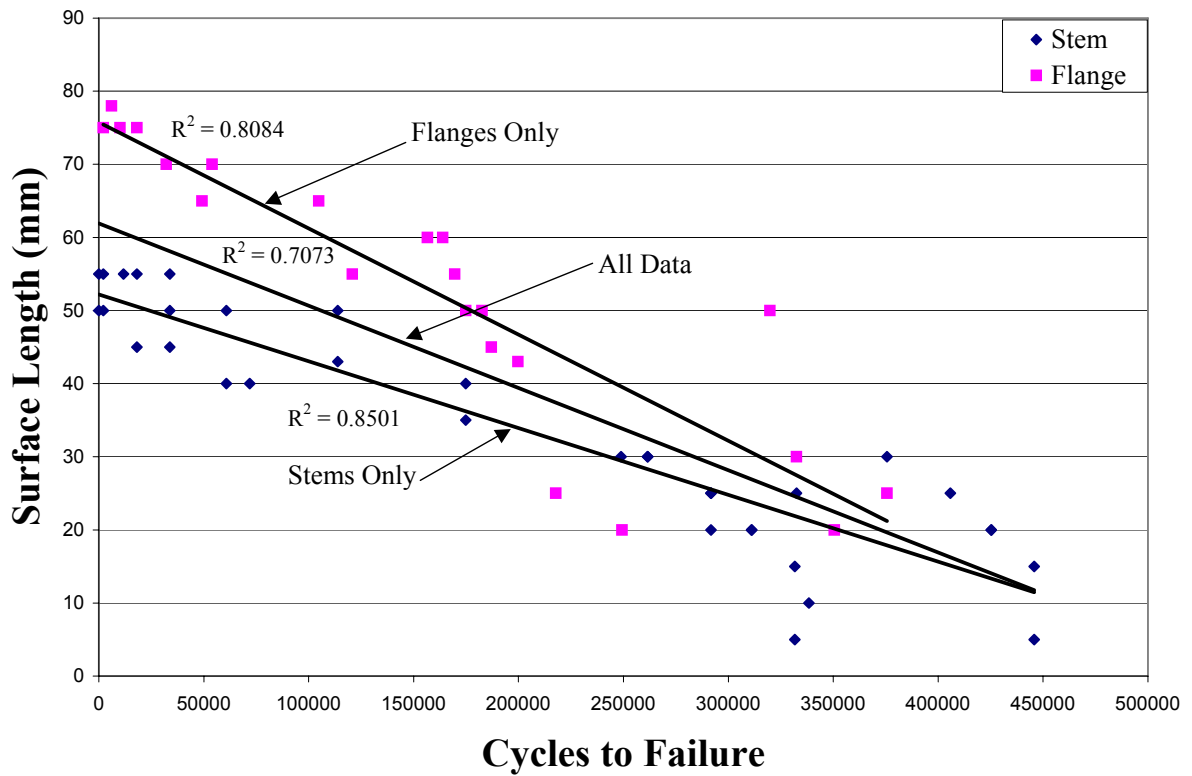


Figure 4.5: Cycles to failure vs. surface crack length

4.5 Correlation Between TOFD Measurements and Visual Observations

The relationship between the crack dimensions found using TOFD and those from visual observations was studied. It was expected that there would be a strong relationship between the crack length and crack depth as the fatigue cracks were seen to grow in a consistent manner. However, as seen in Figure 4.6, there was a large amount of scatter in this data, and little correlation was found. Using linear regression, it was found that the R^2 value was 0.02 when all of the 12 data points were considered. When only the flanges of the tee attachments were considered (five data points) the R^2 value increased to 0.55. The data from the stems of the tee attachments indicate that there was a decrease in crack depth as the crack length increased, which makes little physical sense. The correlation of the depth found at the stems of the tees and the surface crack length produces an R^2 value of 0.16.

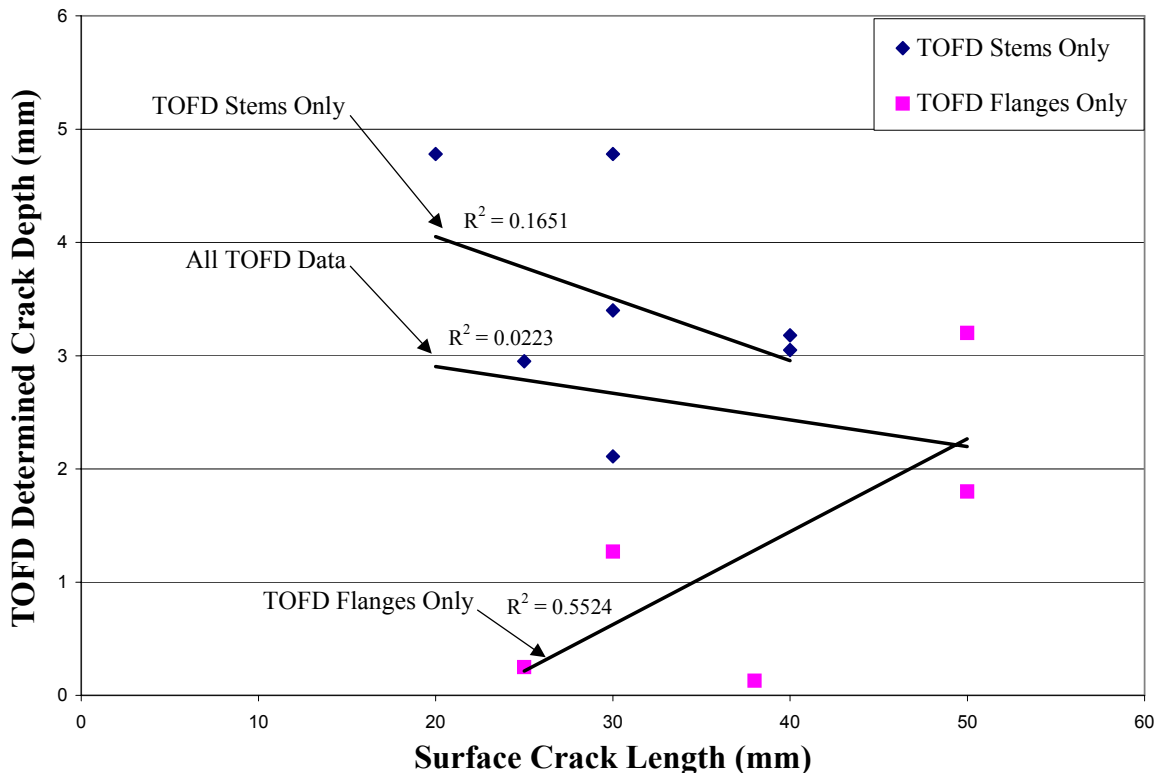


Figure 4.6: Surface crack length vs. crack depth determined using TOFD

The growth of the surface crack is initially rapid, and then slows, which likely indicates that the crack is growing in depth. As such, a single surface crack length could correlate

with a range of crack depths. This crack growth behavior could account for the large amount of variability of the surface crack length versus depth data found in this project. The crack growth behavior is dependent on the geometry of the test specimen used. The decline in the surface crack growth rate was likely due to the finite width of the attachment detail, especially for the flange of the tees. Also, the beam web could have been providing additional stiffness to the area which aided in slowing the crack growth.

4.6 Feasibility of Using Time of Flight Diffraction and Linear Phased Array Testing to Predict Remaining Fatigue Life

The limited testing and results developed through this project do not currently support any substantial conclusions regarding the prediction of remaining fatigue life with the use of ultrasonic non-destructive testing. The data of the TOFD data versus the remaining life does show a general trend that may be developed and proved with additional testing. However, as the visual observations show a strong correlation with remaining fatigue life, and the TOFD data does not correspond well to the visual observations, it is unlikely that better results would be found with additional testing using these two ultrasonic methods for test specimens with this geometry. This configuration of welded joint may not exactly represent the conditions found in ships, however, due to the presence of the beam web and the finite width of the tee attachments. Thus, further study on details that better approximate the details found in ship structures should be performed to better determine the feasibility of predicting remaining life using NDT measurements.

This finding is similar to that of Shell [5] who studied the use of UT and other NDT methods to predict the fatigue life of corroded aluminum specimens. Shell found that there was little correlation between the depths of corrosion found using UT to the remaining life of the specimens. It was found that the probability of significance of this depth parameter was 0.9144, which means there was a 91.44% chance that this correlation could occur by natural variation or chance. This is in contrast to various other parameters investigated by Shell, which showed a probability of significance of less than 0.0001. It is possible that although depth of fatigue crack does not correlate well with remaining life, other quantities measurable using UT or other NDT methods would be useful in predicting remaining fatigue life.

5 CONCLUSIONS

1. The ultrasonic, non-destructive testing methods used in this project, both time of flight diffraction and linear phased array, were poor estimators of remaining fatigue life of the welded joints studied. There appears to be little correlation between the crack depth found using UT to the remaining fatigue life of a welded joint. It seems infeasible to use these methods to predict remaining life of joints with this geometry.
2. TOFD was more sensitive to the types of crack found in this project than LPA. LPA found few indications overall, and no indications at locations which reached failure during the course of fatigue testing.
3. There was a reasonable correlation between visual observations of crack growth, aided by non-destructive dye penetrant testing, and the remaining fatigue life of a welded joint.
4. No correlation was found between the crack depths found using UT and the surface crack lengths found by visual observation as would have been expected. This indicates that the UT methods chosen may not be useful for the detection of fatigue cracking in the welded joints used in this study. This scatter could also be due to the manner in which cracks grew due to the geometry of the specimen used.
5. Hammer peening is an effective and low cost method of preventing fatigue cracking.

6 RECOMMENDATIONS

1. The use of ultrasonic non-destructive testing methods time of flight diffraction and linear phased array is not currently supported by this project as a means to be used in the estimation of remaining fatigue life of welded joints.
2. Alternative methods of non-destructive testing for the detection and characterization of fatigue cracks should be investigated to identify a method which will reliably characterize cracks. Although it is outside the scope of this project to determine alternate NDT methods for the detection of fatigue cracks, it is felt that X-ray and thermography could be considered for future research. Once a method is found, the feasibility of correlating NDT measurements to the remaining life of welded joints can again be considered. This feasibility study should include parameters other than crack depth, such as crack length, profile, reduction in signal during NDT, etc.
3. Studies should be conducted on specimens with a different geometry than used in this project, which would more accurately represent a welded detail found in ship structures.
4. For future research, NDT should be performed much more often than done in this project to more closely monitor fatigue crack growth. Taking data more often will produce more data points for correlation purposes and reduce the effect of an erroneous measurement.
5. Hammer peening should be used on welded details to prolong fatigue life.

7 REFERENCES

1. Petershagen, H. (1986), "Fatigue Problems in Ship Structures," *Advances in Marine Structures*, Elsevier Applied Science, London, pp. 281-304.
2. Jordan, C.R. and R.P. Krumpfen, Jr. (1985), "Design Guide for Ship Structural Details." Report SSC-331, Ship Structure Committee, Washington D.C.
3. Liu, D., and Thayamballi, A. (1996), "Local Cracking in Ships – Causes, Consequences, and Control." *Proceedings: Workshop and Symposium on the Prevention of Fracture in Ship Structure*, March 30-31, 1995, Washington, D.C., Marine Board, Committee on Marine Structures, National Research Council.
4. Clarke, J.D. (1991), "Fatigue Crack Initiation and Propagation in Warship Hulls," *Advances in Marine Structures – 2*, C.S. Smith and R.S. Dow, (eds), Elsevier Applied Science, London, pp. 42-60.
5. Shell, E. B., R.G. Buchheit, and B. Zoofan (2005), "Correlation of Residual Fatigue Life with Quantified NDE Measurements." *International Journal of Fatigue*, Vol 27, pp. 105-112.
6. Kim, Jung-Kyu, Sang-Soo Cho, and Chul-Su Kim (2004), "The Evaluation of Fatigue Life in TWB Sheet Using Magnetic Method." *Key Engineering Materials*, Vol. 270-273, pp. 1706-1711.
7. Asif, S.A, and R.S. Modh (1989), "Crack Propagation Study by Electric Potential Method of Non-Destructive Test Technique." *Journal of the Institution of Engineers (India), Metallurgy and Material Science Division*, March, Vol. 69, No. 2, pp. 57-59.
8. Hellier, Charles J. (2001), *Handbook of Nondestructive Evaluation*. McGraw--Hill, New York.
9. Bray, Don E., and Don McBride (1992), *Nondestructive Testing Techniques*, John Wiley & Sons, Inc., New York.

10. McIntire, Paul, ed., Albert S. Birks and Robert E. Green, Jr., technical eds. (1991), *Nondestructive Testing Handbook*, 2nd ed, Vol. 7, American Society for Nondestructive Testing.
11. Krautkramer, Herbert , and Josef Krautkramer (1990), *Ultrasonic Testing of Materials*, 4th ed. Springer-Verlag, Berlin.
12. Silk, M. G. (1979), “Defect Sizing Using Ultrasonic Diffraction.” *British Journal of NDT*, January, pp. 12-15.
13. Silk, M. G. (1984), “The Use of Diffraction-Based Time-of-Flight Measurements to Locate and Size Defects.” *British Journal of NDT*, May, pp. 208-213.
14. Temple, J.A.G. (1983), “Time-of-Flight Inspection: Theory.” *Nuclear Energy*, October, Vol. 22, No. 5, pp. 335-348.
15. Charlesworth, J. P., and J.A.G. Temple (1989), *Engineering Applications of Ultrasonic Time-of-Flight Diffraction*, John Wiley & Sons, Inc., New York.
16. Baskaran, G., Krishnan Balasubramaniam, C.V. Krishnamurthy, and C. Lakshmana Rao (2004), “Ultrasonic TOFD Flaw Sizing and Imaging in Thin Plates Using Embedded Signal Identification Technique (ESIT).” *Insight*, September, Vol. 46, No. 9, pp. 537-542.
17. Golan, S., Laszlo Adler, K.V. Cook, R.K. Nanstad, and T.K. Bolland (1980), “Ultrasonic Diffraction Technique for Characterization of Fatigue Cracks.” *Journal of Nondestructive Evaluation*, Vol. 1, No. 1, pp. 11-19.
18. Moles, Michael, Noel Dube, and Frederic Jacques (2004), “Ultrasonic Phased Arrays for Thick Section Weld Inspections.” *Proceedings from Joining of Advanced and Specialty Materials VI, Pittsburg, PA, 13-15 October 2003*, pp. 112-118.

19. Choqueuse, D., and A. Lamarre (1998), "Use of Phased Array Ultrasonic Equipment for Fatigue Crack Characterization for Underwater Inspection of Offshore Structures." *Proceedings of the Eighth International Offshore and Polar Engineering Conference*, Vol. 4, Montreal, Canada, May, pp. 86-89.
20. Crowther, P (2004). "Practical Experience of Phased Array Technology for Power Station Applications." *Insight*, Vol 6, No. 9, September, pp. 525-528.
21. McNab, A., and M.J. Campbell (1987), "Ultrasonic Phased Arrays for Nondestructive Testing." *NDT International*, December, Vol. 20, No. 6, pp. 333-337.
22. Poon, W., B.W. Drinkwater, and P.D. Wilcox (2004), "Modeling Ultrasonic Array Performance in Simple Structures." *Insight*, February, Vol. 46, No. 2, pp. 80-81, 84.
23. Huang, J., P.W. Que, and J.H. Jin (2004), "Adaptive Dynamic Focusing System for Ultrasonic Nondestructive Testing of Pipeline Girth Welds." *Review of Scientific Instruments*, May, Vol. 75, No. 5, pp. 1341-1346.
24. Lamarre, Andre (1999), "Dynamic Focusing of Phased Arrays for Nondestructive Testing: Characterization and Application." *NDT.net*, September, Vol. 4, No. 9.
25. Gros, X. E., N.B. Cameron, and M. King (2002), "Current Applications and Future Trends in Phased Array Technology." *Insight*, November, Vol. 44, No. 11, pp. 673-678.
26. Wooh, Shi-Chang, and Yijun Shi (1998), "Influence of Phased Array Element Size on Beam Steering Behavior." *Ultrasonics*, Vol. 36, pp. 737-749.
27. MacDonald, Doug E., Mark A. Dennis, Jeff L. Landrum, and Greg P. Selby (2002), "Phased Array UT Technology for Nuclear Pipe Inspection." *American Society of Mechanical Engineers, Pressure Vessels and Piping Division PVP*, Vol. 450, pp. 11-20.

28. Komura, Ichiro, Taiji Hirasawa, Satoshi Nagai, Jun-ichi Takabayashi, and Katsuhiko Naruse (2001), "Crack Detection and Sizing Techniques by Ultrasonic and Electromagnetic Methods." *Nuclear Engineering and Design*, Vol. 206, pp. 351-362.
29. Shipp, R., C.R.A. Schneider, C.R. Bird, and D.A. Wood (2003), "Independent Qualification of Phased Array Inspection of Fillet Welds." *Insight*, February, Vol. 45, No. 2, pp. 122-124.
30. Mahaut, Steve, Jean-Louis Godefroit, Olivier Roy, and Gerard Cattiaux (2004), "Application of Phased Array Techniques to Coarse Grain Components Inspection." *Ultrasonics*, Vol. 42, pp. 791-796.
31. Date, K., H. Shimada, and N. Ikenga (1982), "Crack Height Measurement – an Evaluation of the Accuracy of Ultrasonic Timing Methods." *NDT International*, December, pp. 315-319.
32. Baby, S., T. Balasubramanian, R.J. Pardikar, M. Palaniappan, and R. Subbaratnam (2003), "Time-of-Flight Diffraction (TOFD) Technique for Accurate Sizing of Surface-Breaking Cracks." *Insight*, June, Vol. 45, No. 6, pp. 426-430.
33. Golan, S. (1981), "Optimization of the Crack Tip Ultrasonic Diffraction Technique for Sizing of Cracks." *Materials Evaluation*, February, Vol. 39, pp. 166-169.
34. Browne, Bill (1997), "Time of Flight Diffraction – Its Limitations – Actual & Perceived." *NDT.net*, September, Vol. 2, No. 9.
35. Silk, M. G. (1987), "Changes in Ultrasonic Defect Location and Sizing." *NDT International*, Vol. 20, No. 1, pp. 9-14.
36. Silk, M. G. (1982), "The Fundamental Accuracy of Ultrasonic Time-of-Flight Testing Techniques." *Periodic Inspection of Pressurized Components*, pp. 125-132.

37. Zippel, William J., Jose A. Pincheira, and Glenn A. Washer (2000), "Crack Measurement in Steel Plates Using TOFD Method." *Journal of Performance of Constructed Facilities*, May, Vol. 14, No. 2, pp. 75-82.
38. Temple, J.A.G. (1985), "Effects of Stress and Crack Morphology on Time-of-Flight Diffraction Signals." *International Journal of Pressure Vessels and Piping*, Vol. 19, No. 3, pp. 185-211.
39. Mihara, Tsuyoshi, Masashi Nomura, and Kazushi Yamanaka (2002), "Relations Between Crack Opening Behavior and Crack Tip Diffraction of Longitudinal Wave." *Nondestructive Evaluation and Reliability of Micro- and Nanomaterial Systems*, Vol. 4703, pp. 137-145.
40. Mihara, Tsuyoshi, Shinji Nomura, Masashi Akino, and Kazushi Yamanaka (2004), "Relationship Between Crack Opening Behavior and Crack Tip Scattering and Diffraction of Longitudinal Waves." *Materials Evaluation*, September, Vol. 62, No. 9, pp. 943-947.
41. Whapham, A.D., S. Perring, and K.L. Rusbridge (1985), "The Effect of Stress on the Transmission of Ultrasound Through Fatigue Cracks." *Seventh International Conference on NDE in the Nuclear Industry, Grenoble (France)*, January/February, pp. 389-392.
42. Silk, M. G., and B.H. Lidington (1975), "Defect Sizing Using an Ultrasonic Time Delay Approach." *British Journal of NDT*, March, pp. 33-36.
43. Baby, S., T. Balasubramanian, and R.J. Pardikar (2002), "Estimation of the Height of Surface-Breaking Cracks Using Ultrasonic Timing Methods." *Insight*, November, Vol. 44, No.11, pp. 679-683.
44. Yokono, Y., Y. Minami, S. Mukae, M. Katoh, and K. Nishio (1992), "Fundamental Study on Detectability of Subsurface Defects by Ultrasonic Testing." *Nondestructive Testing and Evaluation*, Vol. 7, No. 1, pp. 281-296.

45. Lidington, B.H., M/G. Silk, P. Montgomery, and G. Hammond (1976), "Ultrasonic Measurements of the Depth of Fatigue Cracks." *British Journal of NDT*, November, pp. 165-170.
46. Bloodworth, T (1999), "High-Accuracy Defect Sizing for Nozzle Attachment Welds Using Asymmetric TOFD." *Insight*, September, Vol. 41, No. 9, pp. 589-591.
47. Verkooijen, J. (1995), "TOFD Used to Replace Radiography." *Insight*, June, Vol. 37, No. 6, pp. 433-435.
48. Silk, M. G. (1996A), "Estimates of the Probability of Detection of Flaws in TOFD Data with Varying Levels of Noise." *Insight*, January, Vol. 38, No. 1, pp. 31-36.
49. Silk, M. G. (1996B), "An Evaluation of the Performance of the TOFD Technique as a Means of Sizing Flaws, with Particular Reference to Flaws with Curved Profiles." *Insight*, April, Vol. 38, No. 4, pp. 280-287.
50. Blitz, Jack. Electrical and Magnetic Methods of Non-destructive Testing. 2nd ed. London: Chapman & Hall, 1997.
51. Dexter, Robert, Robert Fitzpatrick, and David St. Peter (2003), "Fatigue Strength and Adequacy of Weld Repairs." Report SSC-425, Ship Structure Committee, Washington, D.C.
52. Knight, J.W. (1978), "Improving the Fatigue Strength of Fillet Welded Joints by Grinding and Peening," *Welding Research International*, Vol. 8, No. 6.

APPENDIX: NON-DESTRUCTIVE TESTING DATA

This appendix contains full ultrasonic non-destructive testing results from this project for Specimens A, B and C. Included are the crack depths found using time of flight diffraction for all three UT investigations, and linear phased array measurements for the final two UT investigations. The measurements found from each individual scan are presented, which includes three scans for each tee stem using TOFD and two scans of each tee flange for both methods. Also included are the surface crack lengths found using dye penetrant testing at the time of UT for Specimen C only. The tables include the number of cycles at failure for all attachments.

Table A.1 NDT results for Specimen A

Location	Crack depth (mm) at baseline TOFD	Crack depth (mm) at 709,419 cycles		Crack depth (mm) at 1,209,419 cycles		Number of cycles at failure
		TOFD	LPA	TOFD	LPA	
Tee 1-Flange Left	NRI	NRI	NRI	NRI	NRI	
Tee 1-Flange Right	NRI	NRI	NRI	1.17	NRI	
Tee 1-Stem Left	NRI	NRI	--	NRI	--	5,932,869
Tee 1-Stem Right	NRI	NRI	--	NRI	--	5,932,869
Tee 1-Stem 19° skew	NRI	NRI	--	1.14	--	5,932,869
Tee 2-Flange Left	NRI	NRI	NRI	NRI	NRI	
Tee 2-Flange Right	NRI	NRI	NRI	NRI	NRI	
Tee 2-Stem Left	NRI	NRI	--	NRI	--	
Tee 2-Stem Right	NRI	NRI	--	NRI	--	
Tee 2-Stem 19° skew	NRI	NRI	--	NRI	--	
Tee 3-Flange Left	NRI	NRI	NRI	NRI	NRI	
Tee 3-Flange Right	NRI	0.79	NRI	NRI	NRI	
Tee 3-Stem Left	NRI	NRI	--	NRI	--	
Tee 3-Stem Right	NRI	NRI	--	0.2	--	
Tee 3-Stem 19° skew	NRI	NRI	--	NRI	--	
Tee 4-Flange Left	NRI	NRI	NRI	2.67	1.65	
Tee 4-Flange Right	NRI	NRI	NRI	NRI	NRI	
Tee 4-Stem Left	NRI	NRI	--	NRI	--	
Tee 4-Stem Right	NRI	NRI	--	NRI	--	
Tee 4-Stem 19° skew	NRI	NRI	--	NRI	--	
Tee 5-Flange Left	NRI	NRI	NRI	NRI	NRI	
Tee 5-Flange Right	NRI	NRI	NRI	2.08	1.27	
Tee 5-Stem Left	NRI	NRI	--	NRI	--	
Tee 5-Stem Right	NRI	NRI	--	NRI	--	
Tee 5-Stem 19° skew	NRI	NRI	--	NRI	--	
Tee 6-Flange Left	NRI	NRI	NRI	NRI	NRI	
Tee 6-Flange Right	NRI	NRI	NRI	NRI	NRI	
Tee 6-Stem Left	NRI	NRI	--	NRI	--	
Tee 6-Stem Right	NRI	NRI	--	NRI	--	
Tee 6-Stem 19° skew	NRI	NRI	--	NRI	--	
Tee 7-Flange Left	NRI	NRI	NRI	NRI	NRI	
Tee 7-Flange Right	NRI	NRI	NRI	2.72	2.54	
Tee 7-Stem Left	NRI	0.2	--	0.2	--	
Tee 7-Stem Right	NRI	NRI	--	NRI	--	
Tee 7-Stem 19° skew	NRI	NRI	--	NRI	--	
Tee 8-Flange Left	NRI	NRI	NRI	NRI	NRI	
Tee 8-Flange Right	NRI	0.13	NRI	1.67	NRI	
Tee 8-Stem Left	NRI	NRI	--	NRI	--	
Tee 8-Stem Right	NRI	NRI	--	0.2	--	
Tee 8-Stem 19° skew	NRI	NRI	--	NRI	--	

NRI No Reliable Indication

--- No LPA scan performed at this location

Table A.2 NDT results for Specimen B

Location	Crack depth (mm) at baseline TOFD	Crack depth (mm) at 386,648 cycles		Crack depth (mm) at 1,000,000 cycles		Number of cycles at failure
		TOFD	LPA	TOFD	LPA	
Tee 1-Flange Left	NRI	NRI	NRI	NRI	NRI	
Tee 1-Flange Right	NRI	NRI	NRI	NRI	NRI	
Tee 1-Stem Left	NRI	NRI	--	NRI	--	
Tee 1-Stem Right	NRI	NRI	--	2.49	--	
Tee 1-Stem 19° skew	NRI	NRI	--	NRI	--	
Tee 2-Flange Left	NRI	NRI	NRI	NRI	NRI	
Tee 2-Flange Right	NRI	NRI	NRI	3.07	NRI	
Tee 2-Stem Left	NRI	NRI	--	NRI	--	
Tee 2-Stem Right	NRI	NRI	--	NRI	--	
Tee 2-Stem 19° skew	NRI	NRI	--	NRI	--	
Tee 3-Flange Left	NRI	NRI	NRI	NRI [†]	NRI [†]	386,648
Tee 3-Flange Right	NRI	NRI	NRI	NRI [†]	NRI [†]	386,648
Tee 3-Stem Left	NRI	NRI	--	NRI	--	
Tee 3-Stem Right	NRI	NRI	--	NRI	--	
Tee 3-Stem 19° skew	NRI	NRI	--	NRI	--	
Tee 4-Flange Left	NRI	NRI	NRI	NRI	PI	
Tee 4-Flange Right	NRI	NRI	NRI	1.37	PI	
Tee 4-Stem Left	NRI	NRI	--	1.52	--	
Tee 4-Stem Right	NRI	NRI	--	NRI	--	
Tee 4-Stem 19° skew	NRI	NRI	--	1.27	--	
Tee 5-Flange Left	NRI	NRI	NRI	NRI	NRI	
Tee 5-Flange Right	NRI	NRI	NRI	0.48/4.42	NRI	
Tee 5-Stem Left	NRI	NRI	--	0.69	--	
Tee 5-Stem Right	NRI	NRI	--	NRI	--	
Tee 5-Stem 19° skew	NRI	NRI	--	NRI	--	
Tee 6-Flange Left	NRI	NRI	NRI	NRI	NRI	
Tee 6-Flange Right	NRI	NRI	NRI	0.25	NRI	
Tee 6-Stem Left	NRI	NRI	--	NRI	--	
Tee 6-Stem Right	NRI	NRI	--	NRI	--	
Tee 6-Stem 19° skew	NRI	NRI	--	0.38	--	
Tee 7-Flange Left	NRI	NRI	NRI	NRI	NRI	
Tee 7-Flange Right	NRI	NRI	NRI	0.25	NRI	
Tee 7-Stem Left	NRI	NRI	--	NRI	--	
Tee 7-Stem Right	NRI	NRI	--	NRI	--	
Tee 7-Stem 19° skew	NRI	NRI	--	NRI	--	
Tee 8-Flange Left	NRI	NRI	NRI	0.86	PI	
Tee 8-Flange Right	NRI	NRI	NRI	NRI	NRI	
Tee 8-Stem Left	NRI	0.76	--	0.76	--	2,695,748
Tee 8-Stem Right	NRI	NRI	--	NRI	--	2,695,748
Tee 8-Stem 19° skew	NRI	NRI	--	NRI	--	2,695,748

NRI No Reliable Indication
 PI Possible indication
 --- No LPA scan performed at this location
 † After repair

Table A.3 NDT results for Specimen C

Location	Crack depth (mm) at baseline TOFD	368,395 cycles			645,020 cycles			Number of cycles at failure
		TOFD crack depth (mm)	LPA crack depth (mm)	Visual surface length (mm)	TOFD crack depth (mm)	LPA crack depth (mm)	Visual surface length (mm)	
Tee 1-Flange Left	NRI	NRI	NRI		0.25	NRI	25	820,934
Tee 1-Flange Right	NRI	NRI	NRI		NRI	NRI	25	820,934
Tee 1-Stem Left	NRI	0.2	--		3.18	--	40	
Tee 1-Stem Right	NRI	0.48	--		1.65	--	40	
Tee 1-Stem 19° skew	NRI	NRI	--		1.65	--	40	
Tee 2-Flange Left	NRI	NRI	NRI		1.27	NRI	30	
Tee 2-Flange Right	NRI	1.52	NRI		NRI	NRI	30	
Tee 2-Stem Left	NRI	NRI	--		NRI	--	30	820,934
Tee 2-Stem Right	NRI	NRI	--		2.11	--	30	820,934
Tee 2-Stem 19° skew	NRI	NRI	--		NRI	--	30	820,934
Tee 3-Flange Left	NRI	NRI	NRI		NRI	NRI	25	
Tee 3-Flange Right	NRI	NRI	NRI		NRI	NRI	25	
Tee 3-Stem Left	NRI	NRI	--		NRI	--	30	706,820
Tee 3-Stem Right	NRI	NRI	--		NRI	--	30	706,820
Tee 3-Stem 19° skew	NRI	NRI	--		NRI	--	30	706,820
Tee 4-Flange Left	NRI	NRI	NRI		NRI [†]	NRI [†]		645,020
Tee 4-Flange Right	NRI	NRI	NRI		NRI [†]	PI [†]		645,020
Tee 4-Stem Left	NRI	NRI	--		NRI	--	30	
Tee 4-Stem Right	NRI	NRI	--		3.4	--	30	
Tee 4-Stem 19° skew	NRI	NRI	--		1.27	--	30	
Tee 5-Flange Left	NRI	NRI	NRI		0.25	PI		
Tee 5-Flange Right	NRI	NRI	NRI		NRI	NRI		
Tee 5-Stem Left	NRI	NRI	--		4.78	--	20	
Tee 5-Stem Right	NRI	NRI	--		1.68	--	20	
Tee 5-Stem 19° skew	NRI	NRI	--		NRI	--	20	
Tee 6-Flange Left	NRI	NRI	NRI		NRI	NRI	50	777,820
Tee 6-Flange Right	NRI	NRI	NRI		1.8	NRI	50	777,820
Tee 6-Stem Left	NRI	NRI	--	10	4.78	--	30	706,820
Tee 6-Stem Right	NRI	NRI	--	10	2.16	--	30	706,820
Tee 6-Stem 19° skew	NRI	NRI	--	10	2.16	--	30	706,820
Tee 7-Flange Left	NRI	NRI	NRI		NRI	NRI	38	
Tee 7-Flange Right	NRI	0.13	NRI		0.13	1.27	38	
Tee 7-Stem Left	NRI	NRI	--		2.95	--	25	820,934
Tee 7-Stem Right	NRI	NRI	--		2.54	--	25	820,934
Tee 7-Stem 19° skew	NRI	NRI	--		NRI	--	25	820,934
Tee 8-Flange Left	NRI	NRI	NRI		NRI	NRI	50	
Tee 8-Flange Right	NRI	NRI	NRI		3.2	3.18	50	
Tee 8-Stem Left	NRI	NRI	--		2.95	--	40	706,820
Tee 8-Stem Right	NRI	1.14	--		3.05	--	40	706,820
Tee 8-Stem 19° skew	NRI	NRI	--		3.05	--	40	706,820

NRI No Reliable Indication

--- No LPA scan performed at this location

PI

†

Possible indication

After repair

PROJECT TECHNICAL COMMITTEE MEMBERS

The following persons were members of the committee that represented the Ship Structure Committee to the Contractor as resident subject matter experts. As such they performed technical review of the initial proposals to select the contractor, advised the contractor in cognizant matters pertaining to the contract of which the agencies were aware, performed technical review of the work in progress and edited the final report.

Chairman Mr. Natale Nappi, Jr. NAVSEA

Members

Contracting Officer's Technical Representative:

Ms. Theresa Garnes NAVSEA

Project Technical Committee Members:

Executive Director:

LT Eric M. Cooper USCG

Administrative Assistant:

Ms. Jeannette Delaney ARTI, USCG

SHIP STRUCTURE COMMITTEE PARTNERS AND LIAISON MEMBERS

PARTNERS

The Society of Naval Architects and Marine Engineers

Mr. Bruce S. Rosenblatt
President,
Society of Naval Architects and Marine Engineers

Dr. John Daidola
Chairman,
SNAME Technical & Research Steering
Committee

The Gulf Coast Region Maritime Technology Center

Dr. John Crisp
Executive Director,
Gulf Coast Maritime Technology Center

Dr. Bill Vorus
Site Director,
Gulf Coast Maritime Technology Center

LIAISON MEMBERS

American Iron and Steel Institute
American Society for Testing & Materials
American Society of Naval Engineers
American Welding Society
Bath Iron Works
Canada Ctr for Minerals & Energy Technology
Colorado School of Mines
Edison Welding Institute
International Maritime Organization
Int'l Ship and Offshore Structure Congress
INTERTANKO
Massachusetts Institute of Technology
Memorial University of Newfoundland
National Cargo Bureau
Office of Naval Research
Oil Companies International Maritime Forum
Tanker Structure Cooperative Forum
Technical University of Nova Scotia
United States Coast Guard Academy
United States Merchant Marine Academy
United States Naval Academy
University of British Columbia
University of California Berkeley
University of Houston - Composites Eng & Appl.
University of Maryland
University of Michigan
University of Waterloo
Virginia Polytechnic and State Institute
Webb Institute
Welding Research Council
Worcester Polytechnic Institute
World Maritime Consulting, INC
Samsung Heavy Industries, Inc.

Mr. Alexander Wilson
Captain Charles Piersall (Ret.)
Captain Dennis K. Kruse (USN Ret.)
Mr. Richard Frank
Mr. Steve Tarpy
Dr. William R. Tyson
Dr. Stephen Liu
Mr. Dave Edmonds
Mr. Tom Allen
Dr. Alaa Mansour
Mr. Dragos Rauta
Mr. Dave Burke / Captain Chip McCord
Dr. M. R. Haddara
Captain Jim McNamara
Dr. Yapa Rajapaksie
Mr. Phillip Murphy
Mr. Rong Huang
Dr. C. Hsiung
Commander Kurt Colella
Dr. C. B. Kim
Dr. Ramswar Bhattacharyya
Dr. S. Calisal
Dr. Robert Bea
Dr. Jerry Williams
Dr. Bilal Ayyub
Dr. Michael Bernitsas
Dr. J. Roorda
Dr. Alan Brown
Dr. Kirsi Tikka
Dr. Martin Prager
Dr. Nick Dembsey
VADM Gene Henn, USCG Ret.
Dr. Satish Kumar

RECENT SHIP STRUCTURE COMMITTEE PUBLICATIONS

Ship Structure Committee Publications on the Web - All reports from SSC 392 and forward are available to be downloaded from the Ship Structure Committee Web Site at URL:

<http://www.shipstructure.org>

SSC 391 and below are available on the SSC CD-ROM Library. Visit the National Technical Information Service (NTIS) Web Site for ordering information at URL:

<http://www.ntis.gov/fcpc/cpn7833.htm>

SSC Report Number	Report Bibliography
SSC 443	Design Guidelines for Doubler Plate Repairs on Ship Structures Sensharma P.K., Dinovitzer A., Traynham Y. 2005
SSC 442	Labor-Saving Passive Fire Protection Systems For Aluminum And Composite Construction E. Greene, 2005
SSC 441	Fire Degradation, Failure Prediction And Qualification Methods For Fiber Composites R. Asaro, M. Dao, 2005
SSC 440	Deterioration of Structural Integrity Due to Chemical Treatment of Ballast Water S. Tikku, 2005
SSC 439	Comparative Structural Requirements For High Speed Crafts K. Stone, 2005
SSC 438	Structural Optimization for Conversion of Aluminum Car Ferry to Support Military Vehicle Payload, R.Kramer, 2005
SSC 437	Modeling Longitudinal Damage in Ship Collisions A.J. Brown, JAW Sajdak 2005
SSC 436	Effect of Fabrication Tolerances on Fatigue Life of Welded Joints A. Kendrick, B. Ayyub, I. Assakkaf 2005
SSC 435	Predicting Stable Fatigue Crack Propagation in Stiffened Panels R.J. Dexter, H.N. Mahmoud 2004
SSC 434	Predicting Motion and Structural Loads in Stranded Ships Phase 1 A.J. Brown, M. Simbulan, J. McQuillan, M. Gutierrez 2004
SSC 433	Interactive Buckling Testing of Stiffened Steel Plate Panels Q. Chen, R.S. Hanson, G.Y. Grondin 2004
SSC 432	Adaptation of Commercial Structural Criteria to Military Needs R.Vara, C.M. Potter, R.A. Sielski, J.P. Sikora, L.R. Hill, J.C. Adamchak, D.P. Kihl, J. Hebert, R.I. Basu, L. Ferreiro, J. Watts, P.D. Herrington 2003